

Berichte

zur Polar-
und Meeresforschung

608
2010

Reports
on Polar and Marine Research



Airborne lidar observations of tropospheric Arctic clouds

Astrid Lampert

 **HELMHOLTZ**
| GEMEINSCHAFT

ALFRED-WEGENER-INSTITUT FÜR
POLAR- UND MEERESFORSCHUNG
In der Helmholtz-Gemeinschaft
D-27570 BREMERHAVEN
Bundesrepublik Deutschland

ISSN 1866-3192

Hinweis

Die Berichte zur Polar- und Meeresforschung werden vom Alfred-Wegener-Institut für Polar- und Meeresforschung in Bremerhaven* in unregelmäßiger Abfolge herausgegeben.

Sie enthalten Beschreibungen und Ergebnisse der vom Institut (AWI) oder mit seiner Unterstützung durchgeführten Forschungsarbeiten in den Polargebieten und in den Meeren.

Es werden veröffentlicht:

- Expeditionsberichte (inkl. Stationslisten und Routenkarten)
- Expeditionsergebnisse (inkl. Dissertationen)
- wissenschaftliche Ergebnisse der Antarktis-Stationen und anderer Forschungs-Stationen des AWI
- Berichte wissenschaftlicher Tagungen

Die Beiträge geben nicht notwendigerweise die Auffassung des Instituts wieder.

Notice

The Reports on Polar and Marine Research are issued by the Alfred Wegener Institute for Polar and Marine Research in Bremerhaven*, Federal Republic of Germany. They appear in irregular intervals.

They contain descriptions and results of investigations in polar regions and in the seas either conducted by the Institute (AWI) or with its support.

The following items are published:

- expedition reports (incl. station lists and route maps)
- expedition results (incl. Ph.D. theses)
- scientific results of the Antarctic stations and of other AWI research stations
- reports on scientific meetings

The papers contained in the Reports do not necessarily reflect the opinion of the Institute.

The „Berichte zur Polar- und Meeresforschung“
continue the former „Berichte zur Polarforschung“

* Anschrift / Address

Alfred-Wegener-Institut
für Polar- und Meeresforschung
D-27570 Bremerhaven
Germany
www.awi.de

Editor in charge:
Dr. Horst Bornemann

Assistant editor:
Birgit Chiaventone

Die "Berichte zur Polar- und Meeresforschung" (ISSN 1866-3192) werden ab 2008 ausschließlich als Open-Access-Publikation herausgegeben (URL: <http://epic.awi.de>).

Since 2008 the "Reports on Polar and Marine Research" (ISSN 1866-3192) are only available as web based open-access-publications (URL: <http://epic.awi.de>)

Airborne lidar observations of tropospheric Arctic clouds

Astrid Lampert

**Please cite or link this item using the identifier
hdl:10013/epic.34255 or <http://hdl.handle.net/10013/epic.34255>**

ISSN 1866-3192

Astrid Lampert
Institute of Aerospace Systems
Technische Universität Carolo-Wilhelmina zu Braunschweig
Hermann-Blenk-Str. 23
D - 38108 Braunschweig
Germany
Astrid.Lampert@tu-bs.de

for my husband Philipp

This work is licensed under a Creative Commons License:
Attribution - Noncommercial - Share Alike 3.0 Germany
To view a copy of this license visit
<http://creativecommons.org/licenses/by-nc-sa/3.0/de/deed.en>

Die vorliegende Arbeit ist die inhaltlich unveränderte Fassung einer Dissertation, die in der Sektion „Atmosphärische Zirkulation“ am Alfred-Wegener-Institut für Polar- und Meeresforschung, Forschungsstelle Potsdam, bei Prof. Dr. K. Dethloff angefertigt und an der Mathematisch-Naturwissenschaftlichen Fakultät der Universität Potsdam im Jahr 2009 vorgelegt wurde.

Die Arbeit wurde zugleich online als Dissertation an der Universität Potsdam publiziert unter urn:nbn:de:kobv:517-opus-41211

Contents

Summary	iii
Zusammenfassung	v
1 Introduction	1
1.1 Cloud research in the Arctic	1
1.2 Objectives of the thesis	4
1.3 Motivation: Arctic clouds in climate models	5
1.4 Structure of the thesis	7
2 Tropospheric Arctic clouds	8
2.1 Macrophysical cloud properties	8
2.2 Physical processes and interactions	10
2.3 Radiative effects	13
3 Lidar data evaluation	16
3.1 Scattering theory	16
3.1.1 Rayleigh scattering	16
3.1.2 Mie scattering	17
3.1.3 Scattering of non-spherical particles	17
3.2 The elastic lidar equation	18
3.2.1 Lidar equation	18
3.2.2 Klett evaluation algorithm	19
3.2.3 Transmittance method	20
3.3 Depolarization and color ratio	21
3.3.1 Depolarization ratio	21
3.3.2 Color ratio	21
3.4 Multiple scattering effects on lidar retrievals	22
3.5 Limits of lidar investigation for cloud observations	23
4 The Airborne Mobile Aerosol Lidar (AMALi)	24
4.1 Technical setup	24
4.1.1 Transmitting and receiving system	24
4.1.2 Controller	27
4.1.3 Transient recorders	27
4.1.4 Software	28
4.2 AMALi in the Polar-2 aircraft	29
4.3 Data evaluation	30
5 The Arctic Study of Tropospheric Aerosol, Clouds and Radiation (ASTAR) 2007	32
5.1 Participants, organization, operations	32
5.2 AMALi in the ASTAR campaign	35
5.3 Instrumentation on board of the Polar-2	37
5.4 Technical problems	39
5.5 Synoptic situation	40
5.6 Aerosol and pollution situation	42
6 Case study: Subvisible midlevel ice cloud	46
6.1 Meteorological situation	47
6.2 Optical and microphysical characterization	49
6.2.1 Lidar remote sensing	49
6.2.2 In situ measurements	50
6.2.3 Radiation data	53
6.3 Discussion	54
6.3.1 Microphysical properties	54

6.3.2 Simulation of the measured radiation.....	57
6.3.3 Lidar ratio.....	59
6.3.4 Cloud radiative forcing.....	61
6.4 Interpretation: Implication for the Arctic radiation budget.....	62
7 Airborne observations of Arctic mixed-phase clouds.....	64
7.1 Cloud statistics at Ny-Ålesund during ASTAR 2007.....	64
7.2 Boundary layer clouds.....	65
7.2.1 Synoptic situation and cloud structure.....	67
7.2.2 Cloud thermodynamic phase.....	72
7.2.3 Cloud comparison with CALIPSO.....	74
7.2.4 Cloud comparison with ECMWF analyses.....	75
7.3 Midlevel clouds.....	76
7.3.1 Synoptic situation and cloud structure.....	77
7.3.2 Cloud thermodynamic phase.....	79
7.4 Discussion: Airborne lidar retrieval of cloud properties.....	80
8 Outlook.....	83
8.1 Summary of results.....	83
8.2 Conclusions: Airborne lidar for cloud research.....	84
8.3 Future studies involving the AMALi.....	86
8.4 Potential application in models.....	87
List of acronyms.....	89
List of symbols.....	91
References.....	93

Summary

Due to the unique environmental conditions and different feedback mechanisms, the Arctic region is especially sensitive to climate changes. The influence of clouds on the radiation budget is substantial, but difficult to quantify and parameterize in models. However, data about the Arctic atmosphere are sparse because of the remote location and harsh conditions. Therefore, dedicated airborne measurements using various instruments are necessary. Typical Arctic cloud types include multi layered clouds, mixed-phase clouds and optically thin clouds. In the framework of the PhD project, elastic backscatter and depolarization lidar (light detection and ranging) observations of Arctic clouds were performed during the international Arctic Study of Tropospheric Aerosol, Clouds and Radiation (ASTAR) from Longyearbyen airport (Svalbard) in March and April 2007. The Airborne Mobile Aerosol Lidar (AMALi) of the Alfred Wegener Institute was modified prior to the field campaign. The applied changes of the optical system, the mechanical construction, and the data acquisition allowed the detection of smaller aerosol particles with an increased measurement range, and the possibility of both nadir and zenith looking configuration onboard of the "Polar-2" Do-228 aircraft.

During the ASTAR 2007 campaign, northerly flow predominated the synoptic situation. Convective cloud streets formed in the cold air masses streaming southwards above the relatively warm open ocean West of Svalbard. The air around Svalbard advected from the North exhibited a low aerosol load. Clouds were probed above the inaccessible Arctic Ocean with a combination of airborne instruments: The AMALi provided information on the vertical and horizontal extent of clouds along the flight track, optical properties (backscatter coefficient), and cloud thermodynamic phase. From the data obtained by the spectral albedometer (University of Mainz), the cloud phase and cloud optical thickness was deduced. Furthermore, in situ observations performed with the Polar Nephelometer, Cloud Particle Imager and Forward Scattering Spectrometer Probe (Laboratoire de Météorologie Physique, France) provided information on the microphysical properties, cloud particle size and shape, concentration, extinction, liquid and ice water content. The typical flight pattern consisted of a long flight leg at constant altitude for the remote sensing configuration, and consecutively ascent / descent profiles employing the in situ instrumentation. In the thesis, a data set of four flights is analyzed and interpreted.

The lidar observations served to detect atmospheric structures of interest, which were then probed by in situ technique. With this method, an optically subvisible ice cloud was characterized by the ensemble of instruments (10 April 2007). Radiative transfer simulations based on the lidar, radiation and in situ measurements allowed the calculation of the cloud forcing, amounting to -0.4 W m^{-2} . This slight surface cooling is negligible on a local scale. However, thin Arctic clouds have been reported more frequently in winter time, when the clouds' effect on longwave radiation (a surface warming of 2.8 W m^{-2}) is not balanced by the reduced shortwave radiation (surface cooling).

Boundary layer mixed-phase clouds were analyzed for two days (8 and 9 April 2007). The typical structure consisting of a predominantly liquid water layer on cloud top and ice crystals below were confirmed by all instruments. The lidar observations were compared to ECMWF meteorological analyses. On 9 April 2007, the increase in cloud top height according to a rising boundary layer depth, as determined from meteorological calculations, was observed with lidar. Further, the analysis of a change of air masses along the flight track was evidenced in the airborne data by a small completely glaciated cloud part within the mixed-phase cloud system. This indicates that the updraft necessary for the formation of new cloud droplets at cloud top is disturbed by the mixing processes.

The lidar measurements allowed to determine the thermodynamic cloud phase of the cloud layer closest to the lidar system by analyzing the slope and absolute value of backscatter and depolarization ratio.

The measurements served to quantify the shortcomings of the ECMWF model to describe mixed-phase clouds. As the partitioning of cloud condensate into liquid and ice water is done by a diagnostic equation based on temperature, the cloud structures consisting of a liquid cloud top layer and ice below could not be reproduced correctly. A small amount of liquid water was calculated for the lowest (and warmest) part of the cloud only. Further, the liquid water content was underestimated by an order of magnitude compared to in situ observations.

The airborne lidar observations of 9 April 2007 were compared to space borne lidar data on board of the satellite CALIPSO (Cloud-Aerosol Lidar and Infrared Pathfinder Satellite Observations). The systems agreed about the increase of cloud top height along the same flight track. The airborne lidar penetrated the clouds most of the time and detected the ground return, probably due to small-scale cloud inhomogeneities, which were not resolved by the space borne lidar. However, during the time delay of 1 h between the lidar measurements, advection and cloud processing took place, and a detailed comparison of small-scale cloud structures was not possible.

A double layer cloud at an altitude of 4 km was observed with lidar at the West coast in the direct vicinity of Svalbard (14 April 2007). In contrast to the common occurrence of multi layer clouds in the boundary layer, little information is reported about multiple cloud layers in the free troposphere. The cloud system consisted of two geometrically thin liquid cloud layers (each 150 m thick) with ice below each layer. While the upper one was possibly formed by orographic lifting under the influence of westerly winds, or by the vertical wind shear shown by ECMWF analyses, the lower one might be the result of evaporating precipitation out of the upper layer. The existence of ice precipitation between the two layers supports the hypothesis that humidity released from evaporating precipitation was cooled and consequently condensed as it experienced the radiative cooling from the upper layer.

In summary, a unique data set characterizing tropospheric Arctic clouds was collected with lidar, in situ and radiation instruments. The joint evaluation with meteorological analyses allowed a detailed insight in cloud properties, cloud evolution processes and radiative effects. For future airborne campaigns, the use of two coordinated aircraft probing clouds at the same time, one carrying the lidar and radiation sensors, the other carrying the in situ instrumentation, is recommended. Better closure between the measurements is achieved, reducing uncertainties which are caused by the time delay and atmospheric changes in the mean time.

Further, the implementation of a detailed cloud microphysics parameterization into a regional weather forecast model is proposed, which is then fed with and compared to cloud data obtained by airborne and space borne lidar observations.

Zusammenfassung

Die Arktis mit ihren speziellen Umweltbedingungen ist besonders empfindlich gegenüber Klimaveränderungen. Dabei spielen Wolken eine große Rolle im Strahlungsgleichgewicht, die aber nur schwer genau bestimmt und in Klimamodellen dargestellt werden kann.

Die Daten für die Promotionsarbeit wurden im Frühjahr 2007 bei Flugzeug-Messungen von Wolken über dem Arktischen Ozean von Spitzbergen aus erhoben. Das dafür verwendete Lidar (Licht-Radar) des Alfred-Wegener-Instituts lieferte ein höhenaufgelöstes Bild der Wolkenstrukturen und ihrer Streu-Eigenschaften, andere Messgeräte ergänzten optische sowie mikrophysikalische Eigenschaften der Wolkenteilchen (Extinktion, Größenverteilung, Form, Konzentration, Flüssigwasser- und Eisgehalt, Messgeräte vom Laboratoire de Météorologie Physique, France) und Strahlungsmessungen (Uni Mainz).

Während der Messkampagne herrschte Nordwind vor. Die untersuchten Luftmassen mit Ursprung fern von menschlichen Verschmutzungsquellen war daher sehr sauber. Beim Überströmen der kalten Luft über den offenen warmen Arktischen Ozean bildeten sich in der Grenzschicht (ca. 0-1500 m Höhe) Mischphasenwolken, die aus unterkühlten Wassertröpfchen im oberen Bereich und Eis im unteren Bereich der Wolken bestehen.

Mit den Flugzeug-Messungen und numerischen Simulationen des Strahlungstransports wurde der Effekt einer dünnen Eiswolke auf den Strahlungshaushalt bestimmt. Die Wolke hatte lokal eine geringe Abkühlung der Erdoberfläche zur Folge. Ähnliche Wolken würden jedoch im Winter, wenn keine Sonnenstrahlung die Arktis erreicht, durch den Treibhauseffekt eine nicht vernachlässigbare Erwärmung der Oberfläche verursachen.

Die Messungen der Mischphasenwolken wurden mit einem Wettervorhersagemodell (ECMWF) verglichen. Für die ständig neue Bildung von flüssigen Wassertropfen im oberen Teil der Wolke ist das Aufsteigen von feuchten Luftpaketen nötig. Während einer Messung wurden entlang der Flugstrecke verschiedene Luftmassen durchflogen. An der Luftmassengrenze wurde eine reine Eiswolke inmitten eines Mischphasen-Systems beobachtet. Die Messungen zeigen, dass das Mischen von Luftmassen den Nachschub an feuchter Luft blockiert, was unmittelbare Auswirkungen auf die thermodynamische Phase des Wolkenwassers hat. Weiterhin wurde bestimmt, wie groß die Abweichungen der Modellrechnungen von den Messungen bezüglich Wassergehalt und der Verteilung von Flüssigwasser und Eis waren. Durch die vereinfachte Wolken-Parameterisierung wurde die typische vertikale Struktur von Mischphasenwolken im Modell nicht wiedergegeben.

Die flugzeuggetragenen Lidar-Messungen vom 9. April 2007 wurden mit Lidar-Messungen an Bord des Satelliten CALIPSO (Cloud-Aerosol Lidar and Infrared Pathfinder Satellite Observations) verglichen. Die Messungen zeigten beide eine ansteigende Wolkenobergrenze entlang desselben Flugwegs. Da die Messungen jedoch nicht genau gleichzeitig durchgeführt wurden, war wegen Advektion und Prozessen in den Wolken kein genauer Vergleich der kleinskaligen Wolkenstrukturen möglich.

Außerdem wurde eine doppelte Wolkenschicht in der freien Troposphäre (4 km Höhe) analysiert. Die Wolke bestand aus zwei separaten dünnen Schichten aus flüssigem Wasser (je 150 m dick) mit jeweils Eis darunter. Die untere Schicht entstand wahrscheinlich aus verdunstetem Eis-Niederschlag. Diese feuchte Schicht wurde durch die Abstrahlung der oberen Wolkenschicht gekühlt, so dass sie wieder kondensierte. Solche Wolkenformationen sind in der Arktis bisher vor allem in der Grenzschicht bekannt.

Ein einzigartiger Datensatz von arktischen Wolken wurde mit einer Kombination verschiedener Flugzeug-Messgeräte erhoben. Zusammen mit meteorologischen Analysen konnten für verschiedene Fallstudien Wolkeneigenschaften, Entwicklungsprozesse und Auswirkungen auf den Strahlungshaushalt bestimmt werden.



Photos: Astrid Lampert, Jean - François Gayet, André Ehrlich

1 Introduction

1.1 Cloud research in the Arctic

The Arctic is defined as the region within the northern polar circle, at latitudes higher than 66.5° N. It is a sensitive indicator of climate change (Corell, 2004, IPCC, 2007). This is the consequence of special interactions and dynamical feedback mechanisms of atmosphere, ocean, cryosphere and land (Curry et al., 1996). A recent, obvious change was the decrease of summer sea ice extent over the last decades (e.g. Nghiem et al., 2007). The observations raised public interest in the topic of global warming, which is most evident in the Arctic (Gore, 2006). However, a change in cloud cover may also play a key role (Kay et al., 2008).

From a climatological point of view, the Arctic is characterized by a negative radiation budget on the annual average (Fig. 1.1). The radiation deficits are compensated by meridional atmospheric and oceanic transport of heat, coupling the Arctic to the global circulation patterns. Clouds play a central role by interacting with radiation and regulating climate feedback mechanisms (Fig. 1.2). Generally, they absorb and reflect solar radiation, thus shield the Earth from the incoming radiation and contribute to a cooling of the surface. They absorb terrestrial radiation, partly emit it to space, and partly reflect it back to the surface. This "greenhouse effect" results in a warming of the underlying surface. Contrary to midlatitudes, the surface warming effect of clouds dominates in the Arctic for most of the year (Chapt. 2).

The main motivation of Arctic cloud studies is that the understanding of the cloud types specified below, their processes, feedback mechanisms and effects on radiation and the hydrological cycle is still far from complete despite combined efforts and certain advances (IPCC, 2007). The increase in Arctic cloud cover and changes of cloud properties are mainly responsible for the enhanced Arctic warming under the influence of globally augmented greenhouse gases (Vavrus, 2004). The sensitive climatic balance is further determined by the following unique environmental conditions:

- the long absence of solar radiation in winter time
- the insulated cold winter atmosphere
- frequent temperature inversions
- the usually clean and dry atmosphere
- low aerosol load with sporadic episodes of anthropogenic pollution
- the high surface albedo of sea ice and snow

These conditions lead to particular properties of clouds (multiple layer clouds, mixed-phase clouds, optically thin clouds), which interact with the specific features of the Arctic. Generally, the Arctic atmosphere is subject to a high variability of solar radiation throughout the year, and is much colder and drier compared to midlatitudes. Further, it is very clean with a typical aerosol optical depth of 0.01 at a wavelength of 532 nm, which is sporadically increased up to 0.3 during the spring time "Arctic haze" events (e.g. Herber et al., 2002). The Arctic haze consists of anthropogenic pollution, particles and gases transported into the Arctic from midlatitudes over a long range under special synoptic conditions (Stohl, 2006). It significantly alters cloud properties (Quinn et al., 2007), as more cloud condensation nuclei and ice nuclei are present than in the normally clean Arctic troposphere. Another example of an Arctic feedback mechanism is the interaction of radiation with the surface albedo. The monthly mean broadband albedo of the mostly sea ice and snow covered surface in winter

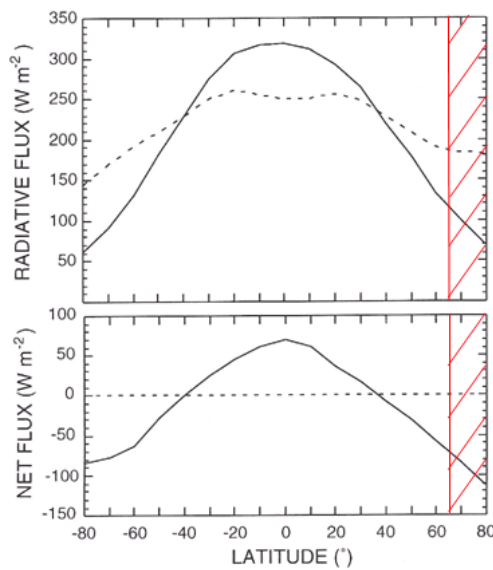
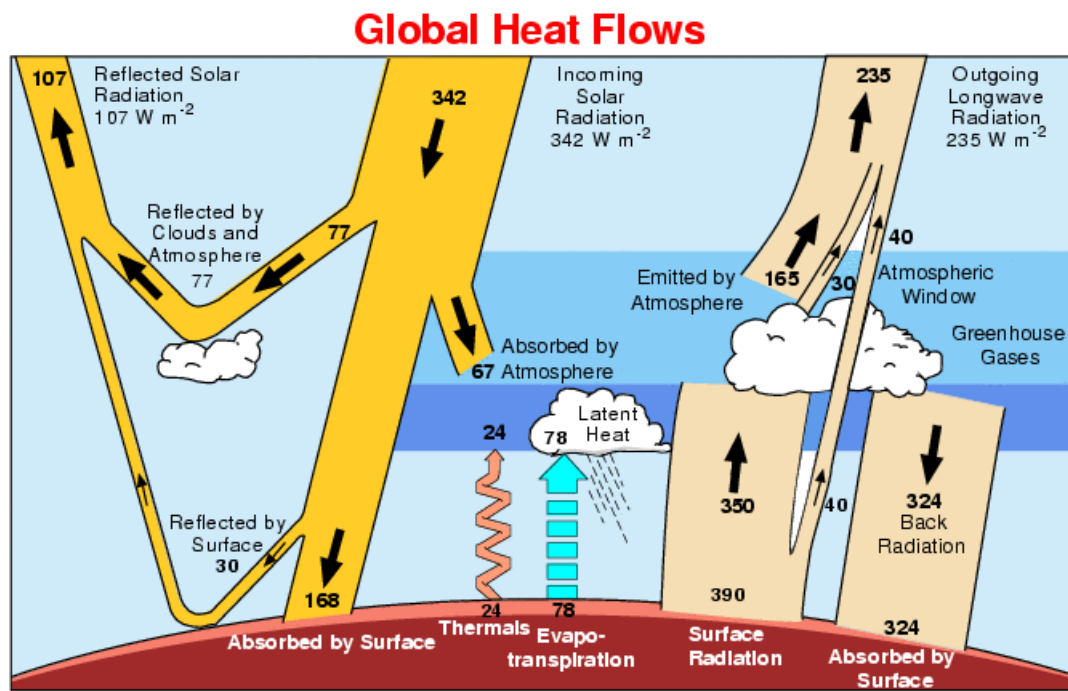


Figure 1.1, top: Zonally averaged absorbed solar radiation (solid line) and emitted terrestrial radiation (dashed line). Bottom: Net radiation (solar minus terrestrial) of the Earth surface (Fig. 11.4 from Visconti, 2001). The Arctic region with its radiation deficit is shaded in red.

exceeds 0.7 (Wyser et al., 2008). In summer, the monthly mean surface albedo in the Arctic reaches a minimum of about 0.3 (Wyser et al., 2008). Then, more solar radiation is absorbed by the less reflecting surface if cloudiness is reduced, resulting in enhanced snow and sea ice melt (Kay et al., 2008). This constitutes a positive feedback mechanism leading to further surface warming.

In order to quantify changes in the Arctic, it is essential to comprehend the complex processes that determine Arctic clouds. The understanding of clouds is advanced both by the evaluation of observational cloud data and model experiments, with the ultimate goal of implementing the results in climate models. However, to date, not all cloud mechanisms are understood well enough for the successful representation in cloud simulations.

Of all atmospheric constituents, water is the most variable in space and time and occurs in its three thermodynamic phases. Clouds have a significant influence on the Earth's surface radiation budget (Fig. 1.2, Kiehl and Trenberth, 1997, Ramanathan et al., 1989). In the Arctic the annual cloud fraction amounts to around 80 % with predominant low-level clouds up to 70 % of the time from spring to fall (Curry and Ebert, 1992). Specific Arctic cloud characteristics include the occurrence of liquid cloud droplets at low temperatures (Intrieri et al., 2002a, Turner, 2005), the formation of multiple cloud layers (Verlinde et al., 2007, Luo et al., 2008) and optically thin clouds in winter (Wyser et al., 2008). Mixed-phase clouds, consisting of different layers of predominantly liquid water droplets or mainly ice particles within the same cloud, are challenging to reproduce in simulations (e.g. Harrington et al. 1999, Morrison et al. 2008). They occur frequently in the Arctic from spring to fall (Intrieri et al., 2002a), thus influence the radiation budget significantly. The mechanisms allowing their persistence over several days and sometimes up to weeks are not entirely understood and therefore subject to intense investigations. Midlevel mixed-phase cloud were for a long time overlooked in atmospheric science (Fleishauer et al., 2002), and have not been as thoroughly investigated in the Arctic as boundary layer and cirrus clouds. However, the influence of midlevel clouds on the radiation budget and on precipitation was acknowledged, and they were included in the European Centre for Medium-Range Weather Forecasts (ECMWF) model. The common phenomenon of multiple cloud layers in the summer boundary layer is



Kiehl and Trenberth 1997

Figure 1.2: Diagram of the Earth's radiation budget. The impact of clouds on solar and terrestrial radiation is significant. Picture from Kiehl and Trenberth (1997).

important for radiative transfer calculations, but difficult to observe by remote sensing only. As the individual cloud layers are mostly optically thick, observations may be limited to the cloud layers closest to the instruments, without penetrating beyond. In the free Arctic troposphere, such observations have not often been performed (Hobbs et al., 2001). Optically subvisible clouds at low and midlevel altitudes were identified to cause diamond dust, ice precipitation out of "cloudless" sky (Intrieri and Shupe, 2004). Their radiative effect is small compared to the optically thick clouds in summer, but not well quantified for the Arctic winter atmosphere.

As the Arctic represents a remote area with little human activity, few information about the atmosphere is available compared to the dense coverage of measurement sites in the Northern hemisphere. Therefore, extensive measurement campaigns and remote sensing by satellite observations are crucial for cloud investigation. From satellite infrared imagery the coverage with Arctic clouds can be assessed year-round independent of the presence of solar radiation, which is absent for long periods during polar night (e.g. Schweiger et al., 1999). However, satellite remote sensing provides a data source with higher uncertainties than in the midlatitudes, as the surface albedo of snow and ice is very similar to the albedo of clouds and hence difficult to distinguish (King et al., 2004). Cloud screening algorithms therefore need special treatment in the Arctic. Further, the upper cloud layers and cloud top altitudes tend to be overestimated by satellite observations compared to ground-based measurements, as the instruments do not penetrate optically thick cloud layers (Shiobara et al., 2006). Nevertheless, the International Satellite Cloud Climatology Project (ISCCP, Rossow et al., 1996) retrieved a series of comprehensive global data sets on clouds, surface and atmospheric information with a grid spacing of 280 km. In the polar regions, data are based on the Advanced Very High Resolution Radiometer (AVHRR) on board of the National Oceanic and Atmospheric Administration (NOAA) polar orbiting satellites. Recent active remote observations from space (Cloud-Aerosol Lidar and Infrared Pathfinder Satellite Observations, CALIPSO, Winker and Trepte, 2007, and radar on board of CloudSat, Stephens et al., 2002) provide

much more detailed cloud observations with a vertical resolution in the range of 30 m and a horizontal along-track resolution in the order of 1 km.

However, serious progress in satellite retrieval needs the evaluation from dedicated field experiments. Also for further understanding of cloud properties and processes, additional ground-based and airborne Arctic observations are necessary. Data interpretation and the validation of clouds in models can only be improved by a combination of simultaneous measurements with active and passive radiation sensors and in situ instrumentation. The Third International Polar Year (2007/2008) focused on research activities in the polar regions (Allison et al., 2007). In this context, the international Arctic Study of Tropospheric Aerosol, Clouds and Radiation (ASTAR) was conducted in the surroundings of Svalbard (approximate location 10-20° E, 76-80° N) in March and April 2007. The schedule was chosen to capture the typical spring time aerosol pollution. However, the synoptic conditions of this particular year provided clean air. Besides the Arctic haze, one central aim of the campaign was the investigation of Arctic clouds.

1.2 Objectives of the thesis

The aim of the thesis is the airborne lidar investigation of Arctic clouds. Airborne lidar measurements provide a height-resolved intersection of the atmospheric structures, which can be used as an onboard guiding tool for further in situ observations. Lidar investigations of optically thick mixed-phase clouds, which attenuate the laser pulses significantly, are a recent development. Methods were considered for the purpose of satellite data evaluation (Hu et al., 2001, 2006, 2007, You et al., 2006). Airborne lidar observations of such clouds were reported by Quante et al. (2000), and Gayet et al. (2007). So far, airborne backscatter lidar measurements served mainly to investigate aerosol (e.g. Davis et al., 2000, McGill et al., 2003), optically thin cirrus and contrails (e.g. Uthe et al., 1998), and polar stratospheric clouds (Tsias et al., 1999), or to determine cloud altitude (Flamant et al., 1997, Frey et al., 1999). Based on case studies of the ASTAR 2007 campaign, the following scientific results were obtained:

- With airborne backscatter and depolarization lidar (light detection and ranging), concomitant solar spectral radiation and in situ instruments, unique cloud observations above the inaccessible Arctic Ocean were performed. Mixed-phase boundary layer clouds were probed, which are of particular importance for the surface radiation budget (Shupe and Intrieri, 2004). The behaviour of mixed-phase clouds at the intersection of two different air masses was observed. In the mixing zone, the cloud was completely glaciated. Further, multi layer mixed-phase clouds at midlevel altitudes were probed.
- The radiative forcing of an optically thin midlevel cloud was determined. This cloud type is difficult to observe with satellite instruments, and neither its frequency of occurrence nor radiative effects in the Arctic have been analyzed in detail. However, the data set of the Surface Heat Budget of the Arctic Ocean (SHEBA) experiment suggests that optically thin clouds occur regularly, especially in winter, and influence the radiation budget (Wyser et al., 2008).
- The observations were analyzed in the context of ECMWF analyses. Lidar data confirmed the cloud existence and cloud altitude calculated by ECMWF analyses, as well as the mixing of two different air masses. Further, lidar and in situ data served to quantify shortcomings of the ECMWF cloud analyses concerning the distribution of liquid and ice condensate in mixed-phase clouds. The results are in agreement with the findings of Beesley et al. (2000). The differences can be attributed to the

representation of cloud phase as a function of temperature in the ECMWF model, which is similar to the parameterization described in 1.3 for a regional climate model. An improved cloud treatment in the model and further validation with airborne lidar and in situ observations are necessary to overcome the disagreement.

- For future airborne studies of the typical boundary layer mixed-phase clouds in the Arctic, the results of the thesis suggest the simultaneous deployment of nadir lidar and spectral radiation instruments onboard an aircraft flying above the clouds. In situ cloud measurements are recommended to be performed synchronously or with a small time delay to the remote sensing measurements. The best outcome for cloud observations can be expected for measurements using two coordinated aircraft, one carrying the remote sensing, one the in situ instrumentation.

1.3 Motivation: Arctic clouds in climate models

As further motivation for the research of Arctic clouds, their representation in a current regional climate model is presented. Cloud parameterizations in climate models have to consider the different microphysical and optical properties and associated radiative effects of the broad variety of Arctic tropospheric clouds, ranging from low-level boundary layer stratus to high-altitude cirrus. Clouds are one of the major sources of uncertainty for climate models (Corell, 2004). The representation of Arctic clouds remains an open task for numerical simulations and experiments, and even more for global and regional weather and climate prediction models (Inoue et al., 2006). Especially mixed-phase clouds are difficult to parameterize (Fridlind et al., 2007; Luo et al., 2008).

The HIRHAM (acronym composed of High-Resolution Limited-Area Model, HIRLAM, and ECMWF, Hamburg, ECHAM, Christensen et al., 1996) is a three-dimensional regional atmospheric climate model, which is used for the Arctic region in the Atmospheric Research group at the Alfred Wegener Institute for Polar and Marine Research (AWI), Potsdam. It is based on the ECHAM4 general circulation model, which resulted from the ECMWF model, modified and extended in Hamburg. The standard horizontal resolutions are $1/6^\circ$ and $1/2^\circ$, the latter corresponding to 50 km x 50 km grid cells. There are 19 vertical levels from the surface up to 10 hPa in a hybrid coordinate system, i.e. following the orography near the surface, with smaller vertical distance between two layers at lower altitudes in order to be able to reproduce small-scale boundary layer features. At the boundaries of the model area, HIRHAM is driven by ECMWF analyses or the ECHAM4 general circulation model. The horizontal wind components, surface pressure, temperature, specific humidity and cloud water are prognostic variables.

Clouds in HIRHAM are implemented on two different scales (see Chapter 3 in Pfeifer, 2006). Large-scale cloud properties with a dimension larger than the distance of neighboring grid points can be explicitly resolved, while sub-grid scale clouds have to be parameterized. The large scale stratiform cloud scheme includes sub-grid scale cloud formation. Sub-grid cloud properties are represented in the large-scale cloud scheme by including the fractional cloud cover, based on relative humidity exceeding a critical value. Large-scale prognostic variables, which are explicitly calculated, are water vapor and total cloud water. The following physical processes are included for the calculations: condensation of water vapor and evaporation of cloud water, evaporation and formation of precipitation by coagulation (cloud droplets) and sedimentation (ice crystals). The fraction of ice water content is determined diagnostically as a non-linear function of temperature, with pure water clouds for temperatures above 0°C , pure ice clouds at temperatures below -40°C , and a mixture of both in between. The cloud ice and water distribution determined by the temperature is assumed to be homogeneously mixed within one specific cloud layer.

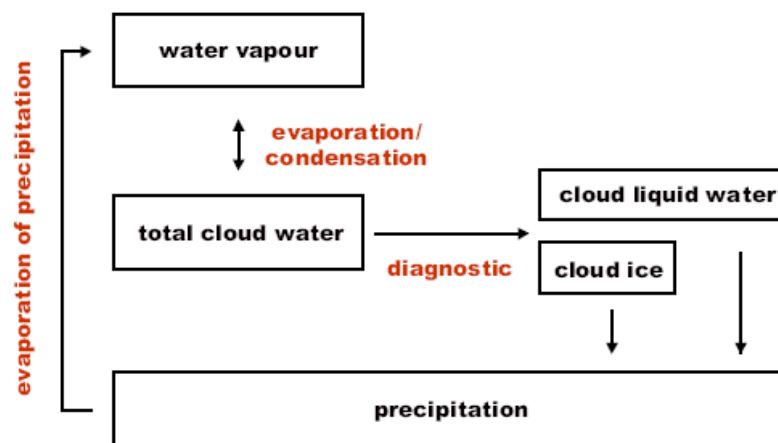


Figure 1.3: Schematical view of the cloud microphysical parameterization in HIRHAM. The arrows indicate the physical processes which are implemented. Specific humidity (water vapor) and total cloud water are prognostic variables, while the partitioning into cloud liquid water and cloud ice is a diagnostic function of temperature.

For warm clouds, precipitation is achieved by the processes of autoconversion (collision and coalescence) of cloud droplets to rain drops and the collision of falling big drops with other cloud droplets. The autoconversion rate is different for maritime and continental air masses, taking into account the aerosol load acting as cloud condensation nuclei. For maritime clouds, the amount of condensation nuclei is smaller, leading to fewer and larger cloud droplets. Thus the conversion rate for rain is higher above the open ocean, leading to a shorter cloud lifetime than above land. For cold clouds, the precipitation of ice crystals due to gravitational sedimentation is implemented, depending on the ice water content, mixing ratio, and air density. This process is about an order of magnitude more efficient than the removal of liquid water by autoconversion.

In the sub-grid cloud scheme, cumulus convection is parameterized by a one-dimensional cloud model which is based on the diabatic warming from latent heat exchange, vertical transport of moisture, heat and momentum in convective updrafts and downdrafts, and entrainment / detrainment processes with ambient air. The results describe an ensemble of convective clouds, characteristic for a grid cell. The cloud base is determined as the lowest level at which a positively buoyant ascending air parcel reaches condensation. The cloud top is the first level where the ascending air parcel becomes negatively buoyant. The clouds of interest for the Arctic region are clouds of shallow and midlevel convection. Clouds of shallow convection are supplied with moisture evaporating from the surface. Turbulent entrainment is quite high, resulting in a large exchange with the surrounding air. In contrast, midlevel convection is related to large-scale vertical velocity and moisture convergence. It is decoupled from the surface, as the boundary layer is often capped by a strong temperature inversion prohibiting the exchange of energy and moisture. Midlevel convection occurs typically in rainbands at warm fronts or in the warm sectors of low pressure systems. The precipitation rate in all convective cloud types is proportional to the total water content of the cloud. The sub-grid convective clouds are coupled to the large-scale cloud scheme by handing over the convective cloud liquid water. Detrainment of cloud water is included in terms of the transport rate of cloud water in the condensation scheme and serves as a source for stratiform cloud formation. The temporal evolution of internal processes in sub-grid scale clouds are not considered in the model.

The main shortcoming of current climate models is the treatment of cloud phase. As described above for the HIRHAM model, the ice fraction of mixed-phase clouds is determined only as a

function of temperature, which is in contradiction to observational facts. Measurements show that mixed-phase clouds cannot be represented adequately by a temperature proxy alone (McFarquhar et al., 2007, Boudala et al., 2004, Korolev et al., 2003, Pinto et al., 2001). As a consequence, the frequently observed existence of liquid droplets at temperatures below 255 K (-18 °C, e.g. Turner, 2005) is underestimated by regional climate models (Sandvik et al., 2007), weather prediction models (Gayet et al., 2009) and general circulation models (Vavrus, 2004). The interactions between water vapor and cloud ice or cloud liquid water and cloud ice, like the Wegener-Bergeron-Findeisen process (Wegener, 1911, Bergeron, 1935, Findeisen, 1938), i.e. the growth of ice particles at the expense of water droplets, are not represented in the HIRHAM model at all. Besides, the typical vertical distribution in Arctic mixed-phase clouds, with a small, predominantly liquid water layer on top and ice dominated cloud bottom (Shupe et al., 2008, Harrington et al., 1999), are not resolved. However, the effect on radiative transfer modeling is substantial, as mainly the upper cloud layer is responsible for shortwave cloud forcing (Ehrlich et al., 2009).

For May 1998, an intercomparison of different regional climate models and the observational SHEBA data set was achieved. HIRHAM underestimated clouds, which resulted in a large bias for shortwave solar radiation as well as for longwave terrestrial downward radiation. Further, too little precipitation was modeled (Inoue et al., 2006). Another regional climate modeling intercomparison evaluated simulations of Arctic clouds and radiation processes for the data set of the year-round SHEBA observations. While there was general agreement of the simulated radiation with measurements, the regional climate models, including HIRHAM, were not able to reproduce cloud cover realistically (Wyser et al., 2008). This affects the radiation balance as well as the interaction of surface, clouds and radiation in the models and may lead to biased estimations of e.g. sea ice cover (IPCC, 2007).

1.4 Structure of the thesis

After an overview of Arctic clouds in Chapt. 2, the theoretical background of lidar observations is exposed in Chapt. 3. The lidar technical setup, own modifications performed prior to the campaign, and the data evaluation scheme are presented in Chapt. 4. The measurements and atmospheric conditions during the ASTAR 2007 campaign are exposed in Chapt. 5. Chapter 6 presents a case study of a subvisible midlevel Arctic ice cloud. In a closure experiment with airborne lidar, in situ and albedometer observations, the radiative effect of the cloud was quantified. Chapter 7 is devoted to the investigation of Arctic mixed-phase clouds performed during the ASTAR 2007 campaign. Two cases of boundary-layer mixed-phase clouds and a midlevel double layer cloud are analyzed in the context of the meteorological situation. Their structure and the cloud phase is characterized. The observations of one cloud are further compared with satellite borne lidar data and ECMWF analyses. Finally, Chapt. 8 provides a summary and conclusions, as well as an outlook on further projects with the airborne lidar system. The implementation of an advanced module of cloud microphysics in a numerical weather prediction model and the validation with a set of airborne and satellite borne lidar data is suggested.

2 Tropospheric Arctic clouds

This chapter provides an overview about tropospheric Arctic clouds and their special properties. Like in other parts of the world, cloud formation and evolution processes are generally controlled by the large-scale synoptic situation, the availability of moisture, the presence of cloud condensation nuclei (CCN) and ice forming nuclei (IFN), radiative cooling, as well as vertical and horizontal mixing. The typical macrophysical properties of Arctic clouds (cloud cover, vertical structure and thermodynamic cloud phase) are analyzed in Sect. 2.1. The physical processes and cloud interactions are discussed in Sect. 2.2. Finally, the radiative impacts of Arctic clouds are specified in Sect. 2.3.

2.1 Macrophysical cloud properties

Different data sets (e.g. Polar Pathfinder Data Set derived from various NOAA satellites, <http://nsidc.org/data/nsidc-0027.html>, ISCCP data set derived from AVHRR) show that the total Arctic cloud cover is typically in the range of 70-95 % throughout the year (Schweiger et al., 1999). An example for ground-based cloud observations is the one-year SHEBA experiment off the North American Arctic coast, where cloud cover was found to be 85 % on average (Intrieri et al., 2002a). Cloudiness increases with sunlit season (Key et al., 2004). Winter is the season with least cloud cover (70 % during SHEBA, Intrieri et al., 2002a).

Vertically, the clouds can be divided into low boundary layer clouds (up to the 800 hPa level), midlevel clouds (800 - 400 hPa) and high cirrus clouds (above the 400 hPa level) according to the ECMWF classification. The height interval of midlevel clouds corresponds to an altitude of roughly 1800 m to 6500 m in the Arctic (spring time). Another definition for midlevel clouds is that both cloud base and cloud top are located between 1500 m and 5500 m (Pinto et al., 2001). Midlevel clouds are situated in the free troposphere, between boundary layer clouds and high cirrus. The term cirrus is used here for clouds above the pressure height of 400 hPa, around 6500 m, up to the tropopause region. Each height interval exhibits characteristic cloud properties.

In the Arctic boundary layer, stratus layers and convective cloud streets (Houze, 1993) are the prevailing cloud types. They occur over large areas (cloud fields of several 100 km diameter) and mainly in clusters (McFarquhar and Cober, 2004). The small-scale structures range from a few 100 m to some km (Gultepe et al., 2000). The upper cloud part often shows fluctuations of concentration and liquid water path with a typical distance of 1 km (Tsai and Jayaweera, 1984).

The Arctic boundary layer in summer time is characterized by the frequent occurrence of geometrically thin but optically thick multi-layered stratus clouds (Verlinde et al., 2007, Luo et al., 2008). Precipitation from one layer into another (so called feeder-seeder) is observed. More than 5 different layers were reported (Intrieri et al., 2002a, Hobbs et al., 2001). During the FIRE ACE campaign in May / July 1998, Lawson et al. (2001) found geometrically small boundary layer clouds of 100-400 m thickness. The transition periods spring and fall are clearly dominated by the existence of mixed-phase clouds, consisting of different layers of liquid water and ice within one cloud. Both stratiform and convective clouds occur as mixed-phase clouds.

The cloud thermodynamic phase, i.e. the distribution of liquid water and ice water, depends on the season (liquid-only clouds in summer, Lawson et al., 2001, mainly ice clouds in winter, Intrieri et al., 2002a), altitude, temperature, and more parameters (see Sect. 2.2). Supercooled

liquid water droplets were observed year-round at temperatures down to $-34\text{ }^{\circ}\text{C}$ (Intrieri et al., 2002a, Turner, 2005).

Winter is the season with the minimum occurrence of liquid water clouds. For example during the SHEBA experiment, only 23 % of the observed clouds in December were liquid phase (Intrieri et al., 2002a). 73 % of the Arctic clouds observed in spring time contained at least some liquid water, up to altitudes of 6.5 km (Intrieri et al., 2002a).

From spring to fall, mixed-phase clouds are common in the Arctic (Intrieri et al., 2002a). Averaged over the SHEBA measurement year, 41 % of all clouds were mixed-phase (Shupe et al., 2005). They have been investigated in a number of dedicated field campaigns in the North American part of the Arctic: the Mixed-Phase Arctic Cloud Experiment M-PACE in fall 2004 (Shupe et al., 2007), the First International Satellite Cloud Climatology Project Regional Experiment Arctic Cloud Experiment FIRE ACE in May / July 1998 (Curry et al., 2000, Lawson et al., 2001), SHEBA in 1997-1998 (Intrieri et al., 2002, Turner, 2005), Beaufort and Arctic Storms Experiment BASE in September / October 1994 (Curry et al., 1997, Pinto et al., 1998) and by the evaluation of satellite data (e.g. Key and Intrieri, 2000). Similar extensive ground-based and airborne data sets for the European Arctic are missing. Here, studies of mixed-phase clouds have been performed during the Radiation and Eddy Flux Experiments REFLEX in September / October 1991, March 1993 and June / July 1995 (e.g. Hartmann et al., 1997) and the ASTAR campaigns near Spitsbergen in June 2004 and March / April 2007 (Gayet et al., 2007, 2009). Further, Arctic clouds were studied during the Polar Study using Aircraft, Remote Sensing, Surface Measurements and Models, of Climate, Chemistry, Aerosols, and Transport (POLARCAT) campaigns from Northern Sweden in April 2008 and Greenland in July 2008 (Law et al., 2008). Due to different possible pollution pathways (Stohl, 2006) and different ambient conditions (especially the western part of Spitsbergen being warm for its location, caused by the influence of the North Atlantic Current) it is not clear whether findings from the North American part of the Arctic can be applied in the European Arctic.

The typical vertical structure of mixed-phase clouds consists of a layer dominated by liquid water droplets on top, which can be up to several 100 m deep, and ice crystals below (Pinto et al., 1998, Shupe et al., 2008). The processes involved in the formation of mixed-phase clouds are described in Sect. 2.2. The ice part of the cloud often extends down to only some 100 m above sea level, with snow precipitating out of the cloud to the surface (Pinto et al., 1998). The liquid fraction generally increases with height in the cloud, although small patches of ice can be found at any height throughout the cloud (McFarquhar et al., 2007, Ehrlich et al., 2009). No unique empirical relationship of liquid fraction related to temperature was found (Pinto et al., 2001, Korolev et al., 2003, Boudala et al., 2004, Mc Farquhar et al., 2007).

Unlike boundary layer clouds, midlevel clouds can occur independently of moisture feeding from the open sea. They can be related to synoptic scale atmospheric events. Optically thin clouds as well as mixed-phase clouds are observed in this altitude range (Lampert et al., 2009a, Lampert et al., 2009b). Individual layers of midlevel mixed-phase clouds often have a geometrical thickness smaller than 100 m (Hobbs et al., 2001). The temperatures at midlevel cloud altitudes cover a wide range and allow the existence of liquid, mixed-phase and ice clouds. The existence of the ice phase was observed both due to ice nucleation within the cloud and seeding from a higher cloud layer (Pinto et al., 2001).

Cirrus clouds often form in connection with large scale synoptic conditions. However, pure ice clouds can be found from altitudes as low as 2 km in the Arctic throughout the year.

2.2 Physical processes and interactions

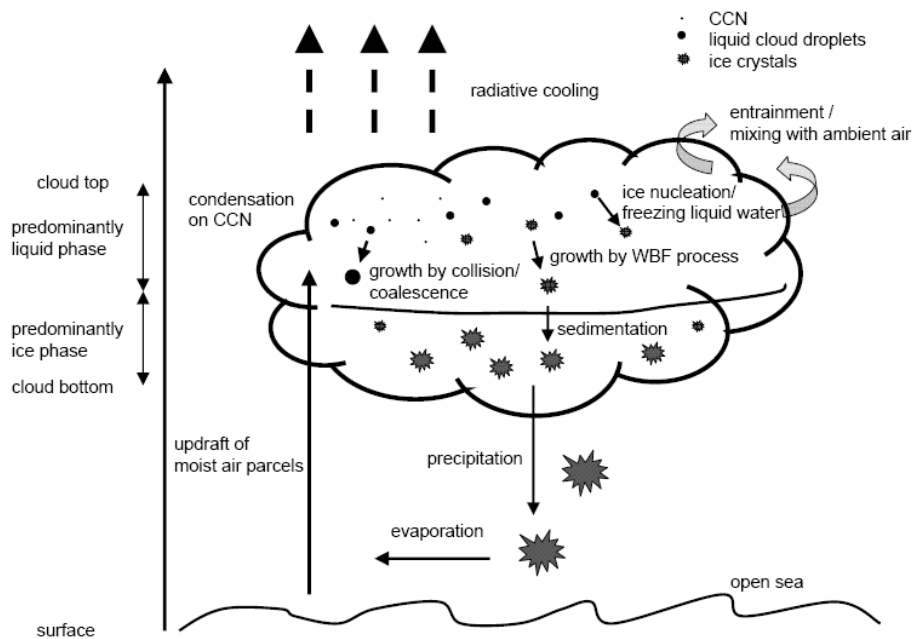


Figure 2.1: Schematic overview of the processes taking place in a mixed-phase cloud. From the open sea, moist air parcels ascend in updraft regions. They condense on cloud condensation nuclei (CCN) in the upper part of the cloud, which experiences radiative cooling. Small liquid water droplets grow by autoconversion. Few ice crystals form by ice nucleation (see text) and grow by the Wegener-Bergeron-Findeisen (WBF) process. Large ice crystals sink by sedimentation, leading to a predominantly liquid cloud top and a glaciated cloud base. Ice crystals precipitate out of the cloud, and often evaporate above the surface. Entrainment processes couple the cloud with ambient air.

Generally, for the formation of clouds, moist air parcels have to reach saturation. Water vapor is provided by the evaporation of liquid droplets, ice crystals and ocean water, or advection processes. In the presence of CCN or IFN, the water vapor condenses as cloud droplets or ice crystals (heterogeneous nucleation). Gas-to-particle conversion processes (homogeneous nucleation) are favored in a moist, but predominantly clean atmosphere. The formation of ice crystals can be initiated by contact freezing (a supercooled droplet freezes when contacted by an ice nucleating aerosol), condensation freezing (the ice phase forms as supercooled liquid water condenses on CCN), immersion freezing (an ice nucleating aerosol is immersed in a supercooled droplet, and the droplet freezes when it cools sufficiently) or by deposition of water vapor on existing ice.

In warm, purely liquid clouds, droplets grow by condensation in a supersaturated environment and by colliding and coalescing with other cloud droplets (autoconversion). The growth by condensation out of the gas phase is determined by the supersaturation, and inversely proportional to the radius of the droplet. Thus, the growth process proceeds quickly at the beginning and slows with increasing droplet, leading to a typical droplet radius of around 10 μm . Further growth is achieved by collision and coalescence processes. Larger droplets, originating e.g. from water condensed on giant CCN or turbulence and subsequent fluctuations of supersaturation, have a higher fall speed and collide with smaller droplets, which can result in coalescence. The efficiency of collision and coalescence increases rapidly with droplet radius (Wallace and Hobbs, 2006).

In cold clouds at temperatures below 0 $^{\circ}\text{C}$, supercooled liquid water droplets as well as ice crystals may occur. A glaciated cloud consists of cloud particles in the ice phase only. In a

mixed-phase cloud, both liquid cloud droplets and ice crystals coexist. However, mixed-phase clouds are only stable under certain conditions. Generally, one would expect the quick glaciation of the entire cloud due to the growth of ice crystals at the expense of liquid water droplets (WBF process). This is caused by the higher supersaturation of water vapor with respect to ice than to liquid water. For this reason, water vapor condenses preferably on existing ice particles. Thereby, the water vapor pressure in the vicinity of the growing ice crystal is lowered below water saturation, leading to the evaporation of adjacent droplets. Other possible growth mechanisms in cold clouds are riming (ice particles collide with supercooled water droplets, which freeze onto them) and aggregation after the collision of ice crystals (Wallace and Hobbs, 2006).

For the onset of precipitation, ice crystals have to reach a certain size. The conversion of liquid cloud droplets to ice and snow depends on the cooling rate (determined by radiative cooling, latent heating, turbulent entrainment, large-scale subsidence and advection) and the concentration and type of IFN. The formation of ice crystals by condensation-freezing and contact nucleation depletes cloud liquid water. Precipitation of ice crystals effectively diminishes the total water content.

Mixed-phase clouds constitute the prevailing feature of Arctic boundary layer clouds. A schematic overview of the processes taking place in this cloud type is given in Fig. 2.1. Relatively warm and moist air parcels ascend from the open ocean. During this process, they are cooled adiabatically, resulting in increased relative humidity. If supersaturation with respect to both ice and water is reached, supercooled liquid droplets and ice crystals form and grow simultaneously. As generally less IFN than CCN are present in Arctic clouds (Rogers et al., 2001), less ice crystals are produced. A threshold vertical velocity is necessary for ascending air parcels, which is determined by the concentration of IFN, the size of cloud particles, temperature and pressure (Korolev and Mazin, 2003). Further, a threshold vertical distance for the lifting is needed (Korolev and Field, 2008). The formation of mixed-phase clouds can therefore be hindered by a temperature inversion, which is usually associated with the existence of boundary layer clouds (Curry et al., 1997).

Supersaturated droplets may form in an air parcel saturated with respect to water if the condensate supply rate exceeds the diffusional growth of the ice crystals (Rauber and Tokay, 1991). The formation of supercooled liquid cloud droplets thus depends on the imbalance of available water vapor and the formation of ice as well as on dynamic effects like mixing and entrainment, and evaporation processes. At cloud top, small ice crystals predominate, as bigger crystals tend to sink down by gravitation. The mass growth rate is proportional to the ice crystal diameter, thus limited for the few small ice crystals found at cloud top. The depth of the liquid layer depends on temperature, with deep water layers for relatively warm clouds ($-5\text{ }^{\circ}\text{C}$ to $-10\text{ }^{\circ}\text{C}$) and a shallow liquid layer for temperatures about $-30\text{ }^{\circ}\text{C}$ (Rauber and Tokay, 1991). In warmer clouds, fewer IFN are activated, so the WBF process proceeds slowly, ice crystals sink down fast enough before the cloud is completely glaciated. For optically thick clouds, cloud-top radiative cooling becomes stronger, leading to further vertical mixing. Frequently, ice crystals fall out of mixed-phase clouds down to sea level (e.g. Pinto et al., 1998, Gayet et al., 2009). A considerable amount of fresh water is settled over the Arctic Ocean accordingly (Gayet et al., 2009).

In summary, processes in mixed-phase clouds, ensuring their persistence over days and sometimes weeks, are still poorly understood (e.g. Harrington et al. 1999, Morrison et al. 2008). Their life time critically depends on temperature, ice concentration and also the habit of the ice crystals (Harrington et al., 1999). Jiang et al. (2000) and Morrison et al. (2008) showed that also the number of ice forming nuclei and the ice particle concentration is crucial to maintain the mixed-phase clouds, which dissipate quickly if the ice concentration gets too high and the ice crystals grow by the WBF process. This leads to glaciation and precipitation of the cloud, shortening the cloud lifetime. Evidently, updrafts combined with the availability

of water vapor are necessary for the formation and stability of mixed-phase clouds (Korolev and Isaac, 2003, Shupe et al., 2007, Korolev and Field 2008) which form above the open ocean.

Boundary layer clouds are influenced by different macrophysical processes. For cold polar air advected over the warmer open ocean, convective clouds form. If warm and moist air flows over the Arctic Ocean, clouds tend to form near the surface, often in different layers. Also frontal systems and occlusions are sources of boundary layer clouds.

A common phenomenon in the Arctic boundary layer are multiple cloud layers. The following mechanisms have been proposed to explain the formation:

- a "greenhouse" effect in the case of a temperature inversion: the middle of a cloud layer is warmed by the absorption of solar radiation and evaporates, while the uppermost and lowermost parts of the cloud are dominated by cooling as they emit longwave radiation towards space and the colder surface, respectively (Herman and Goody, 1976)
- different formation mechanisms of the two layers: the upper cloud layer forms by weak ascent and entrainment, the lower one by advective processes (Tsay and Jayaweera, 1984)
- radiative cooling in a temperature and humidity inversion: a cloud layer near the inversion peak forms. Further radiative cooling results in mixing of the cloud, in a way that the cloud base is colder than the surface. The air above the surface is then warmer than the surface and the upper-level cloud base, cools and condenses, forming the second and possibly even more layers (McInnes and Curry, 1995)
- Formation out of precipitation: precipitation from one single cloud layer evaporates below the cloud and, by radiative cooling of the cloud, condensation of the water vapor is reached. This results in a second, lower cloud layer (Harrington et al., 1999).

The interaction of clouds and aerosol particles influences significantly the cloud radiative properties and cloud life cycle. The cloud droplet concentration depends on the available aerosol acting as cloud condensation nuclei. Their number size concentration, size and chemical composition play a crucial role. In liquid clouds, soluble aerosol modifies the cloud microphysical properties, as the occurrence of more CCN leads to smaller diameters of cloud droplets (indirect aerosol effect, Lohmann and Feichter, 2005). Smaller cloud particles persevere longer in the atmosphere, as they need to grow more before sinking down and falling out. This implies an increased lifetime of clouds. Some aerosols, consisting mainly of insoluble, hydrophobic components, not much sulfate, initiate the formation of ice crystals (Rogers et al., 2001, Lohmann and Feichter, 2005). The fraction of all aerosol particles which act as IFN in comparison with CCN was observed to be very low in Arctic clouds (0-0.02, Rogers et al., 2001). The interaction with enhanced tropospheric aerosol load like the anthropogenic Arctic haze phenomenon might be substantial. Garrett et al. (2004) describe that the cloud microstructure is altered significantly by the aged aerosol. The Arctic haze particles consisting of sulfate act as effective CCN, whereas metallic oxides act as efficient IFN (Rogers et al., 2001).

On the other hand, scavenging by precipitation is an important sink for aerosols. Pinto et al. (2001) describe minimum CCN concentrations directly below low-level precipitating clouds. Also at cloud top, depleted aerosol concentrations were observed. This might be the result of nucleation scavenging. Cloud layers can also be a source of aerosols in the case of detrainment processes.

The radiative interaction of clouds with the surface is especially important in the Arctic due to the high surface albedo of snow and sea ice. Shallow convective cloud cells form, if relatively cold air is advected over the warmer open ocean. For moist air advected over ice covered

regions, a stable boundary layer forms, where stratus cloud formation is associated with isobaric cooling. Curry et al. (1997) report deeper cloud decks and a higher cloud fraction for clouds advected from the open ocean to sea ice in the Beaufort Sea. If the updraft is disturbed, e.g. above pack ice or for changing air masses, moisture supply is not available, so convective clouds are quickly glaciated (Lampert et al., 2009b). Surface changes of smaller scales like open leads also contribute to the available amount of water and CCN / IFN for cloud formation. Clouds strongly influence the surface properties by reflecting back the terrestrial and reducing the solar downward radiation. Unlike in midlatitudes, Arctic boundary layer clouds have a surface warming effect for most of the year (see Sect. 2.3), thus the melting of sea ice is supported by the increasing cloud cover in spring.

Hobbs and Rangno (1998) and Gayet et al. (2007) observed the interaction of low and midlevel clouds in the form of feeder-seeder, ice crystals and drizzle particles falling out of a higher cloud layer into a stratiform layer of liquid cloud droplets. This effect can lead to local glaciation of low level clouds with subsequent fallout of ice crystals and cloud dissipation (Campbell and Shiobara, 2008).

2.3 Radiative effects

Clouds strongly influence the radiative transfer through the atmosphere by scattering, absorbing and emitting of solar and terrestrial radiation. Arctic clouds significantly alter the surface radiation budget (Curry et al., 1996, Shupe and Intrieri, 2004) and thus the surface temperature and onset of sea ice melting in spring time. Sensitive feedback mechanisms of clouds, radiation and surface properties lead to the worldwide most pronounced warming in the Arctic for an increase in greenhouse gases (Vavrus, 2004).

The influence of clouds on the radiation budget is often specified by the magnitude of the cloud forcing CF , i.e. the difference of the net broadband solar and terrestrial infrared (IR) irradiance, F_S^{net} and $F_{\text{IR}}^{\text{net}}$, at the surface for the cloudy and the cloud free (clear) atmosphere:

$$CF = F_S^{\text{net}}(\text{cloud}) + F_{\text{IR}}^{\text{net}}(\text{cloud}) - F_S^{\text{net}}(\text{clear}) - F_{\text{IR}}^{\text{net}}(\text{clear}) \quad (2.1)$$

The absolute values of the surface warming or cooling strongly depend on the solar zenith angle as well as on cloud and surface properties. Longwave (LW) and shortwave (SW) cloud forcing are discussed separately in the following. The term "longwave" is used here for the terrestrial infrared spectral range of 5-100 μm , and the expression "shortwave" comprises the solar spectral range (ultra violet, visible and near infrared) of 0.2-5 μm . The sum (net forcing) quantifies the overall surface warming or cooling of clouds. Cloud forcing is related to cloud thermodynamic phase and microphysical properties (Harrington et al., 1999).

The longwave cloud forcing depends on the temperature and optical thickness of the cloud and has a surface warming effect. The cloud optical thickness is mainly influenced by the cloud particle size and concentration. Generally, liquid water clouds exhibit a higher droplet concentration and smaller droplet size than clouds consisting of ice particles. The LW cloud forcing further increases with liquid water path (LWP) until saturation is reached at a value of around 30 g m^{-2} (Shupe et al., 2004). For higher LWP, the clouds behave as a blackbody, and their radiation depends only on temperature T according to Planck's law:

$$I_\lambda = \frac{2hc^2}{\lambda^5} \cdot \frac{1}{e^{\frac{hc}{\lambda kT}} - 1} \quad (2.2)$$

I_λ denotes the spectral radiance, λ the wavelength, h the Planck constant, c the speed of light, and k the Boltzmann constant.

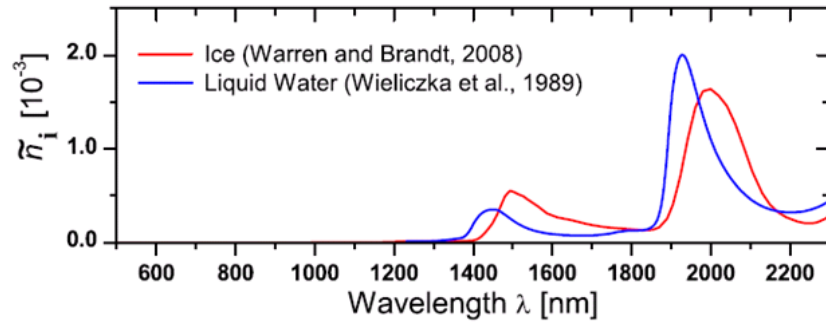


Figure 2.2: Imaginary part of the spectral refractive index \tilde{n}_i for liquid water and ice. The absorption is determined by the imaginary part of the refractive index. Provided by André Ehrlich.

Generally, low level clouds emit a higher spectral radiance due to the augmented temperature compared to midlevel and high cirrus clouds. Numerous temperature inversions in the Arctic result in clouds which can even be warmer than the surface and enhance the LW cloud forcing.

Interactions with an enhanced aerosol load may change the microstructure of clouds. For concurrent thin water clouds and high aerosol concentrations, the increase in cloud longwave emitted radiation can be substantial, with an additional surface warming of 1-1.6 °C (Garrett and Zhao, 2006).

The magnitude of shortwave radiation is subject to a strong diurnal and annual cycle determined by the solar zenith angle. The SW cloud forcing depends on the cloud microphysical and macrophysical properties and has a surface cooling effect. The usually higher particle concentrations and smaller particle sizes of liquid water clouds lead to enhanced SW forcing in comparison with ice clouds.

If the cloud droplet size distribution is shifted towards smaller droplets in higher concentrations for the same amount of water, the reflection of SW radiation will increase. An increase in aerosol concentrations results in enhanced cloud forcing, as clouds get more reflective to incoming solar radiation, which is called Twomey effect (Twomey, 1977).

Comparing the two competing effects of shortwave and longwave forcing, SW forcing plays a dominant role for a short period in the sunlit summer while LW forcing dominates almost all the year, and particularly in the dark winter season. Further, a saturation of cloud forcing, meaning that no additional radiative effect is observed for a higher liquid water path, is reached for lower values of liquid water path in the LW than in the SW (Shupe et al., 2004). The SW surface cooling still increases for clouds of increasing optical thickness while there is no additional LW surface warming.

In contrast to clouds at midlatitudes, the total net radiative effect of Arctic clouds is generally a warming of the surface for most of the year (Curry et al., 1993, Intrieri et al., 2002b), with a mean radiative forcing estimated as 30 W m⁻² by Intrieri et al. (2002b) and 40-50 W m⁻² by Curry et al. (1996). The SW surface cooling of clouds is relatively small for wintertime ice clouds combined with a high solar zenith angle (around -3 W m⁻²), and can obtain values up to -100 W m⁻² in summer months (Shupe et al., 2004). Only for some weeks in summer, the clouds have an overall cooling effect (Curry et al., 1992). This is caused by optically thick clouds with a LWP where the emission of LW radiation is saturated. The SW radiation in this case is reduced substantially.

Midlevel clouds have a smaller radiative forcing than low level clouds, but exhibit a longer period of surface cooling in summer time (Curry et al., 1992). High cirrus clouds have a small warming effect on the surface radiation budget of around 1.5 W m⁻² (see introduction of Hallar et al., 2004).

The forcing of the frequent Arctic mixed-phase clouds is of special importance for the radiation budget. In spring time, they have a net positive surface forcing (Zuidema et al.,

2005). However, the local radiative forcing of mixed-phase clouds depends on the partitioning of liquid and ice water in the clouds and can result in a surface cooling of -160 W m^{-2} for predominantly liquid water clouds (Ehrlich, 2009). As liquid droplets dominate the mass content of mixed-phase clouds, the optical properties needed for radiative transfer (single scattering albedo and asymmetry parameter) are, at a first glance, similar to pure water clouds, while they differ significantly for ice clouds (McFarquhar and Cober, 2004). As the spectral refractive indices of liquid water and ice exhibit differences in the near IR (Fig. 2.2), pure water clouds can be distinguished from mixed-phase clouds by spectral radiation measurements (Ehrlich et al., 2008). Therefore, even small amounts of ice crystals are crucial for the surface forcing of mixed-phase clouds.

3 Lidar data evaluation

The lidar principle is based on the emission of short laser pulses and the time-resolved detection of the signal scattered back from the atmosphere. The Airborne Mobile Aerosol Lidar (AMALi) used for this study is an elastic backscatter lidar system with the detection of depolarization. Therefore, the focus of the chapter is on the theoretical background of elastic lidar measurements, the fundamental processes, equations and parameters used in this work.

3.1 Scattering theory

Scattering theory describes the interaction of electromagnetic radiation and matter. Each single photon emitted by a lidar system may be influenced in different ways: there are photons that pass straight through the atmosphere without any interaction with nitrogen (N₂) and oxygen (O₂) molecules of the air or other particles. Some photons are scattered in different heights into different directions. Only a small part of them, photons that are scattered backwards without changing their energy, i.e. wavelength, can be detected with the elastic lidar system. The term “elastic” backscatter usually refers to both the Cabannes line (no change in the energy state of the scattering molecule) and the excitation of the pure rotational Raman spectrum. The rotational Raman spectrum can be neglected with small interference filters (bandwidth < 0.3 nm).

Other photons are absorbed and are lost for detection. Some of them are re-emitted quasi simultaneously at another wavelength (Raman effect). For Raman lidar systems, Raman signals at another wavelength caused by the excitation of vibrational energy states of the N₂ or O₂ molecules are analyzed. Some photons are scattered several times without changing the energy. A small part of them is collected by the telescope of an elastic lidar system. This so-called multiple scattering is described in Sect. 3.4.

3.1.1 Rayleigh scattering

Molecules and aerosol particles with a size parameter $\gamma = \frac{2\pi r}{\lambda}$ smaller than 1 are called optically small particles. λ refers to the wavelength of the incoming radiation, and r is the particle's radius. These small particles are considered free running oscillators which are oscillating due to the incoming electric field of radiation. Their interaction is described by the Rayleigh scattering theory. The cross section σ for Rayleigh scattering is inversely proportional to the forth power of the wavelength λ of the radiation:

$$\sigma = \frac{2\pi^5}{3} \frac{d^6}{\lambda^4} \left(\frac{n^2 - 1}{n^2 + 2} \right)^2 \quad (3.1)$$

In this equation, d is the diameter of the scattering particle and n the complex index of refraction. The scattering cross section for shorter wavelengths is much larger than for longer wavelengths according to the equation. The angular distribution for radiation scattered by a molecule, the molecular scattering phase function $P(\theta)$, is symmetric in forward and backward direction:

$$P(\theta) = \frac{3}{16\pi} (1 + \cos^2 \theta) \quad (3.2)$$

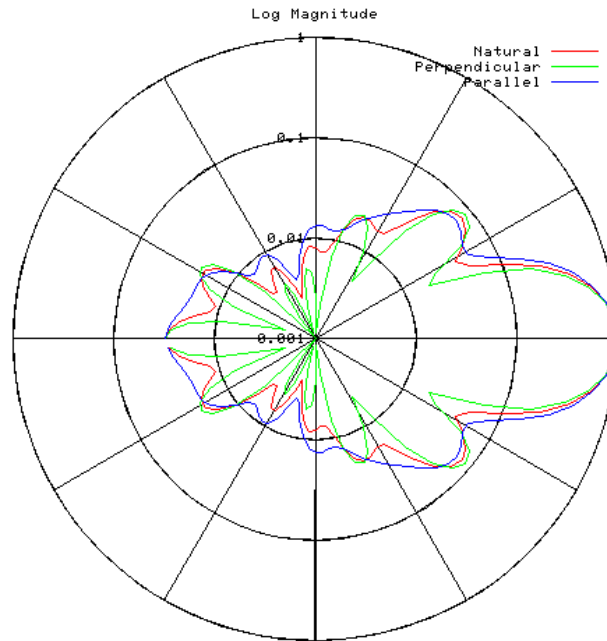


Figure 3.1: Polar graph of the Mie scattering phase function. In this illustration, radiation of the wavelength 532 nm is incident from the left, onto spheres with diameter of 1.0 μm , imaginary refractive index 1.5+0*i, and a concentration of 0.1 μm^{-3} . The different colors denote the scattering phase function for different polarization directions (Prah, 2007).

The scattering angle θ is defined as the angle between the incident and the scattered photon. Due to the omnipresence of the molecules N_2 (78%) and O_2 (21%) in the atmosphere, a Rayleigh contribution is always present in the lidar backscatter signals. It is proportional to the density, thus decreasing with altitude.

3.1.2 Mie scattering

Scattering of spherical particles with the size in the order of the wavelengths of the incoming radiation ($\gamma \approx 1$) is in general described by Mie theory. An analytical (but already difficult) solution for the phase function can be given by solving the Maxwell equations for a sphere with a certain index of refraction and radius. The phase function of the intensity of the scattered light is strongly peaked in forward direction (Fig. 3.1). Mie theory includes Rayleigh scattering and the geometrical optics ($\gamma > 40$) as special cases.

The wavelength dependence of the backscatter coefficient β can be approximated by a power law relationship:

$$\beta = \text{const} \cdot \lambda^{-\mu} \quad (3.3)$$

μ is called the Ångström exponent, with values between 4 for pure Rayleigh scattering (see Eq. 3.1) and 0 for scattering by large particles (geometrical optics).

3.1.3 Scattering of non-spherical particles

Scattering processes involving non-spherical particles are mathematically difficult to describe. In order to reproduce the measured scattering phase function of ice crystals, e.g. by the Polar Nephelometer (Sect. 5.3), data bases for different crystal shape, size and roughness have been

created as lookup tables (Yang and Liou, 1996, Jourdan et al., 2003a, Rother et al., 2006). However, determining the microphysical properties from measuring the scattering phase function constitutes an ill-posed problem. Further, the polarization direction of incident radiation is changed by scattering involving non-spherical particles (see Sect. 3.3.1).

3.2 The elastic lidar equation

3.2.1 Lidar equation

With the lidar system, the power of the laser signal scattered in backward direction to the detection unit is measured in high time resolution. This corresponds to vertical profiling of the atmosphere.

The following equation describes the backscattered laser signal, with r being the range, i.e. the distance between lidar system and scatterer:

$$P(r) = C/r^2 \cdot \beta(r) \cdot \exp(-2 \int_0^r \alpha(r') dr') \quad (3.4)$$

The backscattered power $P(r)$ is proportional to the lidar constant C , representing various technical features of the lidar system. Further, it is proportional to the backscatter coefficient $\beta(r) = \beta^{\text{Ray}}(r) + \beta^{\text{part}}(r)$, where β^{Ray} and β^{part} are the molecular Rayleigh and the particle (volume) backscatter coefficients, and twice the transmission $T(r)$, defined as the integral over the extinction coefficient $\alpha(r) = \alpha^{\text{Ray}}(r) + \alpha^{\text{part}}(r)$, as the photons pass the same path twice on the way up and down.

$$T(r) = \exp(-\int_0^r \alpha(r') dr') \quad (3.5)$$

The lidar constant C includes the system parameters, the power of the pulses emitted by the laser, the effective area of the telescope mirror A (A/r^2 is the solid angle under which a scattering particle sees the telescope mirror), the overlap function, which describes the overlap of the laser beam divergence and the field of view (FOV) of the telescope, and other parameters like the voltage and efficiency of the photomultiplier tubes and the transmission of the optical components. The overlap function is equal to unity when there is full overlap of the laser beam and the telescope field of view, which is the case for a distance larger than 235 m for the AMALi (Chapt. 4). Usually the data evaluation is restricted to a range larger than the overlap distance.

The elastic lidar equation (Eq. 3.4) can also be expressed with the signal variable S being the logarithmic range-corrected power:

$$S(r) = \ln(r^2 \cdot P(r)) = \ln C + \ln \beta(r) - 2 \int_0^r \alpha(r') dr' \quad (3.6)$$

As C contains all the information that does not depend on the range, the spatial derivative of this factor vanishes.

The differential form of the lidar equation is therefore

$$\frac{dS}{dr} = \frac{1}{\beta} \frac{d\beta}{dr} - 2\alpha \quad (3.7)$$

The lidar equation contains two unknown parameters, the extinction coefficient α and the backscatter coefficient β . Additional data or assumptions are needed for solving the equation. Without further information, the so-called attenuated backscatter coefficient can be calculated

as a preliminary evaluation of lidar data. In this case, the extinction coefficient α is neglected and set equal to zero. This is common for space borne lidar applications (e.g. Lidar Level 1 Data Product of the Cloud Aerosol Lidar with Orthogonal Polarization, CALIOP, Anselmo et al., 2006) as the atmosphere exhibits a low density and is general very clean for high altitudes. For these reasons, the extinction coefficient is negligible at high altitudes compared to the backscatter coefficient, and the transmission between the space borne lidar system and atmospheric structures is almost unity.

To solve the lidar equation (3.7), the so-called lidar ratio $LR(r,\lambda)$ is introduced, defined as the ratio of particle extinction coefficient α^{part} and particle backscatter coefficient β^{part}

$$LR(r, \lambda) = \frac{\alpha^{part}(r, \lambda)}{\beta^{part}(r, \lambda)} \quad (3.8)$$

Typical values for clouds and aerosol are around 20 sr and 30-40 sr, respectively.

After substituting the LR , and with $\beta = \beta^{Ray} + \beta^{part}$, the lidar equation (3.7) can be written in the form of a Bernoulli differential equation of grade 2:

$$\frac{d\beta}{dr} = \left(\frac{dS}{dr} + 2 \cdot \alpha^{Ray} - 2 \cdot LR \cdot \beta^{Ray} \right) \cdot \beta + 2 \cdot LR \cdot \beta^2 \quad (3.9)$$

With the Bernoulli substitution this equation can be transformed into a linear differential equation for β^{-1} and solved directly.

3.2.2 Klett evaluation algorithm

The inversion algorithm described by Klett (1981 and 1985) and Ansmann et al. (1992) is the standard method for solving the elastic lidar equation (3.7) for the backscatter coefficient. It is solved under the assumption of a known or guessed LR according to Eq. (3.8). Further, a reference value for the backscatter coefficient β_{ref} at a reference height r_{ref} at the far end of the range has to be assumed (boundary condition). If, for zenith applications, the reference height is chosen in the free troposphere or at the tropopause with very low aerosol load, there is almost no contribution by particles to the backscatter signal S_{ref} . The corresponding lidar signal can be validated with the molecular backscatter coefficient at the reference range, with the density profile calculated from radio sounding or using a standard atmosphere model.

The solution for the backscatter coefficient is

$$\beta(r) = \frac{\exp(S - S_{ref})}{1/\beta_{ref} + 2 \int_r^{r_{ref}} \exp(S - S_{ref}) dr'} \quad (3.10)$$

The solution of the lidar equation is often given in terms of the backscattering ratio BSR, defined as

$$BSR(\lambda, r) = \frac{\beta^{Ray}(\lambda, r) + \beta^{part}(\lambda, r)}{\beta^{Ray}(\lambda, r)} \quad (3.11)$$

The backscattering ratio is a dimensionless quantity. A completely clear atmosphere would have a BSR of 1. For aerosol and optically thin clouds, a typical value in the Arctic is around 2.

With the integration from the far end of the signal towards the lidar system, a stable solution of the lidar equation is found. It is only altered slightly by the noise on the signal and a wrong assumption of the backscatter coefficient at the reference altitude.

For nadir observations from the aircraft, the reference value near the ground might be given by in situ or lidar measurements at ground-based stations. For the AMALi evaluation, this method was applied whenever such data was available. However, for the case studies discussed in the thesis, it was not possible. The reference value β_{ref} can also be approached iteratively for nadir measurements with the same accuracy as for a given reference value (Stachlewska et al., 2009). An initial value is altered until the backscatter coefficient near the aircraft reaches realistic values corresponding to the low aerosol load prevailing in the free troposphere. However, routine evaluation has to be checked carefully in the case that clouds or enhanced aerosol are present at the reference height.

After a first data evaluation assuming a constant lidar ratio, the LR can be modified according to the results, with different values that are typical for individual height intervals, e.g. clouds or aerosol layers.

3.2.3 Transmittance method

The transmittance method (Chen et al., 2002) is an approach to determine the mean extinction coefficient of an aerosol or optically thin cloud layer from elastic backscatter profiles. Assuming a value for the backscattering ratio BSR below and above the cloud, the extinction in the cloud can be calculated by solving the elastic lidar equation.

If the cloud layer is situated in the free troposphere on a day without pollution, the values of the backscattering ratio above and below the cloud should even be the same. This case was also described as the slope method (Kunz and de Leeuw, 1993) for retrieving the extinction coefficient if the atmosphere can be considered as homogeneous, that is if the backscatter coefficient does not vary with range. The term $d\beta/dr$ in Eq. (3.7) vanishes. The differential equation can then be solved directly:

$$\alpha(r) = -\frac{1}{2} \frac{dS}{dr} \quad (3.13)$$

The method can also be applied for inhomogeneous atmospheric conditions, with the approximation of small homogeneous height intervals. The condition of $\frac{1}{\beta} \frac{d\beta}{dr} \ll 2\alpha$ has to be met within these intervals.

However, Kunz and de Leeuw (1993) showed that the accuracy of the slope method is not better than 10 % for small extinction coefficients ($< 0.1 \text{ km}^{-1}$), which is usually the case for Arctic aerosol and optically thin clouds.

The transmittance method provides a solution for known, but different backscattering ratios:

If $BSR(r_b)$ equals $m \cdot BSR(r_t)$ for the height of the cloud bottom r_b and top r_t , respectively, and m is known, the lidar equation (3.4) results in the following equation:

$$\frac{P(r_b)r_b^2}{C\rho(r_b)} \exp(+2 \int_0^{r_b} \alpha(r') dr') = m \cdot \frac{P(r_t)r_t^2}{C\rho(r_t)} \exp(+2 \int_0^{r_b} \alpha(r') dr') \exp(+2 \int_{r_b}^{r_t} \alpha(r') dr') \quad (3.14)$$

$\rho(r)$ represents the air density. In Eq. (3.14), the optical depth in the cloud (between r_b and r_t) is given by the last term and can be calculated straightforward. According to Nicolas et al. (1997), this value constitutes an upper limit, as diffraction leads to enhanced apparent optical depths. The mean extinction coefficient is then the optical depth divided by the cloud's geometrical thickness.

With the extinction coefficient derived from the transmittance method and the backscatter coefficient determined by the standard Klett approach, the average lidar ratio can be estimated from the elastic lidar profiles themselves. Although the error of this method is quite large (around 10 %), it can be used to verify if an assumed lidar ratio is realistic.

3.3 Depolarization and color ratio

3.3.1 Depolarization ratio

For applying the information of depolarization, the transmitted laser light has to be linearly polarized. In scattering processes with non-spherical particles, the polarization direction of the incident radiation is rotated. The (volume) depolarization ratio is defined as the ratio of the backscatter coefficients for scattering in perpendicular and parallel polarization direction, β_{perp} and β_{par} , relative to the linear polarization direction of the transmitted laser beam (Pal and Carswell, 1973):

$$\delta(r) = \frac{\beta_{\text{perp}}(r)}{\beta_{\text{par}}(r)} \quad (3.15)$$

It can also be expressed as the ratio of the perpendicular and parallel polarized elastic lidar signal P_{perp} and P_{par} with a calibration factor k including system parameters of the lidar:

$$\delta(r) = k \cdot \frac{P_{\text{perp}}(r)}{P_{\text{par}}(r)} \quad (3.16)$$

Equation (3.16) uses only the lidar signals, without the need of solving the elastic lidar equation (3.7). The depolarization ratio is calibrated with the depolarization of the molecules of air at an altitude that can be assumed to be free of additional particles. The exact value of the molecular depolarization depends on the bandwidth of the lidar interference filters (Behrendt et al., 2002, see Chapt. 4).

Spherical particles do not change the polarization direction of incident radiation in the case of backscattering processes (180°). However, the depolarization value measured by a lidar system also depends on its field of view (Hu et al., 2001). As can be seen in Fig. 3.1, the scattering function at even small angles around 180° is different for the two polarization directions.

The backscatter from non-spherical ice crystals emerges after internal reflections, which rotate the incident polarization plane (Sassen, 1991). For linearly polarized laser light, the depolarization ratio is thus a criterion to distinguish between spherical and non-spherical scattering particles. This can be spherical aerosol particles (containing soluble material) and non-spherical aerosol (e.g. soot, sea salt) as well as spherical liquid water droplets / drizzle or non-spherical ice particles. For clouds composed of ice particles, the depolarization value depends on the ice particle size and habit. In the review of Sassen (1991), the typical depolarization range is described as 40 - 50 %, although high values up to 80 % have been observed, and values near zero are reported for horizontally oriented plates (see calculations of Mishchenko et al., 1997, and observations of Hu et al., 2007).

Enhanced depolarization values can also be caused by multiple scattering (Sect. 3.4).

3.3.2 Color ratio

The term color ratio generally designs the ratio of the backscatter coefficients at different wavelengths. The color ratio serves to estimate the size of the scattering particles. However, the retrieval of the size distribution and particle density is not possible with only two wavelengths like in the AMALi system, as this constitutes an ill-posed problem. For the backscatter coefficient known at 3 wavelengths and the extinction coefficient determined independently for 2 wavelengths, an inversion code for deriving size distribution and refractive index of spherical particles was proposed by Böckmann (2001).

In this work, the definition of the color ratio C^{part} as used by Liu and Mishchenko (2001) is employed:

$$C^{\text{part}}(r) = \frac{BSR(\lambda_1, r) - 1}{BSR(\lambda_2, r) - 1} = \frac{\beta^{\text{part}}(\lambda_1, r) \cdot \beta^{\text{Ray}}(\lambda_2, r)}{\beta^{\text{part}}(\lambda_2, r) \cdot \beta^{\text{Ray}}(\lambda_1, r)} \quad (3.17)$$

In this equation, λ_1 describes the longer wavelength (532 nm for the AMALi lidar) and λ_2 the shorter wavelength (355 nm).

From the definition of the color ratio, the limit for very small particles (size of molecules) is $C^{\text{part}} = C^{\text{Ray}} = 1$ as the particle backscatter coefficients for both wavelengths converge to the Rayleigh backscatter coefficients and the terms cancel in Eq. (3.17). For “large” particles obeying the laws of geometrical optics, the particle backscatter coefficients at all wavelengths are equal and the Rayleigh backscatter coefficients depend by the power of 4 on the wavelengths, resulting in a limit value $C^{\text{part}} \approx 5$. In the sense of the two lidar wavelengths, “large” refers to particles with an effective diameter exceeding 5 μm (size parameter larger than 40). In the case of cloud observations, the color ratio helps to identify if a cloud component with particle size smaller than 5 μm was present.

3.4 Multiple scattering effects on lidar retrievals

"Multiple scattering" means that photons are not only scattered once by a molecule of the air or a particle, but several times before they are detected. The multiple scattering processes result in an ambiguous correlation of the arrival time of the photon and the distance of the scattering events, causing an afterglow effect in the lidar signals behind a cloud. When the optical depth of the scattering medium is too high (higher than about 0.1 in the case of the AMALi system, the exact value depending on the telescope field of view and the distance from the lidar system, You et al., 2006), multiple scattering effects in the lidar signal cannot be neglected. As the phase function of Mie size particles is strongly peaked in forward direction (Fig. 3.1), there is a high probability that particles scattered back to the telescope have undergone several scattering processes under small angles in forward direction. As multiply scattered photons are recorded later than photons which were backscattered once, the extinction coefficient at the cloud boundary closest to the lidar system is underestimated (Wandinger, 1998). The smaller the telescope field of view, the less multiply scattered photons are collected. The multiple scattering effect can also be exploited to obtain additional information on cloud particle size for lidar systems with multiple field of views (Bissonnette et al., 2005). For lidar systems with a fixed FOV, the relation of parallel and cross-polarized signals reveals if the scattering particles are mainly spherical liquid or non-spherical ice water.

As mentioned in Sect. 3.3.1, the depolarization of a pure water cloud consisting of spherical droplets is zero for a backscatter angle of 180° , but the value obtained by a lidar telescope strongly depends on its FOV. However, in the case of multiple scattering, photons are received which were scattered under other angles than 180° , undergoing a shift in the polarization direction. The depolarization ratio therefore increases with the number of scattering processes.

For common aerosol load and thin clouds with an optical thickness up to around 0.1 for a wavelength of 532 nm, the multiple scattering effect can be neglected for the AMALi system and is not included in the standard lidar equation. As the AMALi has a relatively wide field of view (3.1 mrad, see Chapt. 4), the lidar profiles with an optical depth above the critical value have to be checked before the evaluation of data containing clouds or aerosol.

For moderately thick clouds, which do not completely attenuate the laser signal, a possibility to take into account multiple scattering was described by Platt (1973). He proposed to introduce an additional constant η in the exponent of the lidar equation:

$$P(r) = C/r^2 \cdot \beta(r) \cdot \exp(-2\eta \int_0^r \alpha(r) dr) \quad (3.18)$$

The unknown constant η is described to have values between 0.5 and 1, and has to be determined by either theoretical calculations (assuming spherical particles) or by comparison with the optical depth from radiometric measurements. The boundary layer clouds presented in the thesis were optically too thick, and the correction could not be applied.

For thick clouds, which attenuate the laser beam completely, the lidar signal cannot be evaluated quantitatively. However, atmospheric structures with a high backscatter coefficient may still be observed due to small-scale inhomogeneities in the clouds. Furthermore, it is possible to determine the cloud phase for the layer closest to the lidar system. For clouds consisting of liquid water droplets, the depolarization value increases gradually with cloud geometrical thickness. In contrast, the depolarization ratio of pure ice clouds is enhanced immediately at the cloud boundary (Hu et al., 2001). Ice clouds consisting of different ice particle habits can also be discriminated theoretically, as they have different starting values and slopes of depolarization as a function of optical thickness (You et al., 2006). For liquid water clouds, the backscatter and the depolarization are positively correlated, while for ice clouds, the depolarization decreases with penetration into the cloud, as was observed for CALIPSO data (Hu et al., 2006, 2007).

3.5 Limits of lidar investigation for cloud observations

The lidar investigation of optically thick clouds poses serious challenges for the data evaluation. If clouds attenuate the laser pulses significantly, the quantitative evaluation of lidar profiles to determine the backscatter coefficient of the cloud is not possible. The lidar equation as presented here needs the assumption of single scattering, and the application is limited in the case of multiple scattering (see Sect. 3.4). For clouds which attenuate the laser pulses completely, not even qualitative information for the altitudes beyond the cloud can be estimated.

Generally, the lidar wavelengths are too small to derive information on particle size for typical liquid cloud droplets (radius around 10 μm) or even ice crystals (effective radius around 100 μm). In the case of mixed-phase clouds with distinct layers of liquid droplets and ice crystals, lidar is much more sensitive to the smaller droplets, and the laser pulses are quickly attenuated. For airborne nadir measurements, the combination with radar would allow to penetrate liquid cloud parts and detect the signature of ice crystals or precipitation below a cloud.

The high sensitivity of depolarization measurements to evidence even very few ice crystals (less than 1 l^{-1}) is also affected by multiple scattering in the case of few ice crystals within a predominantly liquid cloud layer (Sect. 3.4).

4 The Airborne Mobile Aerosol Lidar (AMALi)

The lidar system used to perform the airborne measurements of this work is the AMALi, acronym for Airborne Mobile Aerosol Lidar (Stachlewska et al., 2009). It was developed and built by the lidar group of the AWI Potsdam Research Unit in 2002/03 (Stachlewska et al., 2004). The entire system was constructed as small and light as possible for the operation in the Polar-2 aircraft, with limited weight and space for equipment. The AMALi was successfully deployed in the Arctic Study of Tropospheric Aerosol, Clouds and Radiation (ASTAR) in 2004 and 2007, and the Svalbard Experiment (SVALEX) in 2005.

In the framework of this thesis, the AMALi was modified as described below. Data collected during the ASTAR 2007 campaign are analyzed.

4.1 Technical setup

The AMALi is composed of four major parts: The optical unit, the lidar controller, the transient recorders and a notebook with controlling software.

Some mechanical components of the original instrument were modified at the beginning of this project in 2006, to enable the implementation of both nadir and zenith looking configuration alternatively in the Polar-2 aircraft. Before, only nadir operation was possible. Moreover, the optics was exchanged for emitting and detecting a new wavelength, 355 nm, instead of the original one of 1064 nm. This shorter wavelength promised better detection of the small particles of the expected Arctic haze.

To increase the measurement range, the detection mode was changed from analogue signals to a combination of analogue signals for short range and photon counting signals for long range detection. The detection range that should be covered in nadir configuration is limited between 2100 m and 3000 m height, resulting from the flight altitude. The upper limit of 3000 m is due to the necessary working pressure for the electronics and the laser cooling system. The minimum flight altitude of 2100 m results from eye safety calculations for possible ground-based observers and other persons. In the zenith configuration, with the laser pointing upwards, the aim is to cover the troposphere from the aircraft to the tropopause level. It is situated at a maximum of around 9 km for polar spring conditions.

The specifications of the AMALi system are summarized in Table 4.1.

4.1.1 Transmitting and receiving system

An overview of the optical unit is given in Fig. 4.1. The transmitting system includes a flashlamp pumped, pulsed Nd:YAG laser (CFR-200, Big Sky Lasers, Montana, USA) with second harmonic generator (SHG) and third harmonic generator (THG) crystals. The laser thus emits both at the green wavelength of 532 nm with an energy of about 105 mJ and at the UV wavelength of 355 nm with an energy of about 15 mJ, and a residual of the basic wavelength of 1064 nm with energy less than 45 mJ. The energy of the infrared (IR) wavelength 1064 nm is absorbed in the optical unit by a white ceramic glass absorber material called Macor, so it is not further considered here. The beam divergence for the 532 nm wavelength is 2.6 mrad; the divergence of the UV pulses is estimated by the manufacturer as 1.5 to 2.5 mrad. Radiation at both wavelengths is linear polarized, 355 nm in vertical, 532 nm in horizontal direction.

Table 4.1: AMALi specifications. Changes with respect to the original system described by Stachlewska et al. (2004) are indicated in red.

Laser wavelengths	532 nm, 355 nm (new, before 1064 nm)
Laser pulse energy	105 mJ (532 nm) 15 mJ (355 nm)
Laser pulse repetition rate	15 Hz
Laser beam divergence	2.6 mrad
Telescope type	Off-axis
Mirror diameter	10.6 cm
Telescope field of view	3.1 mrad
Detection channels	532 nm, parallel polarization 532 nm, perpendicular polarization 355 nm, unpolarized (before 1064 nm) Both analogue and photon counting mode
Interference filters	0.15 nm FWHM (532 nm) 1.0 nm FWHM (355 nm)
Range	250 – 9000 m (improved)
Range resolution	7.5 m

The pulse repetition frequency can be varied from 2 -15 Hz, but is usually set to 15 Hz for normal operation. The pulse length for the wavelength of 532 nm is given as 11.38 ns.

A double-plain mirror with high reflection coating for the two wavelengths 532 nm and 355 nm (Laseroptik, Garbsen) directs the laser pulses vertically through the perforation in the center of the detection mirror, a protection tube and a window into the sky (Fig. 4.1). Due to non perfect linear polarization, which came along with the implementation of the THG crystal, a dual wavelength waveplate (CVI Laser, USA) and a Glan-Taylor polarizer (OFR, USA) were included in the tube. The waveplate is specially designed for 532 nm and 355 nm and shifts the polarization of the 532 nm wavelength by $\lambda/2$ to match the polarization of the 355 nm wavelength, shifted by λ . The Glan-Taylor prism acts as a polarization filter, passing only linear polarized light vertically into the atmosphere through an opening in the protection window, with an additional window under the Brewster's angle. The perpendicular polarization is absorbed in the tube.

The receiving system consists of the appropriate optics for collecting and separating the signals of 355 nm and 532 nm wavelength, the latter both parallel and perpendicular polarized, and photomultiplier tubes. The signal is guided through a broadband antireflection coated window (BK7) which, in zenith configuration, protects the optics from pollution and water droplets. The light is collected by an off-axis parabolic mirror (SORL, USA) with a focal length of 48 cm. Two folding mirrors are applied, the first guiding the signal to the pinhole of 1.5 mm diameter, resulting in a field of view of the telescope of 3.1 mrad. An anti reflection coated achromatic lens in the detector block (VM-TIM, Germany), designed for 532 nm and 355 nm, is used to parallelize the beam. It is then splitted into the different wavelengths by a 45° dichroic mirror (Laseroptik Garbsen, Germany). The 355 nm signal passes straight on through an interference filter with a bandwidth (full width half maximum, FWHM) of 1nm (Barr, USA) and is then focused with an anti reflection coated lens (Melles Griot) on a photomultiplier tube (PMT, R7400-03, Hamamatsu, Japan). The 532 nm signal is reflected at the dichroic mirror. A polarizing beam splitter then separates the parallel and the perpendicular polarized signal. The parallel signal goes through an interference filter with 0.15 nm bandwidth (Andover Corp., USA), is focused by an anti reflection coated lens (Melles Griot) and detected with a Hamamatsu photomultiplier tube.

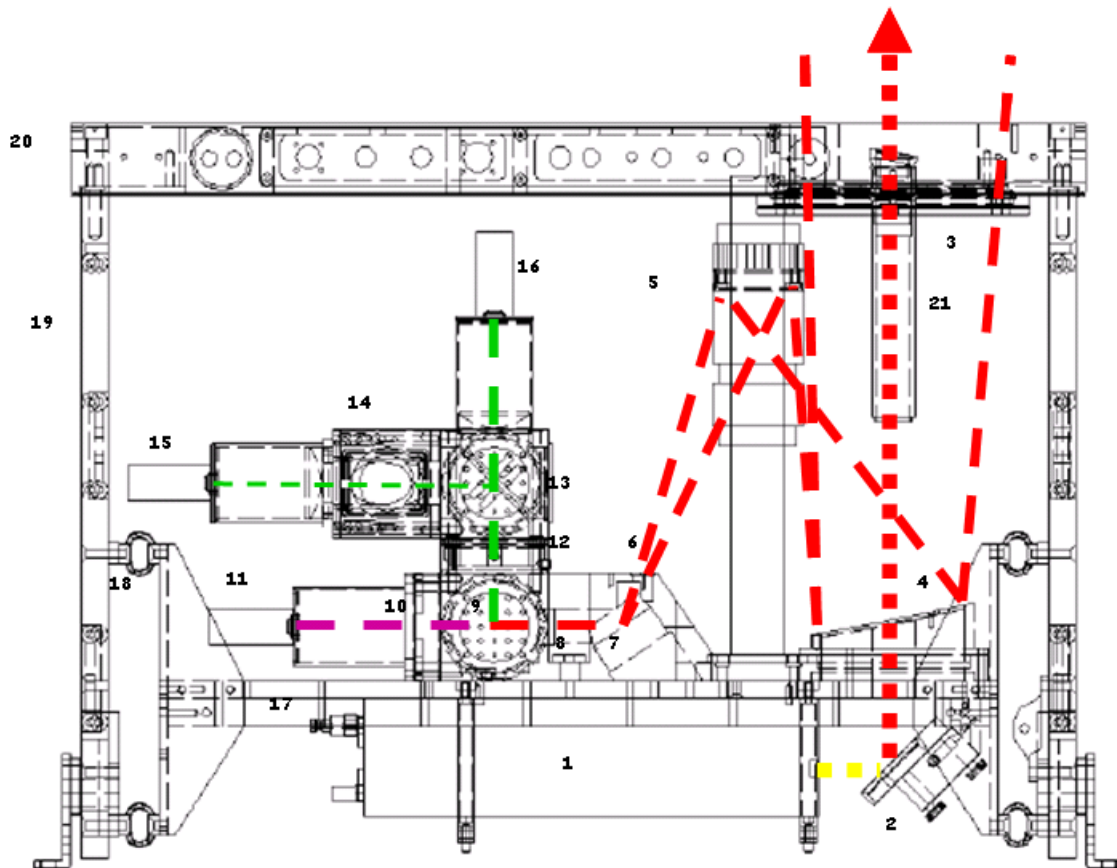


Figure 4.1: The construction of the optical unit. The single components are: Nd:YAG laser (1), mirror (2), window with Brewster's angle (3), off-axis parabolic mirror (4), first folding mirror (5), pinhole (6), second folding mirror (7), achromatic lens (8), beam splitter (9), interference filter for 355 nm channel (10), PMT 355 nm detection (11), interference filter for 532 nm channel (12), polarising cube (13), thin film polarising filter (14), PMT for detection of 532 nm perpendicular polarized (15), PMT for detection of 532 nm parallel polarized (16), optical bench (17), springs (18), posts (19), base plate (20), tube including waveplate and Glan-Taylor polarizer (21).

Superimposed is the optical path in the AMALi system. The laser light composed of the three wavelengths 1064 nm, 532 nm and 355 nm (yellow line) is sent into the atmosphere by a mirror transmitting the 1064 nm and highly reflecting the 532 nm and the 355 nm (red line). The backscattered light is collected by the telescope and split up into the 355 nm (purple line) and 532 nm (green line) by a dichroid mirror. Finally the 532 nm is split up into the components parallel (thick green line) and perpendicular (thin green line) to the emitted polarization direction.

The perpendicular signal is filtered for cross-talk using a thin film polarizing filter at the Brewster angle of 56° and is also focused on a Hamamatsu photomultiplier. To avoid saturation of the detectors from the strong backscatter signal in the nearest range, the light intensity and the dynamical range were reduced by the implementation of neutral density filters of various optical thicknesses right in front of the 532 nm parallel and 355 nm detectors. In order not to reduce the far range signal too much, the optical depth of these filters were chosen carefully. Before the 355 nm detector, a filter with optical depth of 0.8 was used while before the 532 nm parallel channel, a filter with the optical depth of 1.0 was employed. In the case that the detectors were saturated due to a strong signal from near the lidar system, they did not recover quickly enough to obtain reliable data from farther ranges.

The system was designed to have full overlap between telescope field of view and laser beam at the closest possible distance. The signal can only be evaluated from the point where there is full overlap, which is determined by the geometry of the detection unit. With the geometry indicated above, the complete overlap of the backscattered laser beam and the field of view of the telescope is reached at a distance to the aircraft of 235 m (Stachlewska, 2006).

4.1.2 Controller

The controlling unit "Integrated Cooler and Electronics" (ICE) supplies the laser head with cooling liquid, power and controlling parameters. Switches for turning on the pump of the cooling liquid, the flashlamp, and the Q-switch are integrated. Further, the laser power can be adjusted by changing the intensity of the flashlamp. The frequency can be chosen, which is normally set to 15 Hz.

The cooling system is included in the ICE housing. An ethylene glycol – water 1:1 solution is used for cooling, to avoid freezing liquid for airborne operations and in the polar regions. The controlling unit has a temperature and a flow interlock, switching off the laser in case of error messages. For security reasons on board of the aircraft the cooling liquid is pumped to and from the laser head in a double-ply hose with non flammable outer layer.

The long-term stability of the laser was found to be best at an intensity a bit smaller than maximum (Stachlewska, 2006). During a typical measurement period of 3 hours, a warming-up effect of half an hour is observed in the data. However, as the data evaluation does not rely on constant absolute values of the laser power, the lidar data can be used from the beginning of the laser activity. The operator starts the flashlamp and operates the Q-Switch at the ICE manually, in addition to the controlling done in the data acquisition software.

4.1.3 Transient recorders

The transient recorders developed by Licel (Germany) are used for reading out and pre-processing the signals of the three photomultipliers and sending them to the data acquisition program on the laptop.

The challenge of measuring lidar signals in the troposphere is the large dynamic range. The longest possible range can be obtained when the signal strength is just below saturation at the beginning of the full overlap between laser beam and telescope field of view. To measure these signals, quick and reliable electronics are needed. The signals of the three detectors are read out both in analogue and photon counting mode. The photon counting signals are saturated for a range below 1.5 km, the analogue signals get too low for evaluation at a range of 3 km. In the data evaluation, the two signals are composed, overlapping between 1.5 km and 3 km.

A signal from the laser flashlamp is used as source to trigger the transient recorders (Fig. 4.2), which start reading out the photo current and photon counts of the three photomultipliers at a frequency of $\nu = 20$ MHz. According to the equation

$$c = 2s \cdot \nu, \quad (4.1)$$

with c being the speed of light and s the height interval from where the backscattered light is collected, the frequency for reading out the signals corresponds to a sampling interval s of 7.5 m.

The Q-switch is also triggered by the flashlamp signal after the optimal time delay determined by the laser. The transient recorder controls the delay time between the firing of the flashlamp and the laser (set to 135 μ s). Timings are derived from a quartz based oscillator ensuring nanosecond timing stability. As there is no reference value for calibrating the lidar signal in the far end for nadir configuration, a pretrigger is used to determine the background. This means that the photomultipliers start collecting data before a laser pulse is fired, and the mean signal measured during this time is assumed to represent the background stray light getting into the detectors without laser activity. The delay times between the pretrigger and the Q-Switch and between the lamp pulse and the pretrigger can be varied, just the sum is kept constant.

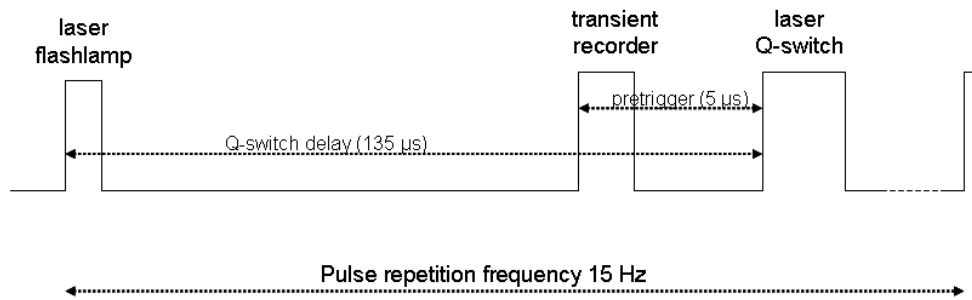


Figure 4.2: Timings of laser activity and data acquisition. The pretrigger delay is set to 5 μs for zenith and to 20 μs for nadir operations. Scheme adapted from Stachlewska (2006).

The number of available bins in each transient recorder (1700) determines the maximum recording range ($1700 * 7.5 * 2 \text{ m}$). The effective maximum range is reduced by the number of bins used for the background determination between pretrigger and laser trigger timings. All bins can be read out and transferred to the computer for each laser shot. For nadir configuration, the delay between pretrigger and Q-Switch was set to quite a long period of 20 μs , corresponding to 400 bins or a height of 3000 m. For the zenith aiming configuration, a shorter pretrigger of 5 μs was chosen to have more information about the signal coming back from higher altitudes. In this case, only 100 out of the 1700 bins were used for the determination of the background.

In the normal operation mode, 14 single shots of data profiles obtained by the photomultipliers are added within the transient recorder and sent via ethernet cable to the laptop. The typical data transfer rate is 150 kb s^{-1} . There the profiles are stored in files and shown on the real-time display for immediate check of the state of the atmosphere.

The transient recorders are working in a data transfer mode called the push mode. This means that the transient recorders get their start, stop, and readout commands from the ethernet controller without any direct interaction with the computer. The ethernet controller then pushes the data to the computer. At the computer level, a periodic task reads the data when it becomes available from the TCP/IP buffer. This frees the laptop from controlling the transient recorders and reduces the communication load, which is important for single shot acquisition (Licel Transient Manual, http://licel.com/transient_overview.html).

4.1.4 Software

A dedicated electronics and a laptop with custom-designed LabVIEW software developed by Licel, Germany, control the laser pulses and collect the data. There are two configurations of software corresponding to the two different mechanical configurations (nadir and zenith) of the lidar system with different default values for the pretrigger length and the online display. With the controlling software, the operator can choose the high voltage of the photomultipliers, the pretrigger length, enable the Q-switch before manually turning on laser firing at the laser controller, and start the data acquisition.

The first online glance on the data is permitted by a panel showing on a logarithmic scale the raw data profiles for all six channels (three analogue and three photon counting) updated every second (Fig. 4.3, top). The representation of each profile can be switched on and off separately in order to have an overview of the performance of all signals or to concentrate on the channel of interest. Three displays for background and range corrected time series can represent optionally any of the six signals or ratios of the signals. According to the structures of interest, this may be the analogue or photon counting signals, the depolarization ratio or the

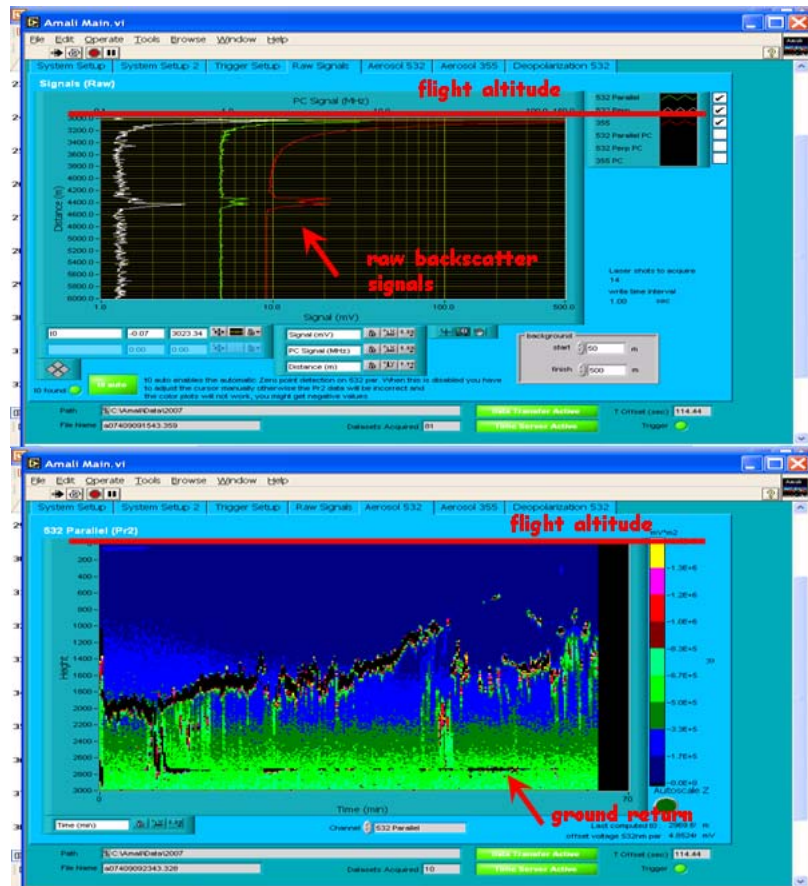


Figure 4.3, top: Real-time logarithmic display of lidar backscatter profiles. Bottom: Online display of the time series of the range-corrected lidar profiles. Boundary layer cloud structures and the ground return are visible.

color ratio (see Chapt. 3). The color coded pictures are updated every minute and give an impression on how the atmosphere is changing with time and location of the lidar system. An examples of the quick-look display is represented in Fig. 4.3 (bottom). The picture shows nadir measurements of precipitating mixed-phase clouds (Chapt. 7).

4.2 AMALi in the Polar-2 aircraft

There are two possibilities for integrating the AMALi in the aircraft, the nadir and zenith looking configuration. The choice of the configuration depends on the flight altitude and the atmospheric structures of interest. Additionally, the two configurations make it possible to compare the airborne measurements with ground-based and space borne lidar systems. The two operation modes of the AMALi required some modifications of the fixing in the aircraft and in the construction of the optical unit itself. Changing the configuration requires about 1 h. In both cases the optical unit is installed at the floor of the aircraft.

In the nadir configuration the optical unit is placed on the right hand side of the aircraft above a perforation of 15 cm diameter in the floor (Fig. 4.4, right). In the zenith configuration the optical unit is placed upside down diagonally on the left hand side of the airplane, the open hole in the roof being located directly behind the cockpit (Fig. 4.4, left). For protecting the operators on board of the aircraft from the laser radiation in the zenith configuration, the path of the laser pulses is covered with a light steel tube of 15 cm diameter leading from the optics unit to the aircraft's roof with the open hole. The tube is fixed to the roof and the optical assembly via two flexible convoluted bellows of non-flammable aramid kevlar tissue.

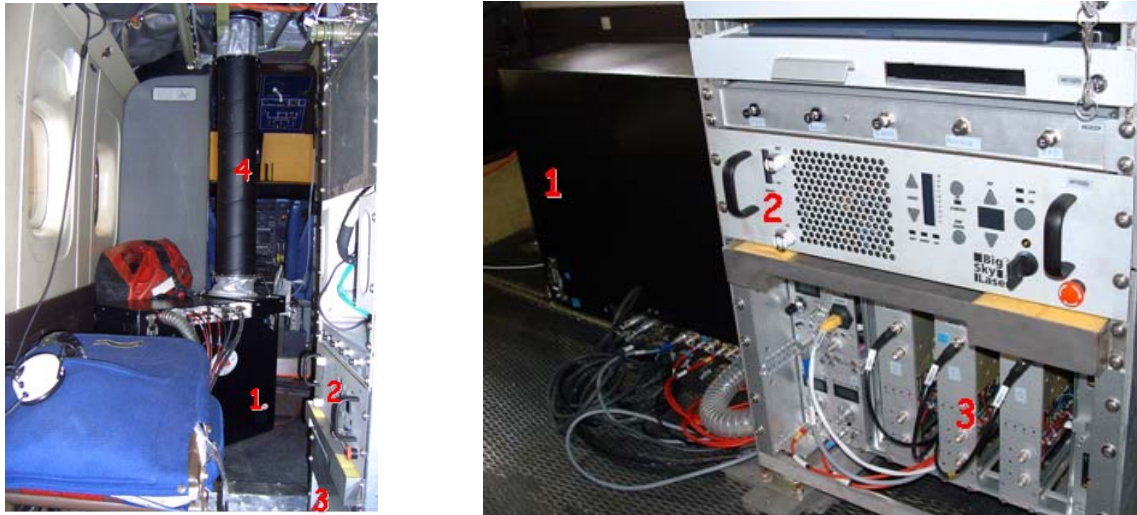


Figure 4.4, left: The AMALi in zenith looking configuration in the Polar-2 aircraft. The optical unit (1) is fixed upside down on the floor, right under the open hole in the roof. The laser controller (2) and the transient recorders (3) are integrated in a rack. The protection tube (4) is shielding the laser beam.

Right: The AMALi in nadir-looking configuration in the Polar-2 aircraft. The optical unit (1) is fixed on the floor, above the open hole. The laser controller (2) and the transient recorders (3) are integrated in a rack.

Before operating the AMALi system, the flashlamp has to warm up for 10 minutes. In nadir configuration, the system can be switched on soon after takeoff, and the flashlamp is warming up during the ascent to the final flight altitude (usually 3000 m). In zenith configuration, the system can be switched on and the flashlamp can warm up before takeoff, the laser and the lidar data acquisition can already be started before takeoff.

4.3 Data evaluation

The evaluation routine used here is based on MATLAB programs developed by Stachlewska (2006). The programs were further modified and extended as described below. Single scattering is assumed for routine evaluation.

The raw data of the three detection channels in analogue and photon counting mode are first background corrected. For each profile, the average background value determined during the pretrigger period is calculated and subtracted from the raw data profiles. In some cases, spikes caused by electronic noise were found in the 532 nm perpendicular polarization signal, which were removed manually before subtracting the mean background value. Then the pretrigger bins are cut, leaving only the real lidar signal, which is first increasing with range until the overlap of telescope and laser beam is reached and then basically decreasing with r^{-2} .

The signal is then averaged over a certain integration time, ranging typically from 15 s to 5 min depending on the application. Generally, the criterion for minimum integration time was set to a signal to noise ratio exceeding 15 at the altitude of the structures being examined.

The data profiles of the analogue and photon counting channels are compared and composed at a height interval where the photon counting channel is not saturated any more and the signal of the analogue channel is still high enough above the noise level. For this purpose, the curvature of both signals is compared in the range between 1.5 km and 3 km. The best agreement over some 100 m is used for composing gradually the combined analogue and photon counting signal. For the short range, the analogue signal multiplied by a scaling factor is used, for the far range, only the photon counting signal is considered. According to Chapt. 3, the multiplication with a constant does not change the solution of the lidar equation.

For a first check of the lidar data quality and the scattering components in the air, the composed signal is range corrected by multiplication with the factor of r^2 . The scattering particles can be considered as a point source of radiation, and the intensity of the backscattered light decreases with the distance of the scatterer as r^{-2} . The dependence on air density is also eliminated by dividing the range corrected signal by the air density profile obtained from the temporally closest radio sounding in Ny-Ålesund. Thereby the molecular (Rayleigh) contribution of backscattering, which for the considered wavelengths is approximately as strong as the backscattering of thin clouds, is removed from the lidar signal. For routine calculation of the backscatter and extinction coefficient, the standard Klett algorithm is applied (see Chapt. 3) after smoothing the vertical profiles with a running mean. A lidar ratio of 20 was assumed for the evaluation of clouds (Lampert et al., 2009a), and a higher value of 30-40 (Hoffmann et al., 2009) was used for the evaluation of aerosol profiles as a first approximation. The boundary condition at the far end from the lidar system was chosen depending on the atmospheric structures. For zenith measurements under clear conditions, a small BSR slightly above the molecular value of 1 was set at the tropopause level. For nadir observations under clear conditions, the value for the BSR near ground was varied iteratively until the values below the aircraft in the free troposphere had values slightly exceeding 1. For optically thin cloud measurements, the boundary conditions were set as described above. However, in the case of optically thick clouds, the boundary condition was set within the cloud and varied to obtain realistic values of backscatter near the aircraft. The data of the clouds themselves could not be evaluated quantitatively due to multiple scattering. In the case of spatially inhomogeneous cloud systems, the boundary value of backscatter and the reference height were checked and adapted manually for each averaged lidar profile to best match the backscattering values in the clear free troposphere.

For calculating the depolarization, the signal of the detector measuring the perpendicular polarized light, composed of analogue and photon counting profile, is divided by the signal of the same wavelength with the polarization direction not altered. As described in Chapt. 3, the depolarization is normalized by setting it equal to the known molecular depolarization (0.36 % for the AMALi system), which depends mainly on the bandwidth of the filters, in a height interval with presumably clear air.

5 The Arctic Study of Tropospheric Aerosol, Clouds and Radiation (ASTAR) 2007

The third Arctic Study of Tropospheric Aerosol, Clouds and Radiation (ASTAR 2007) was conducted in Svalbard from 26 March 2007 to 18 April 2007 as part of the activities of the International Polar Year. With an instrumentation similar to the predecessor campaigns ASTAR 2000 (Hara et al., 2003, Treffeisen et al., 2005, Yamanouchi et al., 2005) and ASTAR 2004 (Gayet et al., 2007, Engvall et al., 2008), the ASTAR 2007 campaign had the primary objective to investigate Arctic aerosol, clouds and the interaction with radiation in the troposphere. Spring time was chosen as it constitutes the season with frequent occurrence of Arctic haze, formed by polluted air masses which are transported into the Arctic from lower latitudes (Quinn et al., 2007). Another aspect was to contribute to the validation of the satellite sensors onboard CALIPSO and CloudSat in the polar regions. Further objectives were to identify transport pathways of particulate and gas phase pollutants in and out of the Arctic from the boundary layer to the upper troposphere, to study chemical processes and transformation of aerosol properties in ageing polar air masses, and to study the effect of cirrus clouds on halogen chemistry in the Arctic upper troposphere.

In the intense observation period of three weeks, the vertical distribution of microphysical, optical and chemical properties of Arctic aerosol and clouds were investigated based on synoptic and pollution forecasts. The different ground-based, airborne and satellite borne measurements served to analyze the complex Arctic processes and interactions. With the help of year-round observatory and satellite measurements, the investigations of the local spring-time campaign can be extended to cover much larger regions and different seasons, which is especially important for modeling activities.

5.1 Participants, organization, operations

The ASTAR 2007 was an international campaign with scientific participants from the following institutes: the Alfred Wegener Institute for Polar and Marine Research (AWI), Bremerhaven and Potsdam (Germany), the Institute of Atmospheric Physics, DLR, Oberpfaffenhofen (Germany), the Department of Meteorology at Stockholm University ITM / MISU, Stockholm (Sweden), the Max Planck Institute for Nuclear Physics, Heidelberg (Germany), the Institute for Environmental Physics (IUP), Heidelberg (Germany), the Institute for Atmospheric Physics, Johannes Gutenberg University, Mainz (Germany), the Laboratoire de Météorologie Physique (LaMP) / Université Blaise Pascal, Clermont-Ferrand (France), the Norwegian Institute for Air Research (NILU), Kjeller (Norway), the Finnish Meteorological Institute (Finland), the Institute of Oceanology, Polish Academy of Science, Sopot (Poland), the NASA Langley Research Center (USA), the Institute of Atmospheric Sciences and Climate (ISAC), Bologna (Italy) and Leosphere Lidar Environmental Observations, Paris (France). Responsible for the airborne operations were the Flight Facility DLR, Braunschweig and Oberpfaffenhofen (Germany) and OPTIMARE Sensorsysteme, Bremerhaven (Germany).

The main focus during ASTAR 2007 were airborne measurements from Longyearbyen airport, Svalbard, with two research aircraft, the AWI Polar-2 Dornier 228-101 and the DLR Falcon. The aircraft had an endurance of about 3.5 h and 4 h, respectively.

Flight planning was based on a detailed weather and pollution event forecasts (Sect. 5.5 and 5.6). For flight planning, the latest development of the expected cloud and aerosol distribution was reviewed every morning. Satellite tracks were also included in the forecast.

Table 5.1: Instrumentation onboard of the Polar-2

ASTAR 2007 / Polar 2 payload

Category	Instrument	Method	Measurement	Institute	PI
Aerosol extinction, radiance & irradiance	Sun photometer	Sun photometer	Spectral aerosol extinction coefficient	AWI Bremerhaven	Herber
	Spectral albedometer	Spectral albedometer	Spectral Radiance (up and downward)	IfT Leipzig	Wendisch
	Radiation sensor	Up- and downward radiation sensor	Spectral selected radiation (downward) and up- and downward radiation	AWI Bremerhaven	Birnbaum
Vertical aerosol profile	AMALI	Aerosol Mobile Airborne Lidar (upward or downward looking)	Backscatter ratio and extinction coefficient at 532 nm	AWI Potsdam	Neuber
Cloud microphysics	FSSP-300 2D-C	Particle spectrometer & imaging probes	cloud element size distribution, particle shape	LaMP	Gayet
	CPI	Cloud particle imager	cloud element size distribution, particle morphology	LaMP	Schwarzenböck
	PN	Polar nephelometer	Scattering phase function	LaMP	Gayet
Aircraft data	Aircraft position data	Polar 2 basic sensor instrumentation	Aircraft position data	Optimare	Garbrecht
	Atmospheric state	Polar 2 basic sensor instrumentation	Pressure, temperature, wind	Optimare	Garbrecht
	CR-2	Frost point hygrometer	humidity	AWI/NIPR	Herber / Wada

Depending on a variety of different scientific objectives, the aircraft were directed into areas with or without clouds, above open water or sea ice, for validation along satellite tracks or above ground-based stations.

The weather forecast was based on the deterministic ECMWF (T799/L91) model. The following parameters were prepared up to 156 hours ahead in time:

- sea level pressure
- low level clouds (> 800 hPa)
- medium level clouds (800 - 400 hPa)
- high level clouds (< 400 hPa)
- cloud condensate, liquid and ice water content at different pressure levels
- relative humidity at different pressure levels
- temperature at different pressure levels
- geopotential at different pressure levels
- wind at different pressure levels
- vertical cross sections (North-South, East-West or along the planned flight track)

Furthermore, AVHRR satellite images were consulted for final go / no-go decisions.

The pollution forecast relied on various tools: For every day, a European and a North American CO and SO₂ tracer were calculated by FLEXPART forecasts (Stohl et al., 2005) as a way to predict the possible advection of human caused pollution from lower latitudes (Arctic haze) to the surroundings of Svalbard. FLEXPART is based on a particle trajectory model operated in a forward mode which allows for information on air mass and tracer transport. Because large events of enhanced Arctic aerosol can be caused by biomass burning events like in 2006 (Stohl et al., 2007, Treffeisen et al., 2007), additionally a biomass burning CO tracer was calculated. HYSPLIT (Hybrid Single-Particle Lagrangian Integrated Trajectory, <http://www.arl.noaa.gov/HYSPLIT.php>) backward trajectories of different heights ending in Longyearbyen, Svalbard, were analysed for air transport during the past 8 days, as this is the typical mean lifetime of Arctic aerosol (Sirois and Barrie, 1999). The Navy Aerosol Analysis and Prediction System (NAAPS) aerosol classification was also taken into account.

Table 5.2: Instrumentation onboard of the Falcon

ASTAR 2007 / Falcon Payload (final status)

Category	Instrument	Method	Measurement	Institute	PI
Aerosol	CPSA/CPC system	6-channel condensation particle counter system (unheated/heated)	Nucleation and Aitken mode aerosol number concentration, semi-/non-volatile particle fraction	DLR-IPA	Minikin
	PCASP-100X FSSP-300	Aerosol spectrometer probes	accumulation and coarse mode particle size distribution, cloud elements	DLR-IPA	Minikin
	Grimm OPC	Optical particle counter	accumulation mode particle size distribution	MISU/ITM Stockholm	Krejci
	(Tandem-) DMA	Differential mobility analyzer (unheated/heated), volatility tandem mode (optional)	Aitken & accumulation mode particle size distribution, aerosol mixing state	MISU/ITM Stockholm	Krejci
	PSAP	Particle soot absorption photometer	Aerosol absorption coefficient	MISU/ITM Stockholm	Krejci
	3A PSAP	3-wavelength Particle soot absorption photometer	Aerosol absorption coefficient	FMI & DLR-IPA	Virkkula (Minikin)
	IN	Integrating nephelometer (Radiance Res.)	Aerosol scattering coefficient	NIPR	(Krejci / Minikin)
	Aerosol sampling	Filter/impactor sampling for single particle element analysis	Aerosol chemistry	TU Darmstadt	Worringen (Minikin)
Trace gases	NO/NO _y & j(NO ₂)	Chemi-luminescence & AU converter, filter radiometer	NO & NO _y mixing ratios, calculation of NO ₂	DLR-IPA	Schlager
	CO	VUV fluorescence	Carbon monoxide mixing ratio	DLR-IPA	Schlager
	Ozone	UV absorption	Ozone mixing ratio	DLR-IPA	Schlager
	IT-CIMS	Chemical ionization mass spectrometry	SO ₂ mixing ratio, also HNO ₃ and HCl possible	MPL-K & DLR-IPA	Arnold / Schlager
	CR-2	Frost point hygrometer	humidity	DLR-IPA	Busen (Minikin)
	Mini-DOAS	Differential absorption spectrometry	Halogen compounds	Uni Heidelberg	Prados & Simmes
Aircraft data	Aircraft position data	Falcon basic sensor instrumentation	Aircraft position data	DLR-FB	Dreiling
	Atmospheric state	Falcon basic sensor instrumentation	Pressure, temperature, humidity, wind	DLR-FB	Dreiling

Various ground-based stations in Svalbard supported the program: The French-German AWIPEV research station located at the Kongsfjord in Ny-Ålesund (78.9° N 11.9° E), the Norwegian clean air laboratory of Zeppelin Station at 470 m altitude near Ny-Ålesund, and the Polish Polar Station Hornsund (77.0° N 15.6° E).

The AWIPEV station contributed to the campaign with daily profiles of radio or ozone sounding, standard meteorological measurements, sun photometer data and lidar observations. The full-automatic multichannel sun photometer (SP1A) measures spectral aerosol optical depth for the wavelength range of 351 to 1062 nm (Herber et al., 2002). The Koldewey Aerosol Raman Lidar (KARL) provides profiles of backscatter and extinction coefficient for the wavelengths 1064 nm, 532 nm and 355 nm, as well as depolarization profiles for 532 nm (Ritter et al., 2004). Raman channels (molecular nitrogen Raman shifted lines at 387 nm and 607 nm, water vapor lines at 407 nm and 660 nm) allow the retrieval of air density and water vapor. Further, the micro pulse lidar (MPL, Spinhirne, 1993) provided data of backscatter profiles at a wavelength of 523.5 nm on a 24-hour basis. Data losses usually only occur when the window is covered with snow, which is removed manually. The MPL in Ny-Ålesund is operated by the Japanese National Institute of Polar Research (NIPR) and maintained by the base personnel of the AWIPEV station.

The Zeppelin Station is equipped by MISU / ITM with different instruments to characterize aerosol properties, namely a Differential Mobility Particle Sizer, Condensation Particle Counters, Optical Particle Counters, a Particle Soot Absorption Photometer and a Volatility Differential Mobility Particle Sizer (Ström et al., 2003).

The Hornsund Station provided measurements of spectral aerosol optical thickness (sun photometer), aerosol concentration and size distributions, solar radiation fluxes, upward and downward shortwave and longwave radiative fluxes, and total ozone content.

In Longyearbyen, additional measurements were performed with the portable lidar system of Leosphere, which provided backscatter profiles at a wavelength of 355 nm. Some Controlled Meteorological Balloons (CMET) were launched by NILU. They were supposed to travel for

several days with the air flow. The aim was to return to the location of the balloon in order to study the ageing of the aerosol within the same air masses using the instrumentation of the Falcon aircraft.

An overview of the different groups participating on board of the two research aircraft in the ASTAR 2007 campaign with their measurement techniques are listed in Table 5.1 (Polar-2) and Table 5.2 (Falcon).

The Falcon payload consisted of instruments for studying aerosol properties and trace gases. The aerosol instrumentation included different particle counters, optical aerosol spectrometer probes, a mobility and volatility analyzer for particle size distributions, particle soot absorption photometers, an integrating nephelometer for particle backscatter and extinction, and a filter and impactor sampling system for investigating chemical properties. The trace gas instrumentation was designed to measure the mixing ratios of NO, NO_y, CO, O₃, and SO₂. A mini-DOAS (Differential Optical Absorption Spectroscopy) was used for observing halogen compounds.

Onboard of the Polar-2 aircraft, the following instruments were integrated: The Airborne Mobile Aerosol Lidar of the AWI (Chapt. 4), the in situ instruments Polar Nephelometer, Cloud Particle Imager and Forward Scattering Spectrometer Probe, operated by the LaMP (Sect. 5.3) for characterizing the optical and microphysical properties of cloud particles, the Spectral Modular Airborne Radiation measurement sysTem (SMART-Albedometer) of the University of Mainz to characterize the radiative effect and the albedo of clouds (Sect. 5.3). Furthermore, a multichannel photometer of the AWI was on board to determine the aerosol optical depth. For first testing and validation, there was also a spectroradiometer of the AWI. Aircraft flight tracks were, if possible, coordinated with satellite overpasses in order to obtain additional data and to contribute to the satellite validation at high latitudes. The lidar CALIOP (Winker et al., 2007) on board of the satellite CALIPSO provides atmospheric backscatter and depolarization profiles at the same wavelength as the AMALi (532 nm, parallel and perpendicular polarization), and at the wavelength of 1064 nm. As the lidar is an active remote sensing instrument, CALIOP data are to a high degree independent of day- and nighttime conditions (Vaughan et al., 2004, McGill et al., 2007). In contrast to passive satellite sensors based on the measurements of scattered or emitted solar and thermal infrared radiation, CALIOP is capable to observe even optically thin clouds more clearly. The data were used for estimating the occurrence of optically thin midlevel clouds during the ASTAR campaign (Sect. 6.4). CALIOP and CloudSat radar profiles (Stephens et al., 2002) were further compared to the airborne cloud observations (Sect. 7.2.3, and Gayet et al., 2009). While lidar is mainly sensitive to the comparatively small liquid water droplets, radar detects with high accuracy ice crystals. The combined evaluation of the two space borne instruments provides very useful for the investigation of mixed-phase clouds (Gayet et al., 2009). Further, Moderate Resolution Imaging Spectroradiometer (MODIS) pictures obtained by the satellites Terra and Aqua served as an overview of the cloud scene in the flight area (e.g. Ehrlich et al., 2008). Combined satellite borne, airborne and ground-based measurements, especially when performed on a larger scale, are of primary importance for modeling activities.

5.2 AMALi in the ASTAR campaign

The application of the AMALi had various objectives: With its real-time display of backscatter and depolarization data, the instrument served as pathfinder to indicate atmospheric structures of interest, which could then be probed consecutively with the in situ devices of Polar-2 or Falcon. Moreover, it was used for calibration and validation purposes in combination with other lidar systems.

Table 5.3: Overview of the 14 lidar flights during ASTAR 2007. Indicated in red are the case studies analyzed in the thesis.

Date	mode	aim of flight	flight direction	Atmospheric features	CALIPSO	Special events
31/03/2007	zenith	test	W, Isfjorden	some low level clouds	no	longer than planned
01/04/2007	zenith	clear sky, CALIPSO	E, above land	Cu below aircraft	yes	delayed flight
02/04/2007	zenith	clear sky, CALIPSO	W, above ocean	low clouds below flight level	yes, 10:00	
03/04/2007	nadir	clouds, KARL	W, Ny-Ålesund	low level clouds above ocean	no	
07/04/2007	nadir	clear sky	SE, sea ice edge	single Cu	no	IP problems
08/04/2007	nadir	clouds, KARL	W	thick Cu	no	low signals
08/04/2007	nadir	clear sky	SE	few low level clouds	no	
09/04/2007	nadir	clouds, CALIPSO	W	thin low level clouds, precipitation	yes	in situ during overpass
10/04/2007	zenith	cirrus, Falcon	SE	subvisible midlevel cloud	no	polar bear
11/04/2007	zenith	clear sky CALIPSO	W, Ny-Ålesund	cirrus	yes, 09:53	landing gear problems
12/04/2007	zenith	clouds	W, Isfjorden	cirrus 4-7 km	no	
14/04/2007	zenith	cirrus, Falcon	W, above ocean	low & midlevel clouds	no	
14/04/2007	zenith	midlevel clouds	W, above ocean	low & midlevel clouds	no	
16/04/2007	nadir	KARL	Ny-Ålesund	low level clouds / cloud free	no	

These systems were the ground-based lidar KARL at Ny-Ålesund, the backscatter lidar provided by Leosphere at Longyearbyen, and the satellite borne lidar on board of CALIPSO. Finally the AMALi was used for investigating liquid, mixed-phase and ice clouds. The original aim of characterizing Arctic haze aerosol was not worth pursuing due to the only very low background values throughout the campaign (Sect. 5.6). Table 5.3 gives an overview of the 14 Polar-2 flights with lidar operation during the ASTAR campaign. During six of these flights, the AMALi was nadir pointing to characterize the lowest part of the atmosphere (0-2.7 km, depending on the flight altitude of the Polar-2), to detect clouds and aerosol in the boundary layer and for validation with the ground-based and zenith looking KARL lidar in Ny-Ålesund and the Leosphere lidar in Longyearbyen. On eight flights, the lidar was zenith pointing to detect midlevel and high level clouds and pollution, and to validate the satellite borne nadir aiming CALIOP lidar system. Four flights were dedicated to the validation of the CALIOP lidar system. During six flights, combined measurements of the lidar and the cloud microphysics instruments were performed. In these cases, the typical flight pattern consisted of a long leg flying at constant altitude above or below a cloud system for observations with the remote sensing configuration (lidar and albedometer), and consecutively a sequence of descent / ascent profiles within the clouds employing the in situ instruments.

In total, about 22 flight hours of lidar data were obtained during the ASTAR 2007 campaign. The data quality allowed the standard calculations with an integration time of 15 s. Only during the first flight on 8 April 2007, the lidar signal was too weak for a proper evaluation due to the low temperatures. The first three clear sky flights in zenith configuration exhibited no significant atmospheric features. The results of the thesis are based on four case studies of cloud observations, performed on 8, 9, 10 and 14 April 2007.

5.3 Instrumentation on board of the Polar-2

The instruments on board of Polar-2 aircraft that were used for the cloud investigations of the thesis in addition to the AMALi are described in the following. They include standard meteorological instruments, the in situ instruments Polar Nephelometer (Gayet et al., 1997), Cloud Particle Imager (Lawson et al., 1998), and Forward Scattering Spectrometer Probe (Dye and Baumgardner, 1984, Gayet et al., 2007), as well as the SMART-Albedometer (Wendisch et al., 2001, Bierwirth et al., 2009).

Standard meteorological instruments in the aircraft measured pressure, temperature, and relative humidity. The air temperature was observed with a Rosemount-PT100 sensor and corrected for the dynamic heating effect. The relative humidity related to water saturation was recorded by a Vaisala HMT333 detector. Additionally, pyrgeometer measurements of upwelling and downwelling thermal infrared irradiance were performed with Eppley instruments. However, the pyrgeometer could not be adjusted perfectly due to space limitations (inclination of around 5°) and was not temperature stabilized.

The combination of the three independent in situ techniques provides a description of particles within a diameter range varying from a few micrometers (typically 3 μm) to several millimeters at a frequency of typically 10 Hz.

The **Polar Nephelometer** (PN) measures the scattering phase function of an ensemble of cloud particles (from a few micrometers to about 800 μm diameter), which intersect a collimated laser beam near the focal point of a parabolic mirror. The light scattered at angles from about 3.5° to 173° is reflected onto a circular array of 56 near-uniformly positioned photodiodes. The laser beam is provided by a high-power (0.8 W) multimode laser diode operating at a wavelength of 804 nm. The data acquisition system is designed to provide a continuous sampling volume by integrating the measured signals of each of the detectors over

a manually-defined period. Methods have been developed to infer the particle phase (liquid or ice), optical parameters (asymmetry parameter, defined as

$$g = \langle \cos \theta \rangle = \frac{1}{2} \int_{-1}^1 \cos \theta \cdot P(\cos \theta) \cdot d \cos \theta \quad (5.1)$$

with θ being the scattering angle and P the phase function, volume extinction coefficient, extrapolated phase function at 532 nm, and lidar ratio), and microphysical properties (particle size distribution, liquid water content (LWC), ice water content (IWC), and particle number concentration). For spherical water droplets the asymmetry parameter is about 0.85, while for ice crystals, g is smaller than 0.85. An iterative inversion method developed by Oshschepkov et al. (2000) and upgraded by Jourdan et al. (2003a), using physical modeling of the scattered radiation, is applied to the average angular scattering coefficients (ASC) measured by the PN. The inversion method is described in more detail in Chapt. 6. Different microphysical models are tested and the best fit of the measurements is determined. The average errors of the measurements of the angular scattering coefficients lie between 3 % to 5 % for scattering angles ranging from 15° to 155° (with a maximum error of 20 % at 155°, Shcherbakov et al., 2006). The uncertainties of the derived extinction coefficient and asymmetry parameter from PN measurement are estimated to be in the order of 25 % and 5 %, respectively (Gayet et al., 2002). The bulk microphysical (number concentration, IWC, effective diameter) and optical parameters (extinction, extrapolated scattering phase function at 532 nm and lidar ratio) can be assessed following the method presented by Jourdan et al. (2003b). The instrument's detection threshold at an air speed of 60 m s⁻¹ amount to about 0.2 cm⁻³

The **Cloud Particle Imager** (CPI) is an imaging and shadowing probe. It detects small particles and delivers pictures of the non-spherical shape of ice plates. Two continuous-wave laser diodes are used. The intersection of the beams is the sampling volume. When a particle passes, the imaging laser is pulsed, and an image of the particle is stored on the CCD of a digital camera with 1 million pixels and a resolution of 2.3 μm per pixel. By counting the particles, the concentration can be calculated with the knowledge of the sample area and true airspeed of the aircraft.

The **Forward Scattering Spectrometer Probe** (FSSP-100) provides information about the size spectrum (5-95 μm) and number concentrations of cloud droplets. A HeNe multimode laser is focused on the sampling aperture which blocks the laser beam by a central dump spot. If particles cross the laser beam, the scattered light is detected. The intensity on the detector depends on the laser power as well as on the size and shape of the particles and on the index of refraction, which is known for ice and water. For spherical particles, Mie theory is used to derive the probe response. Based on this, the LWC can be calculated with an uncertainty of about 30 %. The particle concentration in the FSSP-100 size range can be calculated with an uncertainty of 20 %.

Generally, the accuracies of measurements on probes with shrouded inlet (Polar Nephelometer, CPI and FSSP) could be hampered by the shattering of ice crystals (Korolev and Isaac, 2005, Heymsfield, 2007, McFarquhar et al., 2007).

The **Spectral Modular Airborne Radiation measurement system** (SMART-Albedometer) measures downwelling spectral radiance and irradiance F_{λ}^{\downarrow} and upwelling nadir radiance I_{λ}^{\uparrow} in the visible (350-1000 nm) and near-infrared range (1000-2100 nm). It is actively horizontally stabilized for airborne applications (Wendisch et al., 2001). A detailed description of the SMART-Albedometer configuration during ASTAR 2007 is presented by Ehrlich et al. (2008). From the measurements, the spectral cloud top reflectivity

$$R_{\lambda} = (\pi \text{ sr}) I_{\lambda}^{\uparrow} / F_{\lambda}^{\downarrow} \quad (5.2)$$

is determined. The spectral slope ice index I_S as introduced by Ehrlich et al. (2008) was analyzed in order to distinguish the cloud phase.

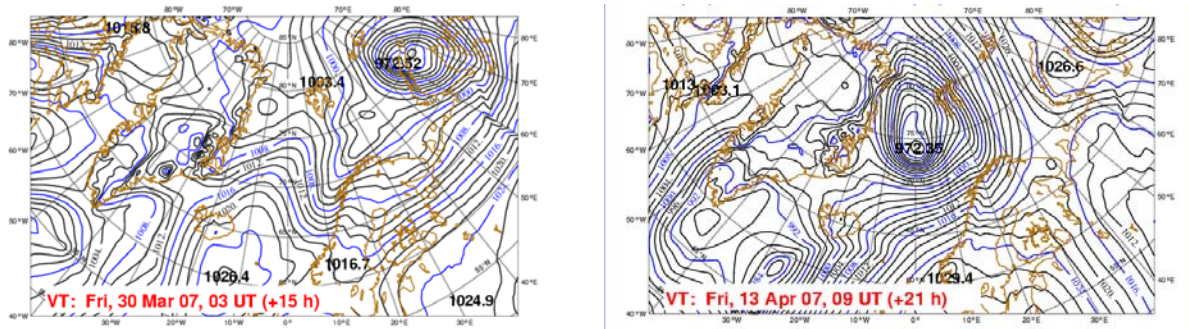


Figure 5.1: ECMWF analyses of MSL pressure (hPa) of 30 March 2007, 03 UTC (+15 h) and 13 April 2007, 09 UTC (+21 h). Provided by Andreas Dörnbrack.

It is defined by

$$I_S = 100 \cdot \frac{\Delta\lambda}{R_{1640nm}} \cdot \left[\frac{dR_\lambda}{d\lambda} \right]_{[1550nm, 1700nm]} \quad (5.3)$$

with $\Delta\lambda = (1700-1550)$ nm. In the wavelength range of 1550-1700 nm used for the analysis, the imaginary part of the refractive index and therefore the absorption of liquid water and ice differ substantially (Sect. 2.3). Values of I_S below 20 are typical for liquid water clouds, while values above 50 indicate pure ice clouds.

The cloud optical depth is estimated from the albedometer measurements. For a given solar zenith angle, the values of the spectral cloud top reflectivity are a function of the particle size distribution and the cloud optical thickness (Nakajma and King, 1990). If the effective particle radius is known (e.g. from in situ observations), the cloud optical depth can be retrieved by radiative transfer calculations. In forward simulations, look up tables for different parameters are created, which serve for comparison with the measurements. The accuracy of the cloud optical depth derived from the uncertainties of the measurements decreases with increasing optical depth. The error is below 20 % for clouds with an optical thickness of less than 20.

5.4 Technical problems

Several problems occurred due to the weather conditions and transport damage of instruments. Construction work at Longyearbyen airport forced the Polar-2 aircraft to spend the night outside a hangar. The low temperatures at the beginning of the campaign (below -20 °C) led to problems with the instruments. Before a flight, the cabin of the aircraft had to be heated up. Due to technical malfunction caused by the low temperatures, the landing gear of the Polar-2 aircraft could not be retracted from 11 April onwards. For security reasons, the landing gear had to be open during the last flights, reducing the flight endurance to 3 h and the operation radius of the aircraft accordingly. The CMET balloons were found to be unsuitable for the cold atmospheric conditions.

The frost point hygrometer and the 2D-C sonde mentioned in Table 5.1 could not be operated as they were broken. Due to technical malfunctions, the data of the spectroradiometer and the sun photometer could not be analyzed. The instruments would have been of interest for a joint data evaluation and further intercomparison with the AMALi.

The protection window of the AMALi was broken during the transport to Svalbard. The AMALi was used without it, paying special attention to cover the optical unit in zenith configuration when there was danger of water droplets. With the open hole of 15 cm diameter in the aircraft fuselage, the optical unit became very cold during the flights, and the laser

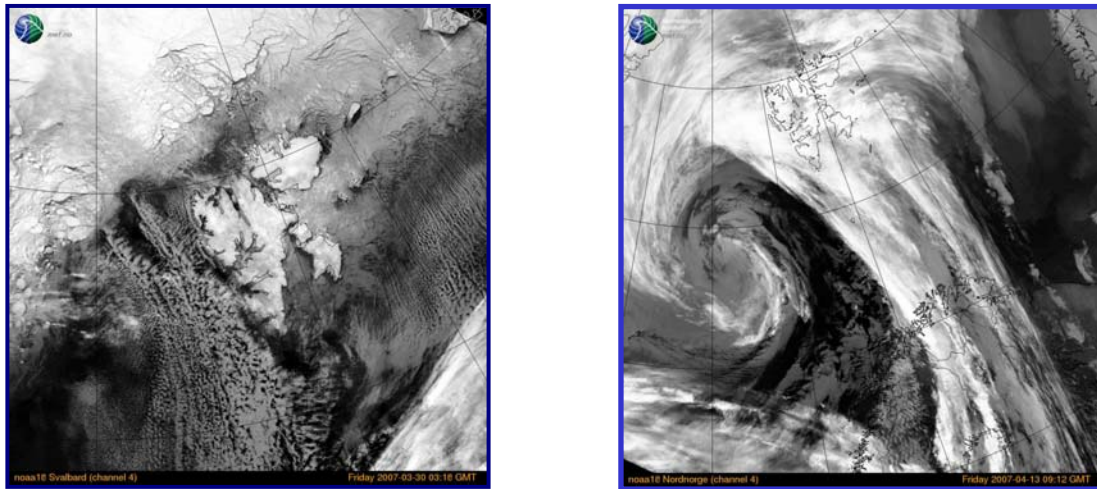


Figure 5.2: NOAA IR satellite images, 30 March 2007, 03:38 UTC (left) and 13 April 2007, 09:12 UTC (right). Courtesy of the Norwegian Meteorological Institute, Tromsø, Norway.

power cannot be assumed as constant. It was not possible to switch on the lidar again during a flight after the laser was turned off and got cold. In combined lidar / in situ flights, switching several times between the instruments was therefore not possible. This additional constraint had to be taken into account for flight planning. The temperature drop decreased especially the 532 nm signal due to the narrow width of the interference filter (0.15 nm), as its peak transmission is temperature dependent (typically 0.021 nm / °C, Melles Griot, 2004). Consequently, the signal to noise ratio was reduced, which resulted in the necessity of longer integration times for the data evaluation. Due to non constant temperatures in the optical unit, the lidar system constant cannot be assumed the same throughout the measurements.

5.5 Synoptic situation

The prevailing meteorological situation from 26 March to 17 April 2007 was characterized by northerly flow above Svalbard, as a result of strong low pressure systems situated mainly south-east of the islands above the Barents Sea. A typical example, Fig. 5.1 (left), shows the mean sea level (MSL) pressure of 30 March (ECMWF T799/L91 Forecasts). Associated with the northerly flow and cold air masses advected from the sea ice, the temperature in Svalbard was quite cold at the beginning, down to -25 °C. The wind speed was generally low, with casual gusts above 10 m s⁻¹ on some days. As a consequence of the strong temperature gradient between the air and ocean, the typical cloud pattern were convective cloud streets emerging above the open ocean in flow direction around Svalbard, as shown by the AVHRR satellite image of 30 April 2007, 03:38 UTC in Fig. 5.2 (left). The cloud structures were in general well captured by ECMWF forecasts. Figure 5.3 shows an example of a CALIPSO satellite track and the forecast of the cloud cover along the track, which consisted of boundary layer clouds. The island of Spitsbergen itself was often at least partly cloud free, and lee effects led to cloud free areas directly south of Svalbard. On 4 April, a low pressure system south-west of Svalbard disturbed the prevailing northerly flow and brought cirrus cloud cover and higher wind speeds from the East. As the low propagated eastwards, the wind direction changed to northerly flow again on 5 April.

Only during the last week of the campaign, low pressure systems in the South caused the wind direction change significantly, and warmer air masses with temperatures above -10 °C were advected from the South-East. Cirrus shields were found in connection with the low pressure

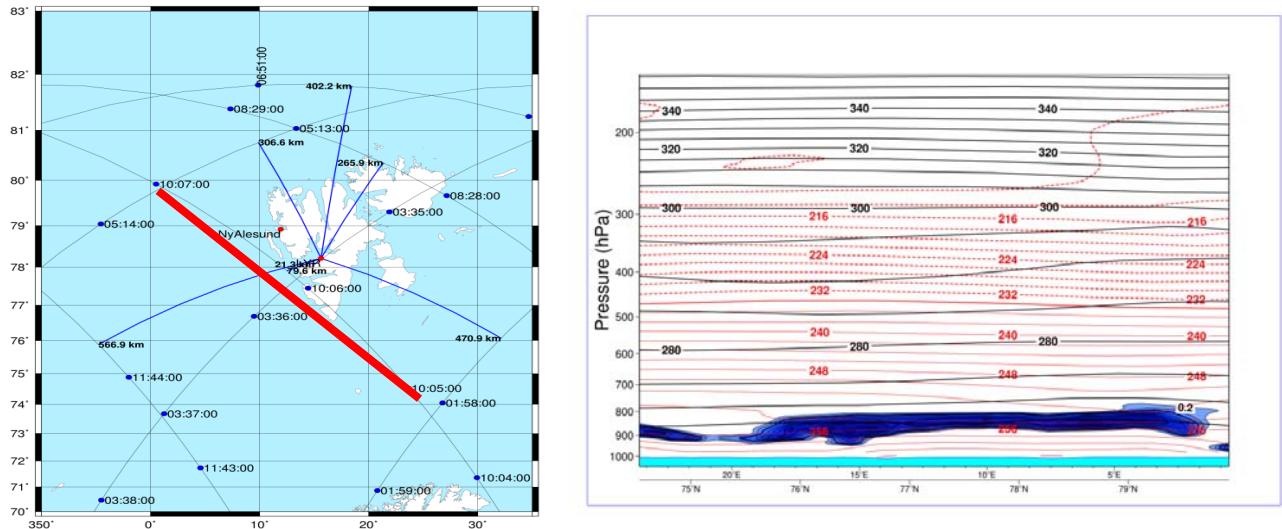


Figure 5.3: CALIPSO satellite tracks on 9 April 2007 (left) and ECMWF forecast of cloud cover along the closest track for 9 April 2007, 12 UTC (right). Provided by Andreas Dörnbrack.

systems. Fig. 5.2 (right) shows the IR satellite picture of a low level system approaching Svalbard on 13 April 2007. The cirrus clouds can clearly be distinguished. Figure 5.1 (right) shows the corresponding ECMWF forecast of MSL pressure. Temperature profiles of radio sounding performed in Ny-Ålesund show a significant increase of atmospheric temperatures throughout the troposphere and stratosphere in the second half of April (Fig. 5.4, left). The sea ice covered area during the ASTAR 2007 campaign is shown in Fig. 5.4 on the right panel (Spren et al., 2008). Sea ice was found North of Svalbard (at latitudes higher than 80 °N). Many of the usually frozen fjords including the Kongsfjord (Ny-Ålesund) and Isfjord (Longyearbyen) showed open water. Towards the West, the water was open, but in the South-East (Storfjord area), the ice cover extended about 200 km.

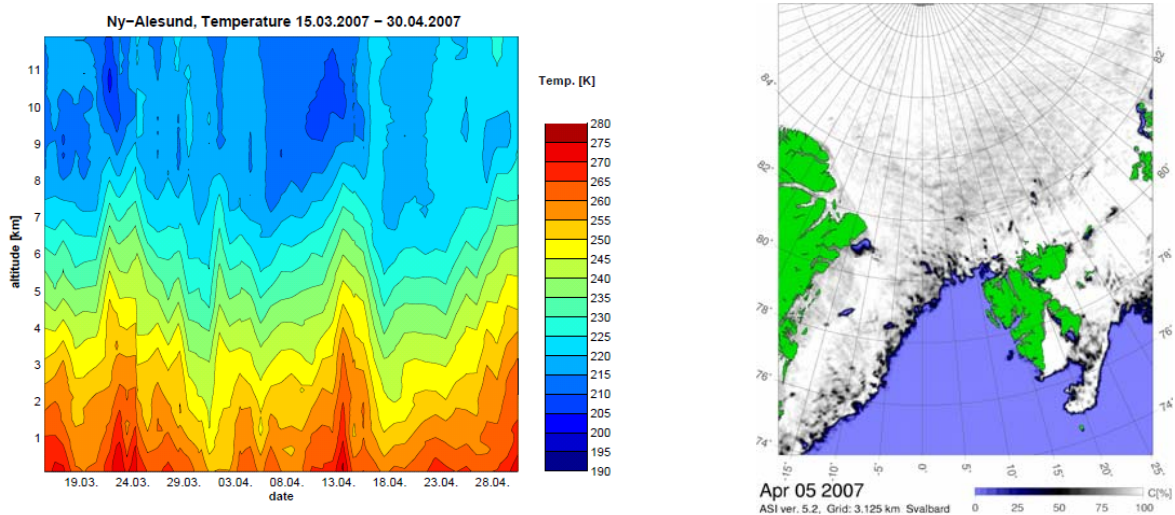
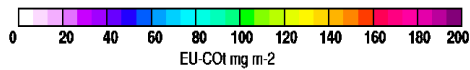
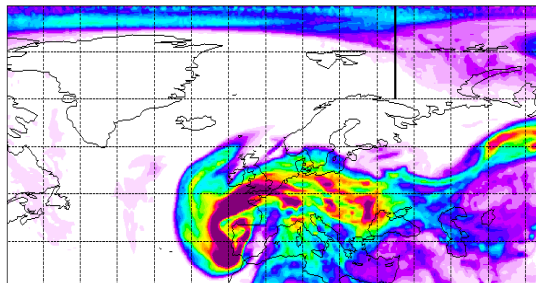


Figure 5.4, left: Temporal development of atmospheric temperatures in Ny-Ålesund. During the second part of April, a warming of the stratosphere can be seen. Right: Sea ice cover around Svalbard during ASTAR 2007 (5 April 2007). Courtesy of the University of Bremen.

Total column of species EU-CO1 for age class 0 - 20.00 DAYS
 Latest analysis time 20070331.180000 Actual time 20070401.120000
 Mean value 0.321E+02 Maximum value 0.443E+03 Minimum value 0.191E+00
 Distance of grid lines 10.0 deg



CROSS SECTION FROM 35.0 TO 35.0 LONGITUDE AND 70.0 TO 90.0 LATITUDE
 EU-CO1 MIXING RATIO FOR AGE CLASS 0 - 20.00 DAYS
 LATEST ANALYSIS 20070331 180000 UTC ACTUAL TIME 20070401 12

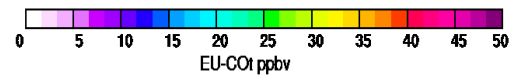
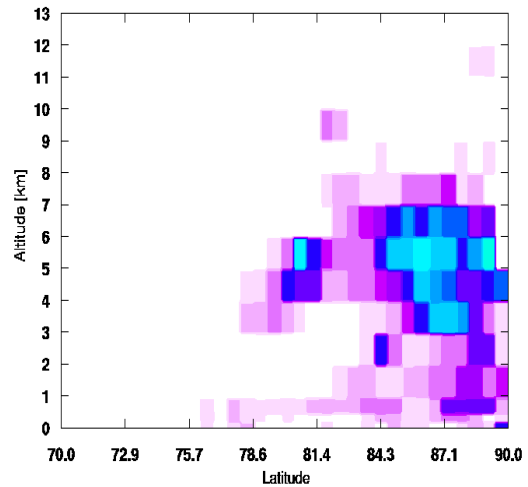
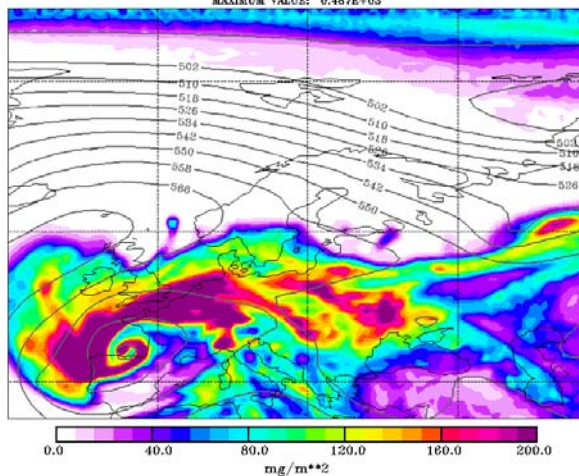


Figure 5.5: Overview of the biomass burning CO tracer (left). The vertical cross section along the black line in the left picture is shown on the right panel. Provided by Andreas Stohl.

5.6 Aerosol and pollution situation

As the investigation of Arctic haze was a pronounced aim of ASTAR, the possible occurrence of enhanced aerosol load from different origins was analyzed. Pollution forecast were provided in order to guide the aircraft to regions of interest.

**TOTAL COLUMN OF EU-CO1
 AND GEOPOTENTIAL HEIGHT CONTOURS AT 500 hPa
 BASED ON GPS ANALYSIS**
 ANALYSIS 20070331 180000 UTC ACTUAL 20070331 210000 UTC
 MAXIMUM VALUE: 6.487E+03



Total column of species EU-CO1 for age class 0 - 20.00 DAYS
 Latest analysis time 20070413.180000 Actual time 20070414.120000
 Mean value 0.362E+02 Maximum value 0.320E+03 Minimum value 0.191E+00
 Distance of grid lines 5.0 deg

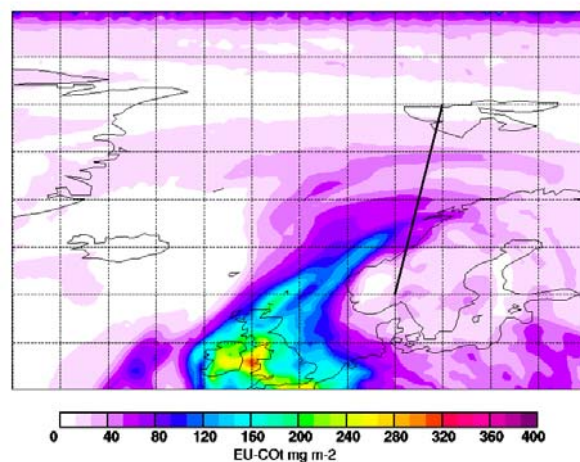


Figure 5.6: Overview of the European CO tracer calculated by FLEXPART forecast. The left picture is a forecast of the beginning (31 March 2007), the right picture is of the end of the campaign (14 April 2007). Different color codes are used. Provided by Andreas Stohl.

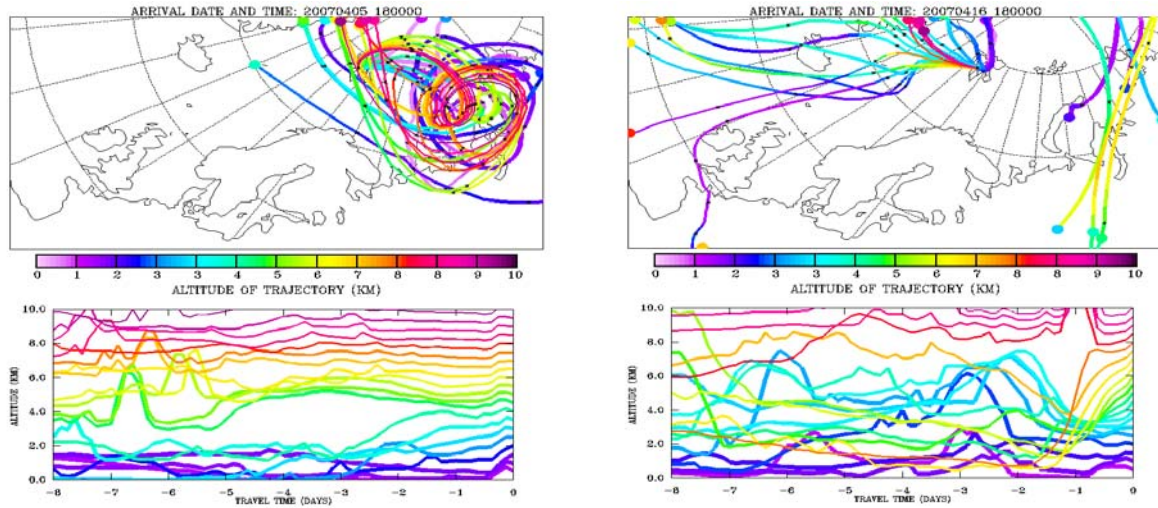


Figure 5.7: HYSPLIT backwards trajectories calculated for 5 April 2007 (left) and 16 April 2007 (right).

Biomass burning aerosol did not reach the Svalbard area during the ASTAR 2007 campaign. An example of FLEXPART forecasts of biomass burning for 31 March is shown in Fig. 5.5. There, the occurrence of aerosol was only predicted further North mainly at an altitude of 3 - 7 km, beyond the operating distance of the Polar-2. Figure 5.6 (left) shows an overview of the European CO tracer typical for the first part of the ASTAR 2007 campaign. On 31 March 2007, very clean conditions with low aerosol number concentrations were encountered over

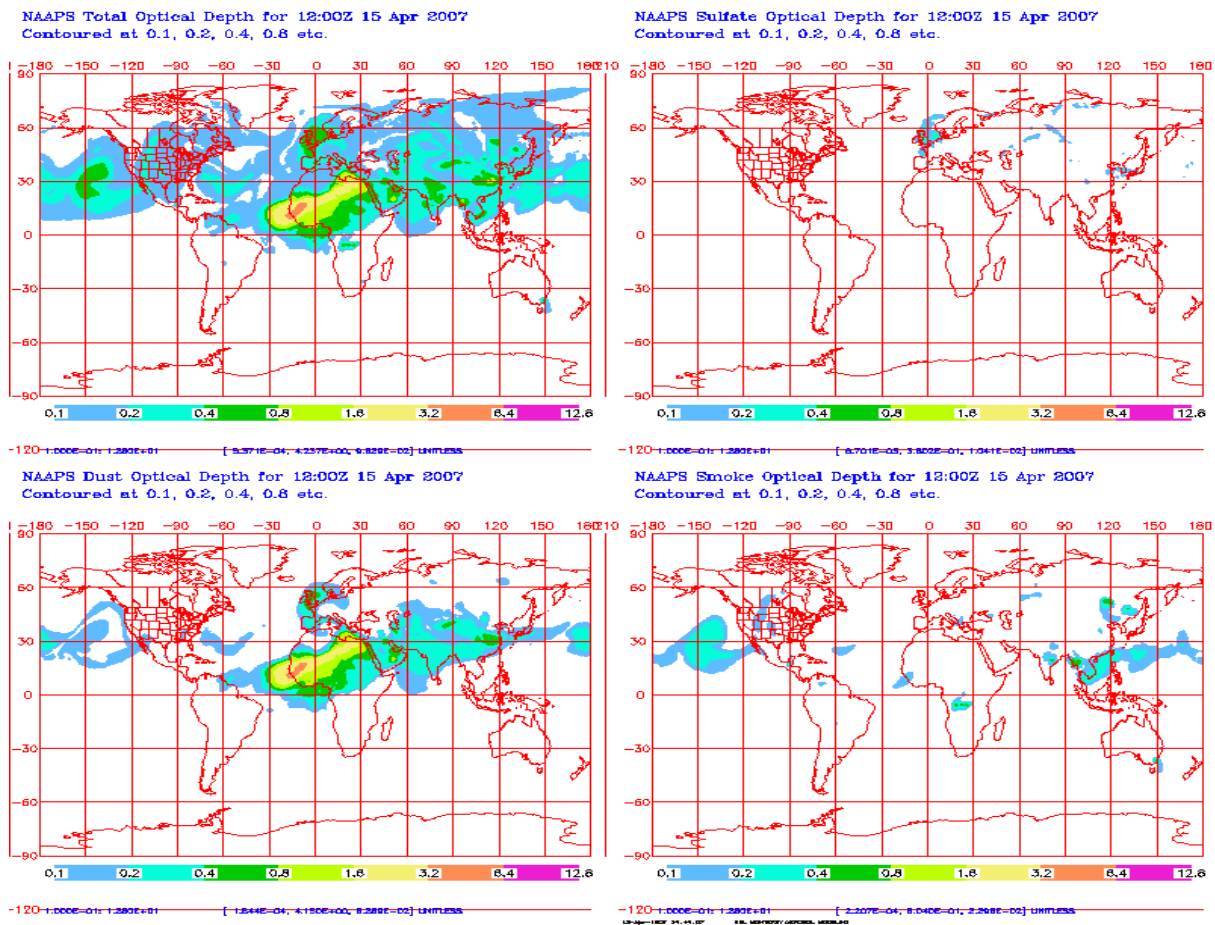


Figure 5.8: NAAPS aerosol forecast of 15 April 2007. The four panels depict the total optical depth, the sulfate optical depth, dust optical depth and smoke optical depth. (Source: <http://www.nrlmry.navy.mil/aerosol/>)

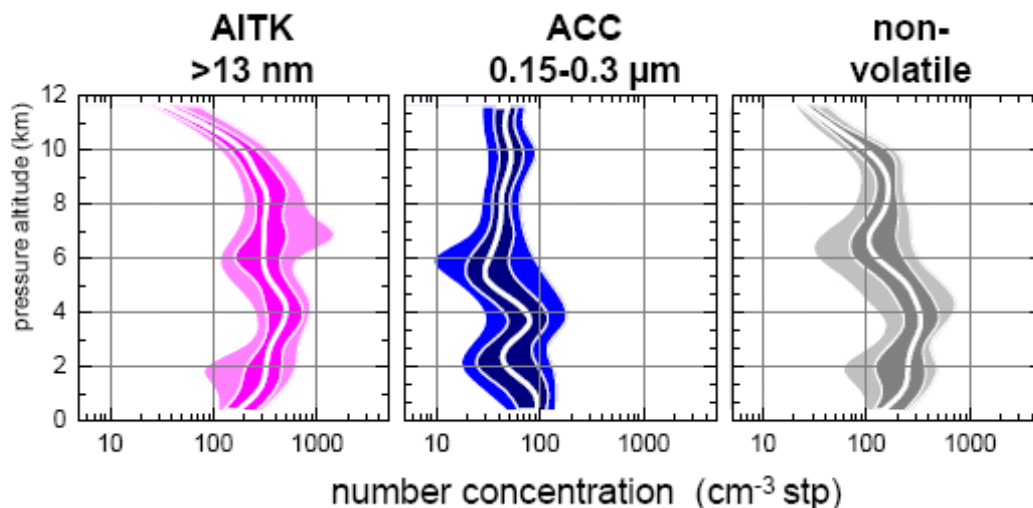


Figure 5.9: Preliminary results of the aerosol vertical distribution combining all Falcon flights. Displayed are median, 10-, 25-, 75- and 95-percentiles of Aitken mode, accumulation mode and non-volatile particles. Provided by Andreas Minikin.

Svalbard. The HYSPLIT trajectories of 4/5 April (Fig. 5.7, left) illustrate that at the beginning of the campaign, the air was trapped in the Arctic for more than a week. On 14 April, at the end of the campaign, an enhanced pollution level was predicted near the coast of Norway (Figure 5.6, right). The expected aerosol concentration in the Svalbard area was still low, although air masses were also advected from lower latitudes as shown by HYSPLIT trajectories for 16/17 April (Fig. 5.7, right). FLEXPART calculations for sulfate did not show enhanced values around Svalbard either.

The NAAPS classification of 15 April confirmed the clean air in the surroundings of Svalbard and the enhanced total optical depth and sulfate optical depth at the West coast of Norway (Fig. 5.8).

Generally the air in Svalbard during the ASTAR 2007 campaign was very clean in terms of the aerosol optical depth determined by sun photometer in Ny-Ålesund (Hoffmann et al., 2009) and the aerosol number concentration observed by airborne measurements on board of the Falcon (Minikin, personal communication). However, the size distribution of the aerosol differed from typical clean conditions: In the boundary layer, the number concentration of very small Aitken mode particles (measurement range 13-150 nm) was reduced, while the concentration of accumulation mode particles (150-300 nm) and coarse particles (1-3 μm) was enhanced (Fig. 5.9). The northerly winds at the beginning of the campaign prevented polluted air masses from Eurasia and America from entering the higher latitudes. Both the tracer forecasts and the backward trajectories suggest that the polluted air was trapped more in the South. Only a small part of very old European and biomass burning aerosol arrived in Svalbard via Siberia and the North Pole. It was predicted to be present in the upper parts of the troposphere (3-9 km).

In the last week of the campaign, the backward trajectories suggested air flow from the West. More attention was paid to the North American CO, sulfate, and biomass burning CO tracers. Some slightly polluted layers originating in North America were predicted at higher altitudes. The satellite images of MODIS showed that visible aerosol layers were present West of Norway, around Great Britain and above Iceland (Figure 5.10). For the Polar-2, the pollution plumes were out of reach. The Falcon aircraft with the longer operating range was able to probe polluted European air masses during a flight to Trondheim, Norway, and back on 15 and 16 April 2007.

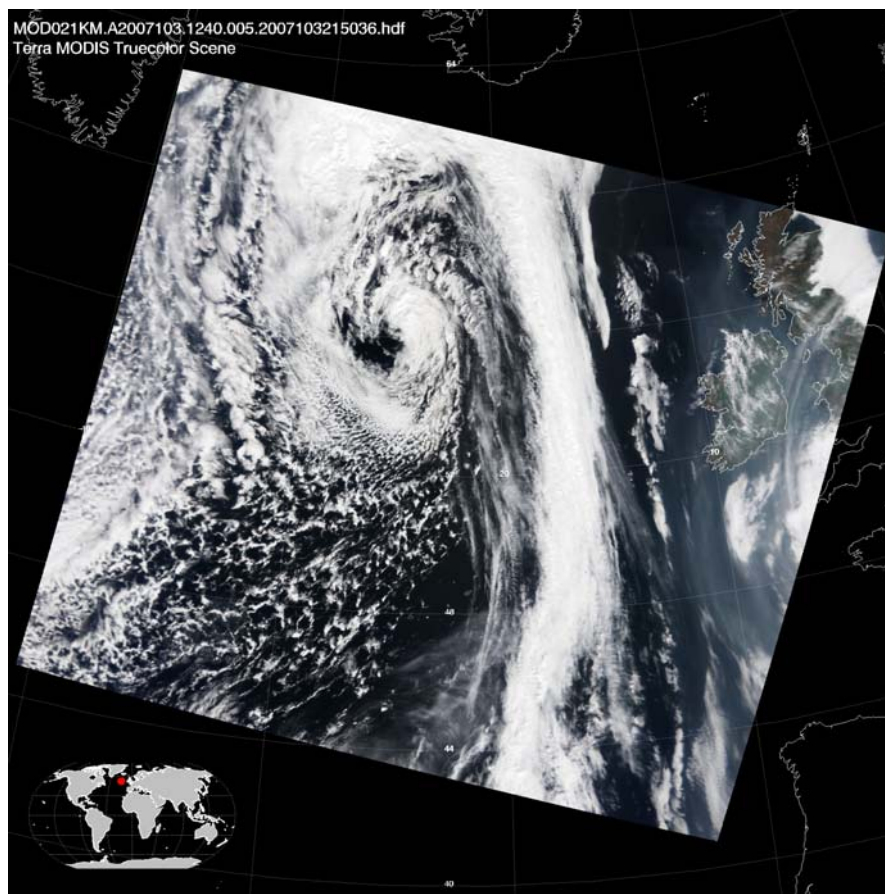


Figure 5.10: MODIS image showing visible aerosol layers West of England on 13 April 2007, 12:40 UTC.

In contrast to particle concentrations and optical depth, the average mixing ratios of reactive NO_y were found to be relatively enhanced during the campaign. Moreover, thin layers with enhanced concentrations of SO_2 were observed. From the ratio $R = \frac{\text{SO}_2}{\text{NO}_y}$, the source type of

the pollution can be determined (Arnold et al., to be published). In one case, on 8 April 2007 during a flight towards the North, the high value of $R > 40$ could be traced back to the Ni-Cu smelting industry complex in Norilsk (69° N , 88° E , Shaw, 1982, Arnold et al., to be published). Sulfate aerosol formed from the precursor gas SO_2 . These findings led to the conclusion that from a chemical point of view, the ASTAR 2007 campaign took place under the typical springtime Arctic haze conditions.

In conclusion, the concentration of Arctic aerosol was very low, the typical spring time Arctic haze with significant aerosol load was not observed. Concerning aerosol, the AMALi detected a slight increase of particles in the boundary layer, probably of local origin. However, the AMALi data evaluation and analysis focused on cloud investigation in combination with the in situ and albedometer measurements. In the following two chapters, case studies of tropospheric Arctic clouds are presented.

6 Case study: Subvisible midlevel ice cloud

In this chapter, a case study of a subvisible midlevel ice cloud is presented (Lampert et al., 2009a). The term “midlevel” is used to distinguish the ice cloud observed at 3 km altitude from high cirrus clouds. On a first glance, optically thin midlevel ice clouds are similar to high-altitude cirrus clouds. However, they have a different cloud forcing due to higher temperatures and other microphysical properties. There are indications that subvisible clouds occur frequently in the Arctic winter (Wyser et al., 2008), but the typical cloud properties and radiative effects have not been investigated thoroughly.

According to the definition by Sassen et al. (1989), subvisible clouds exhibit an optical thickness of less than 0.03 at a wavelength of 532 nm. The optical thickness of subvisible clouds is therefore comparable to slightly enhanced aerosol load, though lower than the typical Arctic haze pollution. Arctic haze usually may reach a higher optical depth of up to 0.3 at 532 nm wavelength (Herber et al., 2002) and thus influences significantly the radiation budget (e.g. Blanchet and List, 1983, Rinke et al., 2004).

So far subvisible clouds have mainly been studied in the form of optically thin cirrus in the tropics and midlatitudes (Beyerle et al., 2001, Cadet et al., 2003, Thomas et al., 2002, Peter et al., 2003, Spichtinger et al., 2005, Immler and Schrems, 2006, Immler et al., 2008). Comparable observations in Arctic regions are rare. Especially, ground-based observations of subvisible clouds in the Arctic are obscured by the almost omnipresent optically thick liquid or mixed-phase boundary layer clouds (see Chapt. 2).

The relevance of optically thin Arctic clouds with regard to the Earth's energy budget was investigated in the context of diamond dust (precipitation of ice crystals in “cloudless” sky, Shcherbakov et al., 2006) which has been shown to exert a negligible effect on the radiation budget (Intrieri and Shupe, 2004). However, the authors showed that almost all the events were caused by optically thin liquid water clouds in the boundary layer, which in winter time have a significant warming effect as they prevent the thermal infrared radiation emitted by the surface from escaping into space. The radiative impact of subvisible midlevel ice clouds, especially in the high Arctic, is difficult to quantify. To deduce the radiative effects of Arctic clouds, the knowledge of their microphysical properties is crucial (Harrington et al., 1999).

During the ASTAR 2007 campaign, a subvisible and glaciated cloud at an altitude of 3 km with a horizontal extent larger than 60 km was observed over the Barents Sea south of Svalbard (76.3-76.6° N, 21-23° E). The ice cloud was intensively probed by alternating airborne remote sensing and in situ instruments onboard of the Polar-2 aircraft. The consecutive deployment of the sensors provided nearly simultaneous measurements of the cloud properties in terms of backscattering coefficient and depolarization ratio by lidar remote sensing (zenith-looking configuration), solar spectral as well as thermal infrared radiation, standard meteorological parameters, and in situ microphysical cloud properties. Operational meteorological analyses provided information on the ambient atmospheric state and on the cloud's development.

Airborne observations of the subvisible Arctic ice cloud were performed in two consecutive stages. First, the lidar and radiation sensors detected the cloud from below as the aircraft flew eastwards at an altitude of 160 m above sea level between 11:54 UTC and 12:09 UTC. The aircraft returned to the cloud center at an altitude of 2820 m as indicated by lidar remote sensing. There, the ice cloud layer was probed directly by in situ instruments from 12:28 UTC to 12:34 UTC. Taking into account the advection of the air during the 30 minutes between the lidar detection and the in situ observation, the aircraft could not probe exactly the same air masses. However, the almost stationary atmospheric conditions show that the same cloud was observed.

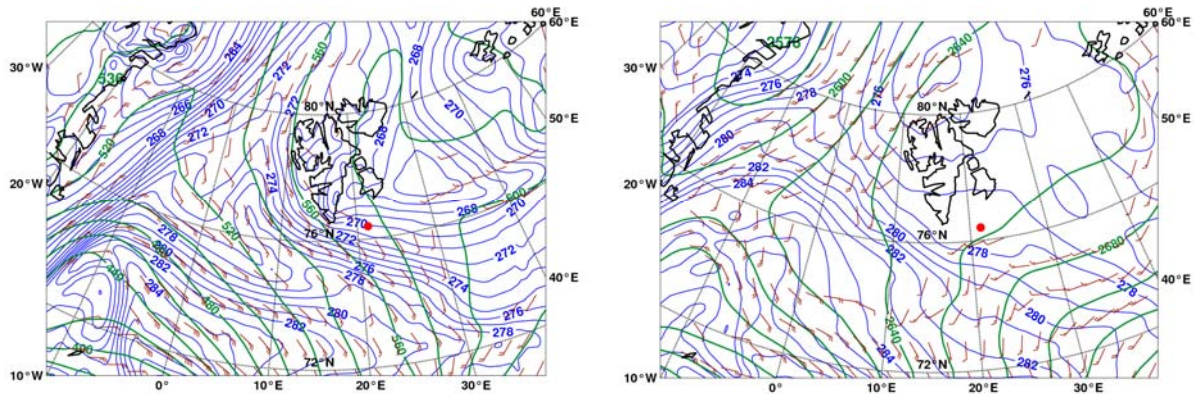


Figure 6.1: ECMWF operational analyses: Equivalent potential temperature (blue contour lines, K), geopotential height (green contour lines, m), and wind speed (barbs, m/s) valid at 10 April 2007, 12:00 UTC at 925 hPa (left) and at 700 hPa (right). The position of the sampled ice cloud is marked by a red dot. Provided by Andreas Dörnbrack.

6.1 Meteorological situation

The data were obtained on a Polar-2 research flight in the vicinity of Svalbard on 10 April 2007 between 11:05 and 13:59 UTC. The area where the cloud was observed is indicated in Fig. 6.1 by a red dot. At this time, cold Arctic air influenced Svalbard whereas the warm sector of a trough propagating eastward dominated the wind field west of the islands. Thus, the near-surface south-easterly winds were weak and mostly aligned with the Arctic frontal zone as shown by the equivalent potential temperature distribution and the wind field at the pressure surface of 925 hPa in Fig. 6.1 (left). At higher altitudes, the weak geopotential height gradients and the absence of upper-level forcing caused a weak south-westerly flow over Svalbard; cf. the flow field at 700 hPa in Fig. 6.1 (right). The wind speed and direction measured during the flight at the altitude of the cloud were 4.5 m s^{-1} and 253° , respectively.

The operational ECMWF analyses charts reveal a north-south oriented band of increased relative humidity over ice (RHI) over Svalbard (Fig. 6.2). In the region of the airborne observations, RHI attained values of $\approx 90\%$ at 700 hPa (Fig. 6.2, right). Operational forecasts used for the flight planning predicted cirrus at higher altitudes. In the operational analyses valid at 12:00 UTC, a formerly coherent region of $\text{RHI} \approx 100\%$ was perturbed by ascending upper tropospheric air leading to smaller RHI values in the measurement area, cf. RHI at $p = 400 \text{ hPa}$ in Fig. 6.2 (left).

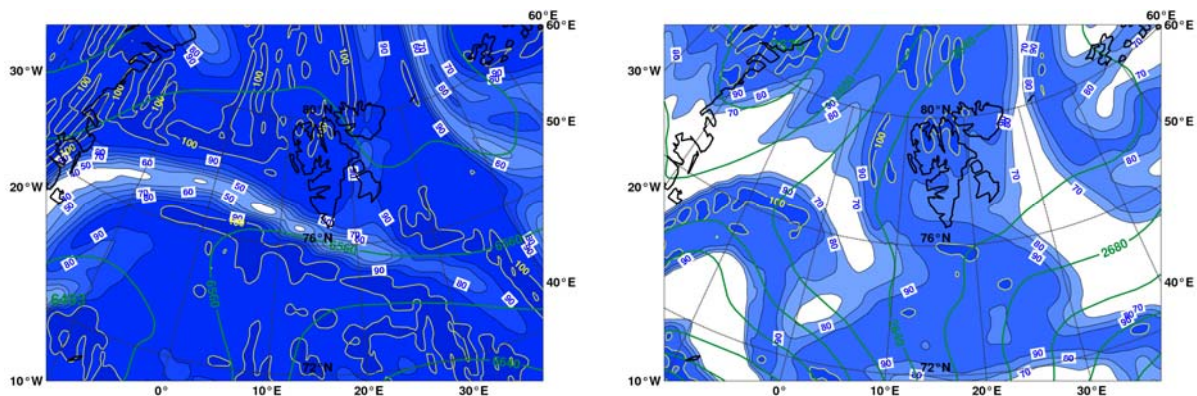


Figure 6.2: ECMWF operational analyses: Relative humidity (blue shading, yellow contour lines $\text{RHI} > 100\%$), and geopotential height (green contour lines, m), valid at 10 April 2007, 12:00 UTC at 400 hPa (left) and at 700 hPa (right). Provided by Andreas Dörnbrack.

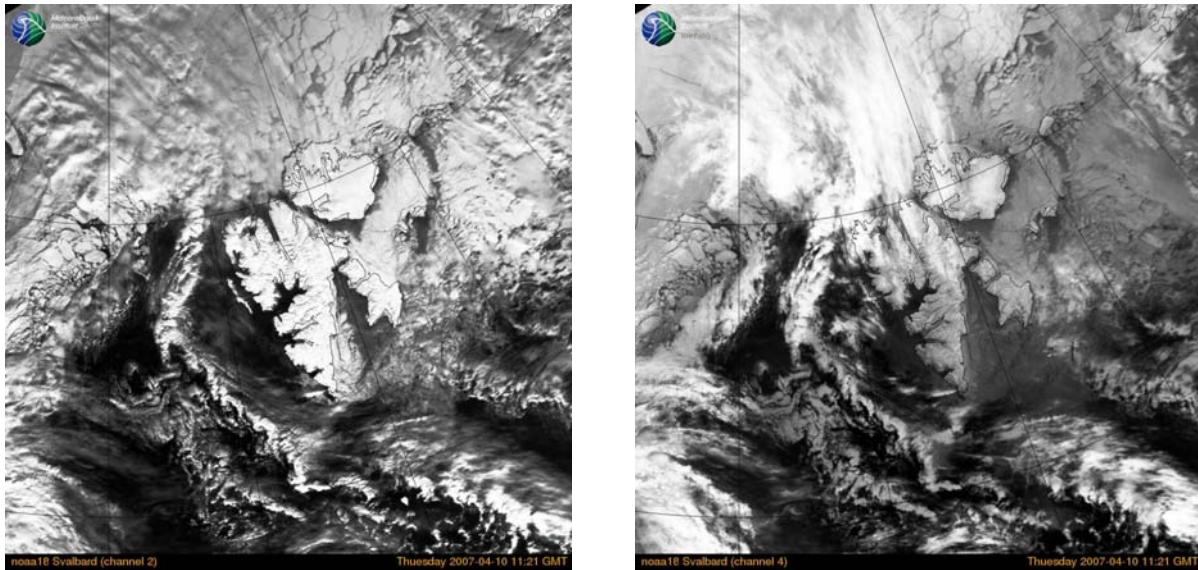


Figure 6.3: NOAA satellite imagery on 10 April 2007, 11:21 UTC. Left panel: visible channel (0.58-0.68 μm), right panel: near infrared channel (0.725-1.10 μm). Courtesy of the Norwegian Meteorological Institute, Tromsø, Norway.

In the cloud itself (at 683 hPa), a mean air temperature of -24.3 °C was found. During ascent and descent of the aircraft, a small temperature inversion of less than 2 K was measured around 500 m above sea level. The relative humidity related to water saturation inside the cloud was $79 (\pm 10)$ %. This corresponds to a relative humidity above ice of ≈ 100 % (almost saturated).

The NOAA satellite images (Fig. 6.3) confirm the ECMWF analyses. An elongated band of cumulus clouds west of Svalbard marked the air mass boundary whereas the area south and south-east of Svalbard was almost free of low-level clouds. The near infrared channel of the NOAA satellite reveals high-level cirrus clouds north of Svalbard and cirrus associated with the approaching warm front in accordance with the RHI values for 400 hPa as shown in Fig. 6.2 (left).

To examine the history of the observed air parcels, the three-dimensional trajectory model LAGRANTO (Lagrangian Analysis Tool, Wernli and Davies, 1997) was applied. It allows the calculation of kinematic Lagrangian trajectories for air parcels. The time-trace of a parcel's position and its physical properties are based on regular gridded analysis fields of the three dimensional wind vector. The parcel positions are calculated for a half-hour time step with linear interpolation of the wind field at off-grid locations. LAGRANTO is driven by the wind fields of the 6-hourly operational ECMWF analyses. Further meteorological parameters can be traced along the trajectory. As output, Lagranto saves latitude, longitude and pressure as well as the traced parameters (relative humidity above ice, RHI, in this case).

Trajectories arriving between 600 hPa and 750 hPa in the observational area at 10 April 2007, 12:00 UTC, reveal a slow propagation from south-west, see Fig. 6.4. In this altitude region, the absence of significant deformation and mixing indicates that the air masses kept their properties for the past 24 hours. Before this time, the air parcels slowly ascended and, eventually, the relative humidity above ice increased to values close but below 100 % in the global meteorological analyses. Trajectories arriving at 400 hPa were descending with decreasing RHI in time (not shown).

The stable atmospheric conditions with low wind speeds continued in the same area (76.45° - 76.6° N, 20.8° - 21.3° E) throughout the next day. During a CALIOP overflight on the next morning, 11 April at 09:53 UTC, an optically thin cloud at around 3 km altitude was recorded.

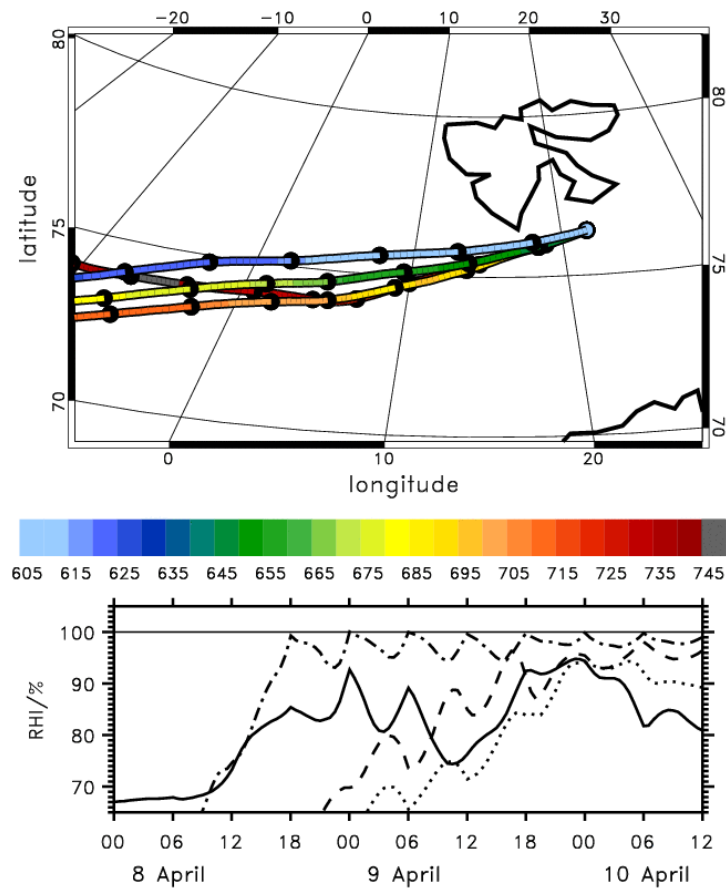


Figure 6.4: Backward trajectories released at 21.8°E and 76.4°N on 10 April 2007 at 12:00 UTC. Top panel: Pressure along the trajectories for $p_{\text{start}} = 750, 700, 650,$ and 600 hPa, respectively. The black bullets are plotted every 6 hours. Bottom panel: relative humidity over ice RHI for $p_{\text{start}} = 750$ (solid line), 700 (dotted line), 650 (dashed line), and 600 (dash-dotted line) hPa, respectively. Provided by Andreas Dörnbrack.

The isobaric flow on this following day came from south-east without significant lift of the air masses in the last 24 h.

6.2 Optical and microphysical characterization

6.2.1 Lidar remote sensing

The AMALi was deployed onboard the Polar-2 aircraft in zenith-looking mode. In order to obtain a sufficiently high signal to noise ratio larger than 15 for the 532 nm channel at the cloud top, the data were averaged over 15 s. With a mean ground speed of the aircraft of 62 m s^{-1} , the horizontal resolution of the lidar data amounted to about 930 m.

The vertical profiles of the backscattering ratio at 532 nm wavelength along the flight track reveal the presence of an optically thin ice cloud from 11:52 UTC to 12:09 UTC as shown in Fig. 6.5 (top). Its geometrical depth varied between 500–1000 m. The cloud base was located at about 2500 m and the cloud top descended along the flight track from 3500 m to 3000 m altitude. After 12:00 UTC, a cirrus cloud was recorded above the optically thin ice cloud at an altitude of 6000–6500 m (not shown in Fig. 6.5).

The particle backscatter coefficient β^{part} for $\lambda = 532 \text{ nm}$ as calculated with the standard Klett approach (see Chapt. 3) exhibited values between $0.3(\pm 0.1) \cdot 10^{-6} \text{ m}^{-1} \text{ sr}^{-1}$ and $5(\pm 1) \cdot 10^{-6} \text{ m}^{-1} \text{ sr}^{-1}$ throughout the cloud. The lidar ratio LR was set to 21 sr as a preliminary first guess,

which is a typical value for ice clouds (Ansmann et al., 1992, Giannakaki et al., 2007). For the calculation of the particle backscatter coefficient, the assumed LR is not critical: The Arctic atmosphere apart from the subvisible cloud was so clear that Klett solutions with a LR of 21 (± 10) sr were very similar to each other (with errors less than 2 %). The minimum resolution for the particle backscatter coefficient of the AMALi is in the range of $(1 \pm 0.5) \cdot 10^{-7} \text{ m}^{-1} \text{ sr}^{-1}$. However, for calculating the extinction coefficient, the assumption of the lidar ratio is crucial (cf. discussion in Sect. 6.3.3). Assuming a lidar ratio of 21 sr, the extinction coefficient in the cloud varied between 0.006 and 0.1 (± 0.003) km^{-1} . The error of the extinction coefficient was estimated according to error propagation with reasonably chosen uncertainties of β^{part} and LR . The uncertainty of LR was assumed as the magnitude of LR itself, 21 sr. As the small values of the backscatter coefficient have the highest relative error, the minimum resolution value ($1 \cdot 10^{-7} \text{ m}^{-1} \text{ sr}^{-1}$) was used for the error in the backscatter coefficient. The uncertainty in the retrieval of the extinction coefficient thus amounts to $3 \cdot 10^{-3} \text{ km}^{-1}$. Furthermore, the cloud optical thickness τ at $\lambda = 532 \text{ nm}$ was calculated by integrating the extinction coefficient from cloud bottom (r_b) to cloud top (r_t):

$$\tau = \int_{r_b}^{r_t} \alpha(r') dr' = \int_{r_b}^{r_t} LR \cdot \beta(r') dr' \quad (6.1)$$

The values varied from subvisible (0.01-0.03) for more than half of the observation time to an upper value of 0.09 (± 0.005). After visual inspection of all lidar profiles and as expected due to the low optical depth $\tau < 0.1$ (You et al., 2006), multiple scattering can be excluded for this case.

The volume depolarization showed significantly enhanced signals with values up to 40 % (Fig. 6.5, bottom). This clearly indicates the existence of non-spherical ice crystals in the observed subvisible midlevel ice cloud (You et al., 2006).

In order to estimate the size of the cloud particles, the color ratio was analyzed. The entire cloud exhibited values of the color ratio of 3 to 4. As these values are clearly smaller than 5, which is the value for particles with an effective diameter exceeding $5 \mu\text{m}$ (Chapt. 3), the existence of particles with an effective diameter smaller than $5 \mu\text{m}$ is demonstrated. However, this is an ill-posed problem, and a precise retrieval of the particle size is impossible with the two lidar wavelengths only. Such small cloud particles with a size smaller than $5 \mu\text{m}$ and very low concentration are also difficult to detect with the in situ sensors applied here (see Sect. 6.2.2).

6.2.2 In situ measurements

The center of the subvisible midlevel ice cloud was probed with the in situ instrumentation at the altitude of 2820 m, following the guidance from the lidar measurements collected 30 min earlier. During this flight sequence, microphysical data were obtained between 12:29 and 12:34 UTC. However, one has to be aware that due to the time delay, the comparison of the data is limited.

The independent in situ instruments used for this analysis, the Polar Nephelometer, the Cloud Particle Imager, and the Forward Scattering Spectrometer Probe, are described in Sect. 5.3.

For the interpretation of the PN measurements, different microphysical models were tested. The best fit of the measurements was achieved using a combination of spherical droplets with diameters ranging from $1 \mu\text{m}$ to $100 \mu\text{m}$ and deeply rough hexagonal columns (with an aspect ratio of 2) with maximum dimension ranging from $20 \mu\text{m}$ to $900 \mu\text{m}$. The retrieval is further discussed in Sect. 6.3.1. As the PN measurements were not limited by the small particle concentration, the retrieval of microphysical and optical properties from the in situ instruments is mainly based on PN data.

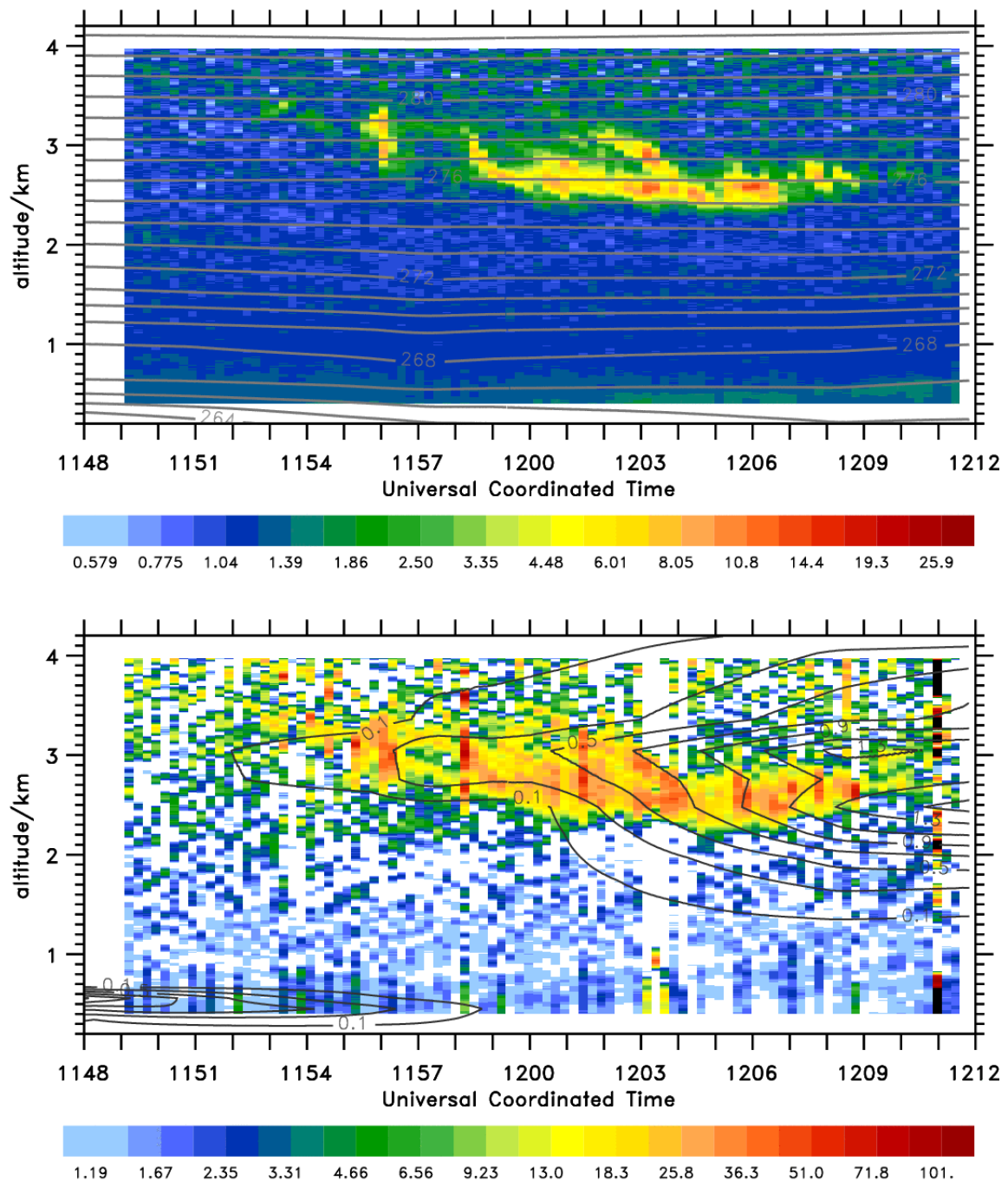


Fig. 6.5: Zenith measurements of backscattering ratio at 532 nm (top panel) and volume depolarization (bottom panel) with 15 s resolution along the flight track of the Polar 2. The data are smoothed vertically about 3 height steps. Large values of the depolarization with an extension in vertical bands are artifacts. Superimposed are contour lines of the potential temperature (K, top) and the cloud ice water content (mg kg^{-1} , bottom). Meteorological data: ECMWF operational analyses interpolated in space and time on the flight track. ECMWF analyses provided by Andreas Dörnbrack.

Only 4 single ice crystals were recorded with the CPI during this time, which had column shape with a length of 100-200 μm (Fig. 6.6). The rounded edges of the ice crystals suggest that the cloud was in an evaporation process (see Sect. 6.1). The very few ice crystals detected indicate that (i) the particle concentration was very low and (ii) most of the ice crystals evidenced by the PN were smaller than about 100 μm . Furthermore, the FSSP did not detect particles. This means that the concentration of ice crystals with a size smaller than 50 μm was



Figure 6.6: Images of the four single ice crystals detected by the CPI in the thin cloud at about 3 km altitude. Provided by Jean - François Gayet.

below the instrument's detection threshold. The low concentration was confirmed by the analysis of the PN data, which measured single ice crystals although the instrument was designed to probe an ensemble of cloud particles. Therefore, assuming the detection of single particles and knowing the sampling volume (150 cm^3 with a true air speed of 70 m s^{-1} at 20 Hz), the ice particle concentration can be estimated from the extinction coefficient and the effective diameter.

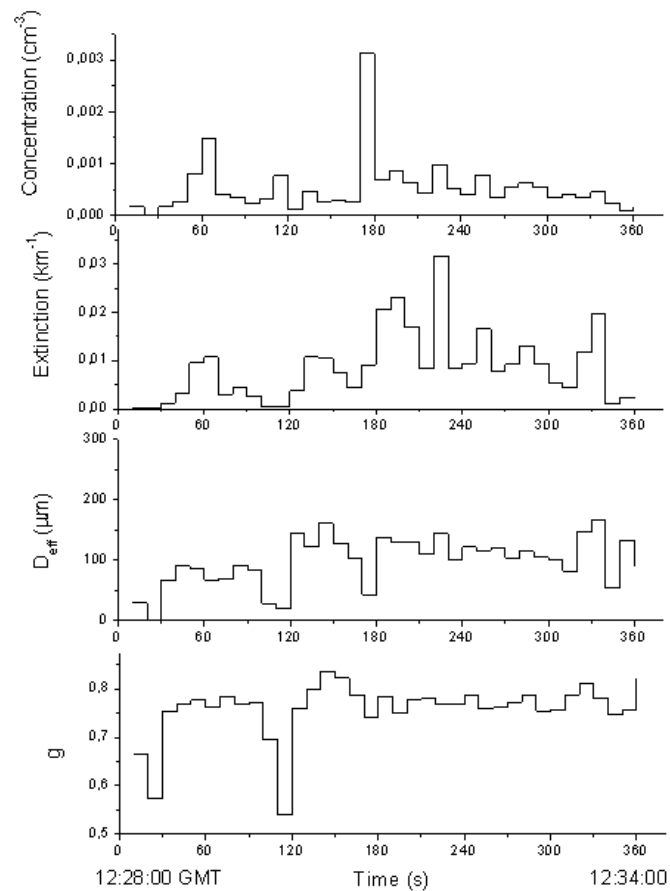


Figure 6.7: Time series of the concentration, extinction coefficient, effective diameter D_{eff} , and asymmetry parameter g retrieved from the Polar Nephelometer. Provided by Valery Shcherbakov.

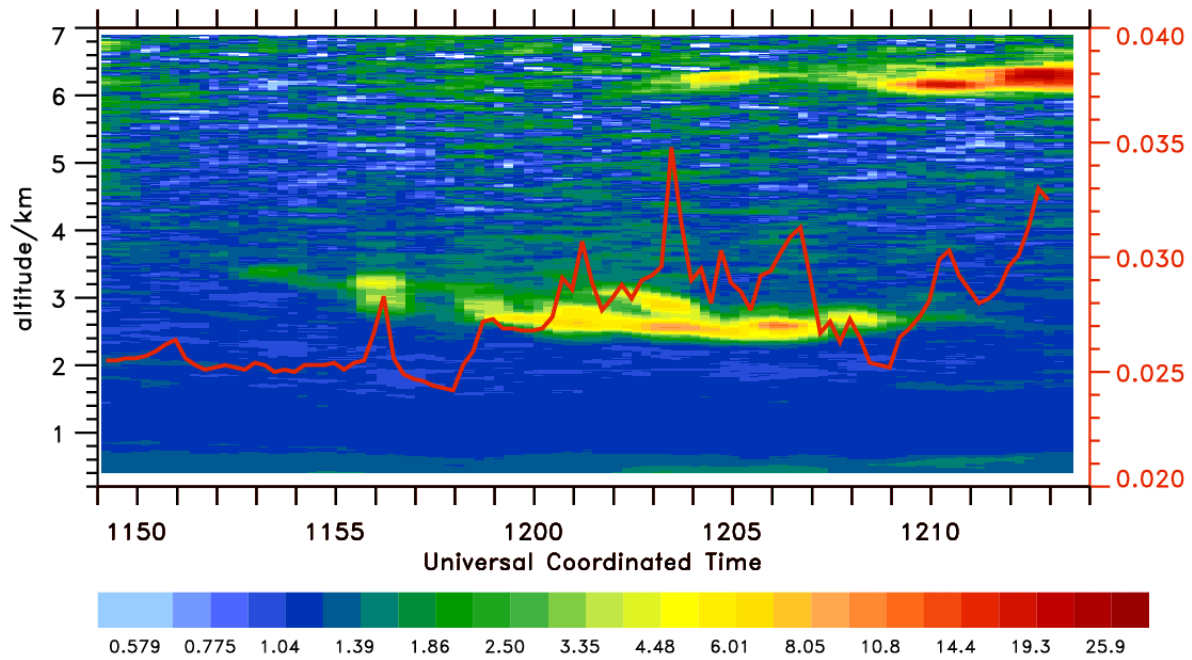


Fig. 6.8: Zenith measurements of backscattering ratio at 532 nm smoothed vertically about 3 height steps with 15 s resolution as in Fig. 6.5. Superimposed is the radiance in $\text{W sr}^{-1} \text{m}^{-2} \text{nm}^{-1}$ at 532 nm (red line). After 12:00 UTC, a cirrus cloud appears at an altitude of about 6 km. Radiance provided by André Ehrlich.

The time series (every 10 s) of these quantities together with the asymmetry parameter g are displayed in Fig. 6.7. If there were several particles in the sampling volume, the effective diameter would be overestimated and the concentration underestimated. Integrating the PN data over the four minutes cloud sequence, the mean values of the extinction coefficient and asymmetry parameter are 0.01 km^{-1} and 0.78, respectively, and the concentration of ice particles and mean effective diameter are 0.5 l^{-1} and $100 \mu\text{m}$, respectively. For averaging over the densest part of the cloud (30 s), the extinction coefficient and the asymmetry parameter are 0.02 km^{-1} and 0.77, respectively. The extinction coefficient values are in the same order of magnitude with the lidar data (see Sect. 6.2.1). At the same time, they are much below the typical values of midlatitude cirrus clouds as presented in Gayet et al. (2006). This clearly indicates that a subvisible midlevel ice cloud was probed. Most of the asymmetry parameter values fall within the range that is typical of cirrus clouds shown by Gayet et al. (2006), i.e., a cloud containing ice particles was sampled. For spherical water droplets the asymmetry parameter is about 0.85, significantly larger than the values reported here.

6.2.3 Radiation data

The SMART-Albedometer described in Sect. 5.3 was operated during the flight of 10 April 2007. In the case of the optically thin ice cloud investigated in this study, the observed downwelling nadir radiance I_{λ}^{\downarrow} was analyzed for the flight at 160 m altitude, about 2300 m below cloud base. I_{λ}^{\downarrow} is most sensitive to the slightly enhanced scattered solar radiation below the cloud. The overall uncertainty of I_{λ}^{\downarrow} was estimated with 6 % at the wavelength of 532 nm. Additionally, pyrgeometer measurements of upwelling and downwelling thermal infrared irradiance were used to confirm that the modeled data in this spectral range were appropriate. The downwelling radiance I_{λ}^{\downarrow} below the cloud showed a clear evidence of the optically thin cloud above. Enhanced scattering of solar radiation by the cloud particles increased I_{λ}^{\downarrow} as shown by the time series in Fig. 6.8 (superimposed red line). The clear sky value of 0.025 W

$\text{m}^{-2} \text{sr}^{-1} \text{nm}^{-1}$ at 532 nm was measured shortly before the lidar detected the optically thin cloud. Simultaneous with the increasing lidar backscattering ratio, also $I_{532\text{nm}}^{\downarrow}$ increased to a maximum value of $0.030 \text{ W m}^{-2} \text{sr}^{-1} \text{nm}^{-1}$. From 12:00 UTC the cirrus detected by the lidar at 6000–6500 m altitude led to a further increase of $I_{532\text{nm}}^{\downarrow}$ up to $0.036 \text{ W m}^{-2} \text{sr}^{-1} \text{nm}^{-1}$ (Fig. 6.8). The response of the downwelling thermal infrared irradiance (pyrgeometer measurements) qualitatively had a similar behavior as the solar radiance and lidar optical thickness (not shown). Below the ice cloud the pyrgeometer values increased simultaneously with the lidar optical thickness from values of 172 W m^{-2} to 176 W m^{-2} . After 12:00 UTC, the additional cirrus cloud above the optically thin ice cloud led to further increased values measured by the pyrgeometer.

6.3 Discussion

6.3.1 Microphysical properties

An inversion of the PN data to retrieve microphysical and optical parameters was performed by Olivier Jourdan. Jourdan et al. (2003a) showed that the information content of the PN measurements is sufficient to retrieve an equivalent component composition and particle size distribution for a given ice cloud. Following the methodology established in Jourdan et al. (2003b), the ice cloud average angular scattering coefficients (ASC) measured by the PN at the wavelength 800 nm and scattering angles 6.7° – 155° were extrapolated to the forward and backward scattering directions. Afterwards, the corresponding ASC and extinction coefficient at a wavelength of 532 nm can be assessed in order to derive a representative lidar ratio for the interpretation of the AMALi measurements. The crucial point of this methodology concerns the choice of the microphysical model that best reproduces the optical and microphysical observations.

The inversion method for the PN data is based on a bi-component representation of cloud composition and constitutes a non-linear least squares fitting of the scattering phase function using smoothness constraints on the desired particle size distributions (PSD). Measurement errors at each angle and PSD's values for each size, in the sense of probability density function, are assumed to be described by the lognormal law, which is the most natural way to take a priori information about the non-negativity of these quantities (Tarantola, 1994). No analytical expression for the particle size distribution is assumed for the converging solution in this method. The only constraint in this connection is smoothness, needed to avoid an unrealistic jagged structure of the desired size distribution, because the inverse problem is ill posed without constraints. The inversion method is designed for the retrieval of two volume particle size distributions simultaneously, in this case one for hexagonal ice columns and another for spherical ice crystals. The technique needs, however, to specify a lookup table containing the scattering phase functions of individual ice crystals. Lookup tables containing the angular scattering coefficients of spherical ice crystals, droxtals, columns with three aspect ratios (2,5,10), plates with 4 aspect ratios (0.1, 0.5, 0.2, 1), hollow columns, 6 branch bullet rosettes, and aggregates were calculated.

Three roughness parameters for ice particles were also considered (smooth, moderately rough, and deeply rough). The roughness of the surface can be defined as a small scale property similar to surface texture. In the simulation, the rough surface is assumed as composed of a number of small facets which are locally planar and randomly tilted from their positions corresponding to the case of a perfectly plane surface. The tilt distribution is supposed to be azimuthally homogeneous. It is specified by a two parametric probability distribution function including a scale parameter σ_s and the shape parameter η (which determines the kurtosis).

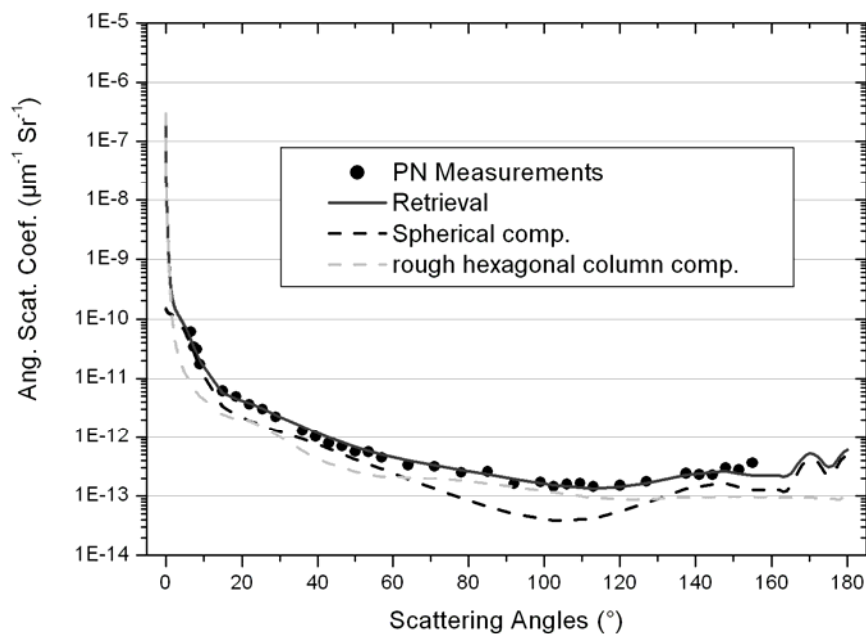


Figure 6.9: Retrieved angular scattering coefficients at the Polar Nephelometer nominal wavelength (800 nm). The PN data were averaged over 4 minutes. Contributions of both components (ice spheres, and ice columns) on the cloud total scattering properties are also displayed. Provided by Olivier Jourdan.

The model of surface roughness used in this study is based on the Weibull statistics (Dodson, 1994) and was already proposed by Shcherbakov et al. (2006). This approach incorporates the Cox and Munk model used by Yang and Liou (1998). Surface roughness can substantially affect the scattering properties of a particle if the geometric scale of the roughness is not much smaller than the incident wavelength. In the case of radiation scattered by large ice crystals (i.e. for size parameters within the geometric optics regime), surface roughness can reduce or smooth out the scattering peaks in the phase function that correspond to halos. For the deeply rough case the computed phase function is essentially featureless. The 22° and 46° halos linked to the hexagonal geometry of ice crystal are smoothed out and the backscattering is substantially reduced because of the spreading of the collimated beams. A roughness scale parameter $\sigma_s = 0.25$ was chosen, which is according to the Improved Geometric Optics Model (IGOM) considered as deeply rough.

In this case study, all the possible combinations of the habits listed above were tested. The best fit of the measurements was achieved using a combination of ice spheres with diameters ranging from $1 \mu\text{m}$ to $100 \mu\text{m}$ and deeply rough hexagonal columns (with an aspect ratio of 2) with maximum dimension ranging from $20 \mu\text{m}$ to $900 \mu\text{m}$. This model gives the minimum root mean square deviation (15 %) compared with the measured ASC.

Since the inverse problem is ill posed for one specific combination of ice crystal geometry, different size distributions can be retrieved. This is accounted for in the estimation of the lidar ratio and the bulk microphysical parameters. The scattering phase function of spherical ice crystals was simulated from Lorentz-Mie theory, and the scattering patterns of rough hexagonal column crystals randomly oriented in 3D space were computed by the Improved Geometric Optics Model (Yang and Liou, 1996). The bulk microphysical (number concentration, IWC, effective diameter) and optical parameters (volume extinction, extrapolated scattering phase function at 532 nm and lidar ratio) were assessed following the method presented by Jourdan et al. (2003b). On the basis of the two particle size distributions,

Table 6.1: Total retrieved bulk microphysical and single scattering properties from PN measurements and contribution of both components. Provided by Olivier Jourdan.

Retrieved Parameters	Spherical ice component	Hexagonal columns component	Total (Spheres + columns)
Concentration (cm^{-3})	0.233	0.002	0.235
TWC (mg m^{-3})	0.009	0.266	0.275
D_{eff} (μm)	4.5	105.8	60.9
Extinction (km^{-1})	0.008	0.009	0.017
Single Scattering Albedo	1.0000	0.9999	0.9999
Asymmetry, g	0.8007	0.7991	0.7998
Lidar Ratio (sr) (800 nm)	17.2	64.5	27.4
Lidar Ratio (sr) (532 nm)	16.3	67.4	27.2

the extrapolated ASC in the forward and backward directions at the lidar wavelength (532nm) as well as the extinction coefficient were calculated. This step was performed using direct modeling of light scattering corresponding to the retrieved PSD. Therefore, access to both terms needed for the lidar ratio computation, namely the scattering coefficient at 180° and the extinction coefficient at 532 nm, was possible. From this method a LR of 27 sr with 25 % error was estimated.

The retrieved ASC from the inversion scheme along with direct PN measurements averaged over 4 minutes are displayed in Fig. 6.9. The measured ASC are flat at the side scattering angles, which is in accordance with most of the observations (Francis et al., 1999; Shcherbakov et al., 2005; Gayet et al., 2006; Jourdan et al., 2003b) or directions in ice cloud remote sensing application (see among others Labonnote et al., 2001, Baran and Labonnote, 2006, 2008, Baran and Francis, 2004). Scattering phase functions of non-spherical ice crystals mostly exhibit enhanced sideward scattering compared to spherical water droplets. Fig. 6.9 highlights that the retrieved ASC are in good agreement with PN direct measurements. The scattering contribution of each microphysical component (dashed lines in Fig. 6.9) points out that the hexagonal ice crystal component reproduces the general flat behavior of the measured ASC at side scattering angles. However, a small ice sphere component is needed to model the relatively higher scattering in the angular range $[15^\circ-60^\circ]$ and $[130^\circ-155^\circ]$ in comparison with hexagonal shape assumption.

The comparison of the model with direct microphysical measurements is limited in this case study, as only four single ice crystal were recorded by the CPI and no statistically significant measurements were performed by the FSSP-100. However, the CPI images (Fig. 6.6) suggest the presence of rounded edge column ice crystals with an average length of 100-200 μm . This observation supports the choice of a rough column component in the microphysical model. Additionally, as shown in Table 6.1, the retrieved effective diameter and number concentration of the hexagonal ice crystal component are acceptable compared to the measurements (effective diameter of 106 μm and very low concentration of 0.002 cm^{-3}). As mentioned above, a small spherical ice component is needed in order to fit the measured ASC. The only information derived from direct measurements that could confirm the presence of small ice crystals is linked to the minimum detection threshold of the CPI and FSSP-100 instruments. The CPI is not able to detect particles with sizes lower than 10 μm (Lawson et al., 2001) and the FSSP-100 minimum measurable concentration is around 0.2 cm^{-3} . The microphysical retrievals are in agreement with the instruments' shortcomings, as the estimated total number concentration of the ice cloud is 0.2 cm^{-3} and the effective diameter of the small ice crystals is 4.5 μm .

In conclusion, a microphysical model composed of small spherical ice particles and larger deeply rough hexagonal column crystals leads to optical and, to a certain extent,

microphysical properties (asymmetry parameter, extinction and ASC), which allows to reproduce the measurements. On that basis, the microphysical model corresponding ASC for a wavelength of 532 nm is computed in order to derive the ice cloud mean lidar ratio. The assessed lidar ratio is $27 (\pm 7)$ sr with the relative error of 25 % accounting for instrumental errors and the extrapolation technique. This value is in reasonable agreement with other values obtained for cirrus clouds (Chen et al., 2002, Cadet et al., 2005, Giannakaki et al., 2007).

The low asymmetry parameter (~ 0.78) of the PN measurements is consistent with the enhanced depolarization measurements of up to 40 % and the CPI images indicating non-spherical ice crystals. It is not possible to distinguish the particle shape from the values of lidar depolarization measurements, not even for clouds composed entirely of one kind of ice particle habits, as was evidenced by Monte Carlo simulations of You et al. (2006). Most of the asymmetry parameter values fall within the range that is typical of cirrus clouds shown by Gayet et al. (2006), i.e., a cloud containing ice particles was sampled.

The extinction coefficients retrieved from the PN range between the lidar values (Sect. 6.2.2) but could not exhibit the maximum of 0.1 km^{-1} measured by the lidar. This suggests that the aircraft was not within the densest part of the cloud during the in situ measurements, or the cloud generally was in the process of dissolving. The values of RHI around saturation and the round edges of the ice crystals confirm that dissolving processes were taking place in the cloud. The extinction coefficients are much below the typical values of midlatitude cirrus as presented in Gayet et al. (2006). This clearly indicates that a subvisible midlevel ice cloud was probed.

6.3.2 Simulation of the measured radiation

The measured I_{λ}^{\downarrow} was employed to retrieve the optical thickness of the observed cloud. For this purpose, radiative transfer simulations were performed by André Ehrlich with the Library for Radiative Transfer (libRadtran) package (Mayer and Kylling, 2005). It calculates the radiation field for user-specified atmospheric and surface conditions. The model wavelength range of 300-2100 nm was adapted to the spectral resolution of the SMART-Albedometer. The meteorological input (profiles of air pressure, temperature and relative humidity) was obtained from radio sounding at Ny-Ålesund (10 April 2007, 11:00 UTC). Above 33 km altitude a subarctic winter profile (Anderson et al., 1986) was used. The aerosol microphysical properties were taken from Shettle (1989). The spring-summer maritime aerosol profile was chosen for the boundary layer, background aerosol conditions were applied for the altitudes above. The aerosol optical depth applied to the simulations was scaled by the Ångström formula with an Ångström exponent of $\alpha = 1.51$ and an aerosol optical thickness at $1 \mu\text{m}$ wavelength of $\tau = 0.03$. Both coefficients were obtained from sun photometer measurements at Ny-Ålesund on 7 April 2007 using a SP1A sun photometer (Herber et al., 2002). For gas absorption the parameterization by Ricchiazzi et al. (1998) was used. To solve the radiative transfer equation, which describes the attenuation of direct solar radiation in the atmosphere, the discrete ordinate solver DISORT version 2.0 by Stamnes et al. (1988) was applied. It uses one-dimensional plane-parallel geometry assuming a horizontally homogeneous atmosphere, and provides the radiation quantities radiance and irradiance at arbitrary altitudes. The simulated values were then compared to the measured radiation, and the cloud optical thickness of the model was varied to obtain the best agreement of measured and modeled radiation.

First the cloud free situation (11:50-11:52 UTC) was simulated, and then the subvisible midlevel ice cloud was included in order to match the observations between 11:53 and 12:00

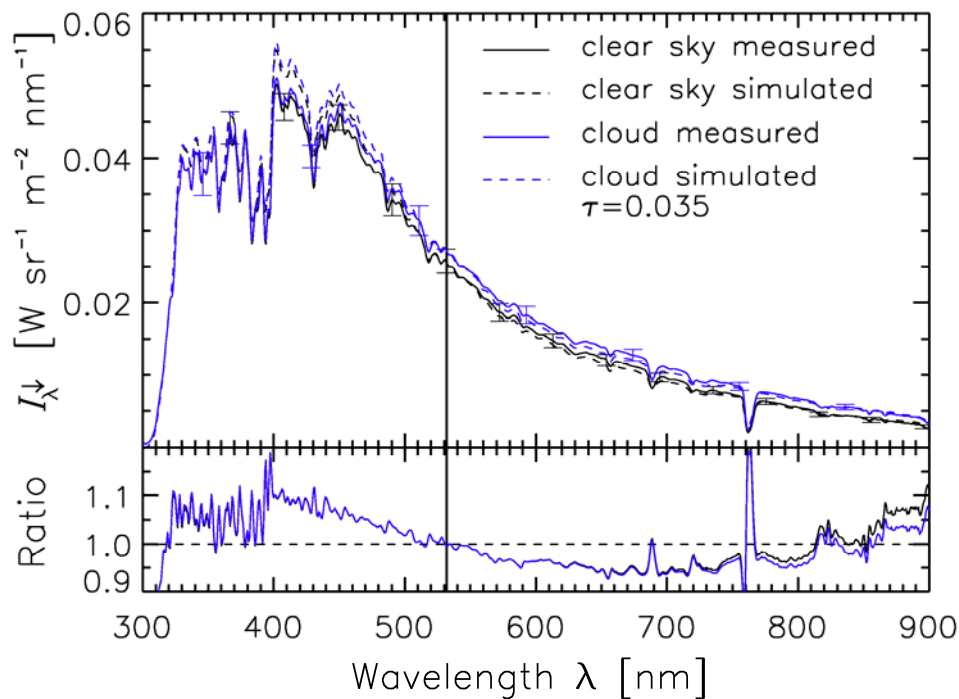


Figure 6.10, top: Spectral downwelling radiance I_{λ}^{\downarrow} simulated (dashed lines) and measured (solid lines) by the SMART-Albedometer for clear sky conditions (black lines, 11:50-11:52) and the observed optically thin midlevel ice cloud (blue lines, 11:57-11:59 UTC). The measured and simulated data are averaged over two minutes (sequence of the thin cloud indicated by vertical lines in the time series of Fig. 6.11). Bottom: Ratio of simulated and measured downwelling radiance for the clear sky and cloudy case. Provided by André Ehrlich.

UTC. To accurately reproduce the clear sky downwelling radiance, measured before the subvisible cloud appeared above the aircraft, a cirrus cloud at 6500-7000 m altitude, approaching from the South and later also detected by the lidar, had to be considered. During the first part, the cirrus was not directly above the aircraft but already in front of the sun affecting the diffuse radiation. The cirrus optical depth $\tau = 0.04$ and effective radius $R_{\text{eff}} = 60 \mu\text{m}$ were estimated as best fit to the measured clear sky radiance and included in the simulations by using the parameterization of Key et al. (2002) assuming solid column ice crystals. The spectral downwelling radiance of clear sky simulations and measurements shown in Fig. 6.10 (black lines) are in good agreement especially for the wavelength range between 500 nm and 600 nm, including the 532 nm channel (vertical bar) of AMALi.

In a second step, the subvisible cloud at an altitude of 2500-3000 m was included in the simulations. The scattering phase function and single-scattering albedo derived from the PN measurements (Sect. 6.3.1) were employed. The simulations for a solar zenith angle of 70° , present during the measurements, were found to be almost insensitive against the assumed scattering phase function, because for this scattering angle, the scattering phase function shows almost the same values for different shapes of ice crystals (see Fig. 6.9). Therefore the simulations are most sensitive to the cloud optical thickness τ . By variation of τ , the simulations were modified in order to fit the measurements of I_{λ}^{\downarrow} below the cloud. The spectral downwelling radiance simulated below the subvisible cloud is shown in Fig. 6.10 as blue line. From this method an optical thickness of 0.048 was obtained for the time interval between 11:53 and 12:00 UTC. The comparison with AMALi results is discussed in Sect. 6.3.3.3. The mean spectral downwelling radiance shown as dashed line in Fig. 6.10 agrees well with the simulation.

The ratio of simulated and measured downwelling radiance ranges between $\pm 10\%$ for most wavelengths (Fig. 6.10, lower panel). As the simulations were fitted by varying the cloud optical depth, the best agreement was found at 532 nm wavelength. The deviations at other wavelengths result from a) measurement uncertainties of the spectrometer and b) the aerosol optical depth assumed for the radiative transfer simulations. As the airborne measurements were conducted about 370 km away from Ny-Ålesund, a different aerosol optical thickness may have been present in the vicinity of the subvisible cloud. However, as Figure 6.10 shows, the ratio of measurements and simulations is similar for the cloud free and cloudy case. This implies that variations in the SMART-Albedometer data (cloud free, cloudy) result only from changes of the cloud properties and not from aerosol properties of the low aerosol load. The scattering properties of cloud particles in the visible wavelength range are almost independent of the wavelength, whereas aerosol scattering decreases exponentially with a power law with increasing wavelength in this wavelength range (Chapt. 3).

Although the differences between clear sky and cloud covered case were low, the simulations showed that the radiative effects of the optically thin cloud were detectable by the radiance measurements.

6.3.3 Lidar ratio

The lidar ratio is crucial for determining the extinction coefficient and the cloud optical depth τ from lidar measurements (Chapt. 3). As the two parameters are proportional to the lidar ratio, they are strongly influenced by the error of the lidar ratio. Therefore, three independent methods of determining the lidar ratio are applied and compared in the following.

6.3.3.1 PN measurements

On the basis of the microphysical model described in Sect. 6.3.1, the corresponding ASC for a wavelength of 532 nm was computed in order to derive the ice cloud mean lidar ratio. The extrapolated scattering phase function of the PN delivered relatively high lidar ratios, depending on the assumed particle shape. The best agreement of the model and the measured extrapolated scattering phase function was obtained with a lidar ratio of 27 (± 7) sr. This resulted from fitting a mixture of small ice spheres, and deeply rough hexagonal columns with an aspect ratio of 2 to the scattering phase function. The relative error of 25 % accounts for instrumental errors and extrapolation technique (Jourdan et al., 2003a).

6.3.3.2 Transmittance method

Another independent approach to determine the effective lidar ratio is the transmittance method (see Chapt. 3). From the elastic lidar profiles at the wavelength $\lambda = 532$ nm, the lidar ratio was estimated. As the cloud was located at an altitude in the free troposphere on a day without pollution (indicated by the clear sky values of optical depth measured with the lidar directly before the cloud), the assumption of the same backscattering ratio below and above the cloud is justified.

With the method described in Chapt. 3, single values and their error bars were retrieved for the *LR* with a horizontal resolution of 930 m between 11:54 and 12:00 UTC. Due to the small cloud optical depth, the results are not influenced by multiple scattering. The mean effective value for the *LR* of the cloud was found to be 15 (± 10) sr.

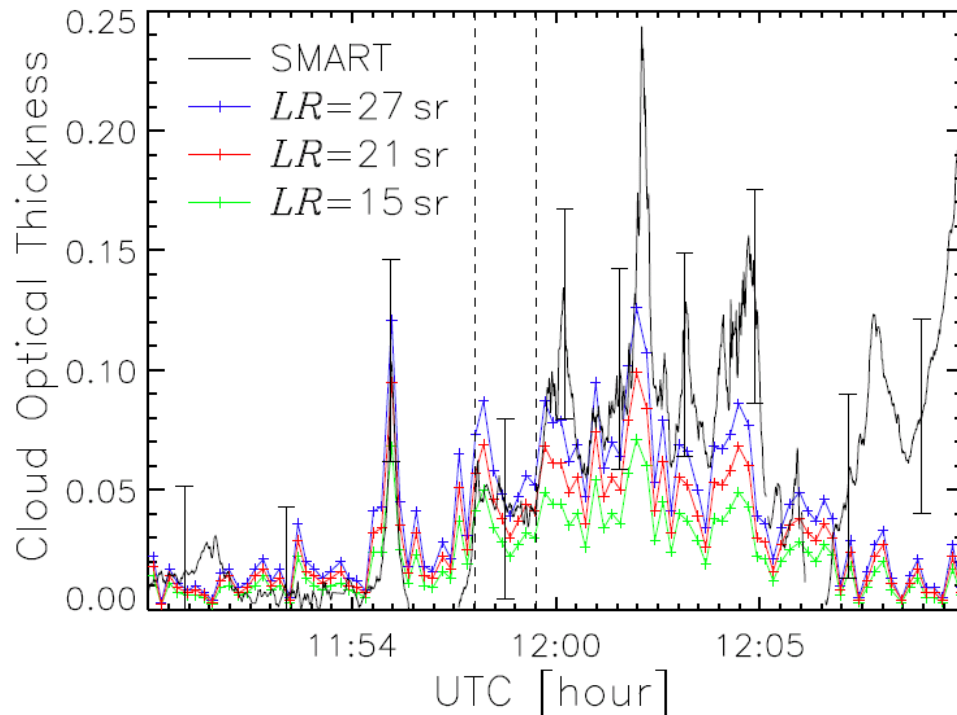


Figure 6.11: Time series of cloud optical thickness determined from SMART-Albedometer measurements (black line) and from lidar data for different values of the lidar ratio (27, 21 and 15 sr, colored lines). The error bars at exemplary time steps display the uncertainty of the albedometer retrieval. The vertical bars indicate the time interval over which the measured and simulated values were averaged for the spectra shown in Fig. 6.10. After 12:00 UTC, an additional cirrus cloud at 6 km altitude caused the discrepancies of the albedometer and lidar cloud optical thickness. Provided by André Ehrlich.

6.3.3.3 Combination of lidar and radiation measurements

From SMART-Albedometer measurements, a time series of the cloud optical depth was retrieved for the lidar wavelength of 532 nm. For this purpose, the method described in Sect. 6.2.3 was applied. Lookup tables were calculated for the downwelling radiance $I_{532\text{nm}}^{\downarrow}$ assuming a cloud optical thickness in the range of 0-0.5. For each measurement of the SMART-Albedometer, an appropriate value of τ was derived by interpolating the lookup tables' values to the measured $I_{532\text{nm}}^{\downarrow}$. Fig. 6.11 shows the time series of τ retrieved from $I_{532\text{nm}}^{\downarrow}$. In addition, the cloud optical thicknesses derived from AMALi assuming three different LR (PN measurements $LR = 27$ sr, mean value $LR = 21$ sr, transmittance method $LR = 15$ sr) are given. The derived τ agree within the uncertainty range of τ retrieved from the SMART-Albedometer until 11:59 UTC. After 12:00 UTC the cirrus cloud was above the aircraft increasing the measured radiance. Therefore, τ retrieved from the SMART-Albedometer overestimates the optical thickness of the subvisible cloud. Assuming that single scattering (at a scattering angle of 70°) is dominating the radiative transfer through the subvisible cloud, τ is obtained independently of the ice crystal scattering phase function (and LR). The retrieved τ are used in combination with the AMALi measurements to derive an independent estimate of the LR . By dividing τ by the corresponding integral of the particle backscatter coefficient, the LR is calculated. For the time when the cloud was detected without cirrus above, and omitting the cloud free section around 11:57 UTC, this method resulted in an effective LR of $20 (\pm 10)$ sr.

Table 6.2: Lidar ratio of the thin ice cloud retrieved from different data sets.

retrieval	PN	lidar	albedometer / lidar	overall
<i>LR</i> (sr)	27 ± 7	15 ± 10	20 ± 10	21 ± 6

6.3.3.4 Comparison

In summary, the effective lidar ratio and its accuracy were determined by three independent methods (evaluation of PN data, transmittance method applied to lidar data, and combination of cloud optical thickness derived from albedometer and integrated lidar backscatter, Table 6.2). A *LR* of $27 (\pm 7)$ sr was obtained from the PN data, $15 (\pm 10)$ sr from the transmittance method, and $20 (\pm 10)$ sr from the combined albedometer and lidar data. The disagreement of the value derived from PN can be explained by the temporal delay between the in situ and remote sensing measurements. However, the mean lidar ratio was calculated from these three values by error propagation. It amounts to 21 sr. The error bar was estimated according to the following considerations: A lidar ratio in the range of 20 to 25 sr is within the error bars of all measurements. The mean values of the *LR* obtained by the in situ retrieval and the transmittance method were also included in the range of the *LR*. Therefore, $21 (\pm 6)$ sr is proposed as an overall lidar ratio for the cloud. This value is in reasonable agreement with other *LR* values for cirrus clouds in the literature (Ansmann et al., 1992, Chen et al., 2002, Cadet et al., 2005, Giannakaki et al., 2007). For CALIOP data evaluation, a lidar ratio of 25 sr is used for cirrus clouds (Sassen and Comstock, 2001).

6.3.4 Cloud radiative forcing

Broadband solar and infrared, downwelling and upwelling irradiance ($F_{S\downarrow}$, $F_{S\uparrow}$, $F_{IR\downarrow}$, $F_{IR\uparrow}$) were calculated by André Ehrlich with radiative transfer simulations at aircraft altitude (160 m) for two cases. First, the observed situation including the subvisible midlevel ice cloud and the cirrus cloud above (case 1) was simulated using the input parameters as described in Section 6.3.2. The net solar irradiance $F_S^{\text{net}} = F_{S\downarrow} - F_{S\uparrow}$ was found to be $F_S^{\text{net}} = 155.5 \text{ W m}^{-2}$, the net thermal infrared irradiance $F_{IR}^{\text{net}} = F_{IR\downarrow} - F_{IR\uparrow} = -85.6 \text{ W m}^{-2}$. To estimate the radiative forcing of the subvisible midlevel ice cloud, a second simulation including only the cirrus cloud was evaluated (case 2). Without the midlevel ice cloud, the net solar irradiance increases to $F_S^{\text{net}} = 158.7 \text{ W m}^{-2}$, while the net thermal infrared irradiance is reduced to $F_{IR}^{\text{net}} = -88.4 \text{ W m}^{-2}$ (Table 6.3). The solar radiative forcing of the subvisible midlevel ice cloud (case 1 minus case 2) of -3.2 W m^{-2} indicates enhanced reflection of solar radiation due to the subvisible cloud and therefore additional surface cooling. On the other hand, the subvisible cloud's emission of infrared radiation led to enhanced surface warming in the range of 2.8 W m^{-2} (thermal infrared forcing of the midlevel ice cloud). Therefore, the net effect of the cloud on the local radiation budget was a slight cooling effect of -0.4 W m^{-2} . On a local scale in which the subvisible cloud was observed, this cooling is almost negligible.

The small net radiative effect estimated from the radiative transfer simulations was detected by the radiation measurements only in certain limits. The solar irradiance measurements did not show any response to the subvisible midlevel ice cloud. The measurement uncertainty of 4 % exceeds the estimated changes in $F_{S\downarrow}$ and $F_{S\uparrow}$ (2% change).

Table 6.3: Modeled downwelling and upwelling irradiance and net fluxes in the solar and thermal infrared wavelength range. Provided by André Ehrlich.

		Clear Sky	Thin cloud	Forcing
Solar	$F_{S\downarrow}$ [W m^{-2}]	351.7	345.8	
	$F_{S\uparrow}$ [W m^{-2}]	193.0	190.2	
	F_S^{net} [W m^{-2}]	158.7	155.5	-3.2
Thermal IR	$F_{\text{IR}\downarrow}$ [W m^{-2}]	184.7	187.5	
	$F_{\text{IR}\uparrow}$ [W m^{-2}]	273.1	273.1	
	$F_{\text{IR}}^{\text{net}}$ [W m^{-2}]	-88.4	-85.6	+2.8

The increased downwelling thermal infrared radiation related to the presence of the optically thin cloud was observed by the pyrgeometer, which showed an increase from 172 W m^{-2} to 176 W m^{-2} . The magnitude of the change is consistent with the simulations, which calculated an increase from 184.7 W m^{-2} to 187.6 W m^{-2} . The disagreement of the absolute values can be attributed to the reasons given in Sect. 5.3.

6.4 Interpretation: Implication for the Arctic radiation budget

Although the forcing of the subvisible midlevel ice cloud of -0.4 W m^{-2} is generally negligible, especially on a local scale, under night time conditions without solar forcing, the net surface warming effect of about 2.8 W m^{-2} is considerable.

Compared to Arctic aerosol layers, the radiative effects of optically thin Arctic clouds are often in the same order of magnitude (Blanchet and List, 1983, Rinke et al., 2004), but sometimes with the opposite sign. Arctic haze, often occurring at the same altitudes as the midlevel ice cloud analyzed here (Scheuer et al., 2003), is generally warming the atmosphere because of its absorption characteristics (Blanchet and List, 1983). A further effect of subvisible midlevel ice clouds in the free troposphere might be the interaction with aerosols. Here, the aerosols may act as ice condensation nuclei and the cloud as a sink for aerosols. The study of Jiang et al. (2000) shows that the existence of Arctic mixed-phase clouds is very sensitive to the concentration of ice forming nuclei. It is likely that similar interactions take place with midlevel subvisible clouds. More investigations are necessary to confirm and quantify these possible implications.

Compared to cirrus clouds at higher altitudes with a similar optical depth, the optically thin midlevel ice cloud of this study shows a generally higher IR forcing due to the higher temperatures at lower altitudes. Thus, midlevel Arctic ice clouds tend to cool the surface temperatures less than higher ice clouds with comparable optical properties in the solar wavelength range.

The repeated occurrence of atmospheric conditions favorable for the formation of optically thin midlevel Arctic ice clouds is suggested by the CALIOP observation of a similar thin cloud in the same region one day later on 11 April 2007. This emphasizes the relevance of this cloud type for the Arctic radiative budget.

For the time period of the ASTAR 2007 campaign (26 March to 16 April 2007), the data of 113 overpasses of the CALIOP lidar were available for the geographical location around Svalbard ($0\text{-}30^\circ \text{ E}$, $75\text{-}82^\circ \text{ N}$). In 62 of these cases, clouds were found in the altitude range of 2500 m to 3500 m, which were optically thin enough that the lidar signal was not completely attenuated but penetrated to the ground. Cases with boundary layer clouds beneath were not considered. Although this is only a very rough estimate, it underlines the possible importance of thin midlevel clouds. Even if these clouds have a small effect on the radiation budget as for

the case presented here, their existence could be important in the Arctic winter, when the thermal warming effect is not balanced by the cooling influence in the solar wavelength range.

7 Airborne observations of Arctic mixed-phase clouds

In this chapter, lidar investigations of Arctic mixed-phase clouds during the ASTAR 2007 campaign are presented. Parts of the results are published in Richter et al. (2008) and Lampert et al. (2009b).

7.1 Cloud statistics at Ny-Ålesund during ASTAR 2007

As an overview of the cloud situation during ASTAR 2007, micro pulse lidar data were analyzed. For the statistics of cloud base and cloud top height, the MPL data from 15 March until 30 April 2007 was analyzed. First, the data was averaged to means of 10 min and background corrected. From the obtained profiles the backscattering ratio was calculated with the Klett algorithm (Sect. 3.2.2).

Using different thresholds for the difference between two adjacent BSR values (high values above 0.1 increasing for at least 3 height steps or a single peak difference of at least 0.2 to 0.3 if no lower clouds were detected), the BSR was analyzed for cloud peak structures in five distinct altitude intervals: 0-300 m (snow on the window), 300-1200 m (boundary layer clouds), 1200-2500 m (low clouds), 2500-5500 m (midlevel clouds) and 5500-10000 m (high clouds). If none of these were detected the profile was set to 'cloud free'. The cloud categories take into account the frequent occurrence of a temperature inversion at around 1200 m and 2500 m observed by radio sounding in Ny-Ålesund, which is influenced by local orography. The upper boundary of midlevel clouds follows the definition of Pinto et al. (2001).

Since the signal to noise ratio above a cloud structure can decrease dramatically, the peak threshold conditions were adjusted accordingly (e.g. a SNR below 3 between 7500 m and 10000 m and the detection of no clouds give evidence that there was snow on the window instead of a cloud free atmosphere). Depending on the optical thickness of the lower clouds, the data about the occurrence of higher clouds have to be considered as less reliable. The MPL does not provide information on depolarization, and thus the thermodynamic phase of clouds.

The main finding was that the occurrence of boundary layer clouds and low clouds increased through the analyzed time period from 51 % to 65 %. The boundary layer cloud occurrence even increased from about 36 % in the second half of March to 59 % in the second half of April, while the clear sky fraction remained roughly constant at about 25 % to 33 %. In Fig. 7.1, the percentages refer to the respective time periods with a snow free window.

As cloudiness in the Arctic increases with sunlit season (Key et al., 2004), a strong increase in low-level cloud cover is generally observed during the transition period spring. The results of cloud occurrence for spring 2007 in Ny-Ålesund are similar to the MPL observations of March and April 2002 (Shiobara et al., 2003). In 2001, the existence of low-level clouds (0-2000 m altitude), measured with ceilometer, increased from 30 % in March to 50 % in April (Kupfer et al., 2006). The MPL cloud statistics of ASTAR 2007 indicate that the typical atmospheric conditions of Arctic spring were present from a cloud point of view. This is of special interest as the Arctic haze phenomenon with enhanced tropospheric aerosol load was not pronounced during the ASTAR 2007 time period (Hoffmann et al., 2009). Arctic haze, observed regularly at Ny-Ålesund by sun photometer (Herber et al., 2002) and lidar (Ritter et al., 2004) in spring time, occurs often at altitudes below 3000 m (Scheuer et al., 2003) and provides cloud condensation nuclei for cloud formation. Despite the absence of Arctic haze, the increase in low level cloudiness was observed. However, even under clean conditions,

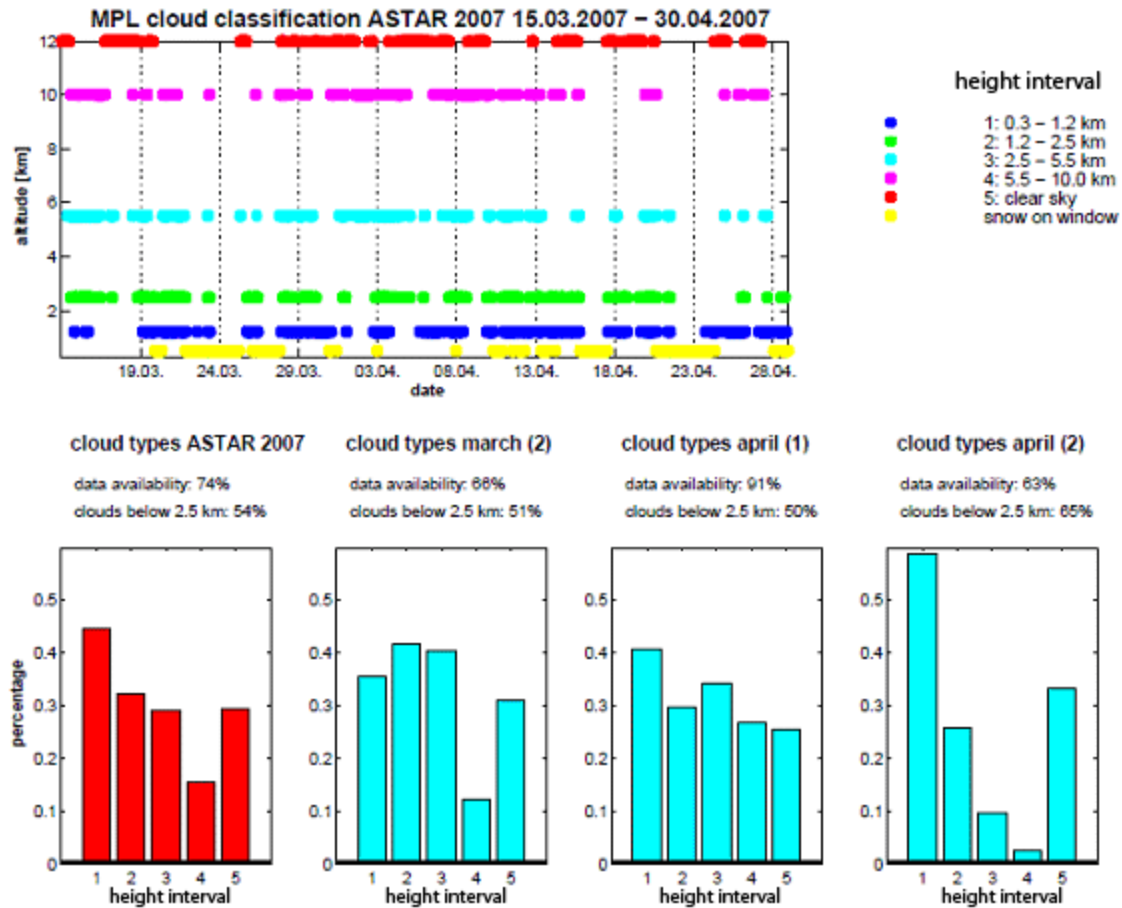


Figure 7.1: Occurrence and height distribution of clouds from 15 March to 30 April 2007, observed by MPL (top). Percentage of cloud cover for different height intervals for the whole time period, and divided into periods of 2 weeks. Provided by Anne Hoffmann.

particles in the accumulation mode are found in Svalbard throughout fall to spring (e.g. Ström et al., 2003). They are subject to long-range transport and persevere sometimes over months in the Arctic atmosphere (Ström et al., 2003). Also sea salt particles of local origin serve as cloud condensation nuclei. The thawing of sea ice, the increased solar radiation and atmospheric temperatures in spring lead to more water vapor in the atmosphere available for cloud formation.

7.2 Boundary layer clouds

The aim of the research flight on 8 April 2007 was to investigate the properties of boundary layer clouds forming in a cold air outbreak west of Svalbard. Along the flight track, nearly perpendicular to the longitudinal convective cloud streets, the clouds were probed by deploying the in situ instrumentation. Along the same flight track backward, simultaneous remote sensing measurements with lidar and solar radiation sensors were performed at an altitude of 2730 m.

The flight on 9 April was planned as a contribution to the CALIPSO and CloudSat satellite validation. The Polar-2 followed the footprint of the satellite track above the open ocean towards North-West nearly synchronously, at an altitude of 2760 m. Lidar observations were performed during this first part of the flight from 08:36 to 09:25 UTC. Reaching the predefined northernmost waypoint, the aircraft turned and flew back the same path

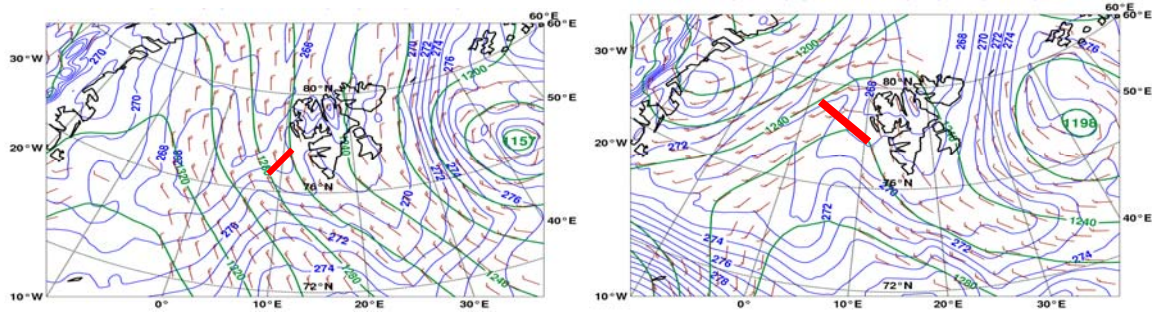


Figure 7.2: Geopotential height (m, green lines), equivalent potential temperature (K, blue lines) and wind speed (ms^{-1} , barbs) at 850 hPa on 8 April (left) and 9 April 2007 (right) at 12:00 UTC. The approximate locations of the flight paths are indicated by red lines. Meteorological data are taken from operational ECMWF analyses. Provided by Andreas Dörnbrack.

descending and ascending from cloud top to cloud bottom deploying the in situ sensors. The profile measurements were performed within the clouds from 09:50 to 10:44 UTC. The actual coincidence with the CALIPSO satellite overpass occurred on the way back during the in situ measurements at 10:06 UTC. The flight tracks are indicated as red lines in the synoptic analyses (Fig. 7.2).

In the following, the cloud properties of the two cases, observed with lidar, albedometer and in situ instruments, are analyzed in the context of the synoptic situation (7.2.1). The thermodynamic cloud phase derived from the lidar measurements is evaluated with albedometer and in situ data (7.2.2). A comparison of the airborne and space borne lidar measurements is presented (7.2.3). The EMCWF analyses of cloud condensate and the partitioning of liquid and ice water is evaluated with the airborne lidar and in situ observations (7.2.4).

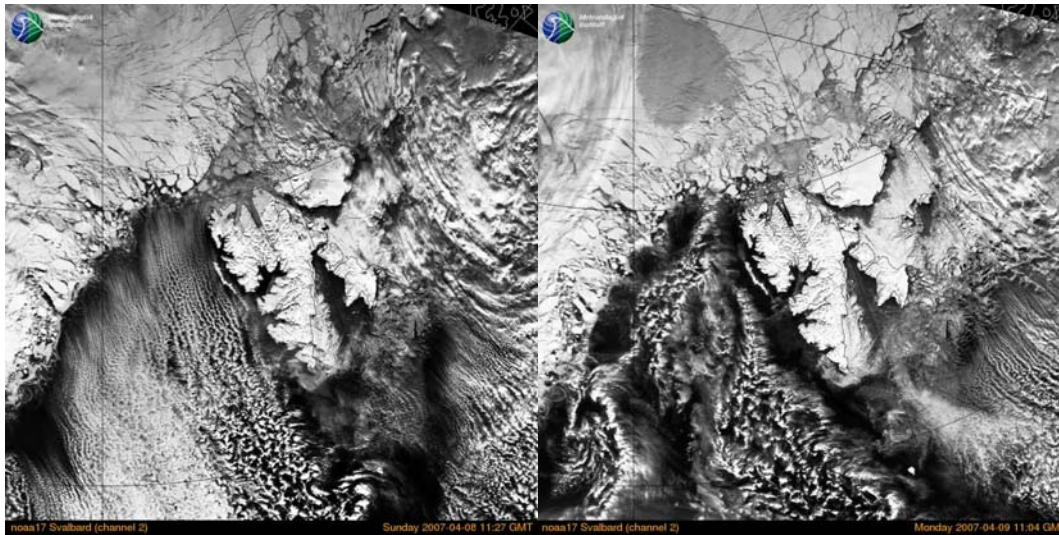


Figure 7.3: NOAA visible satellite imagery on 8 April 2007 11:27 UTC (left) and 9 April 2007 11:04 UTC (right). Courtesy of the Norwegian Meteorological Institute, Tromsø, Norway.

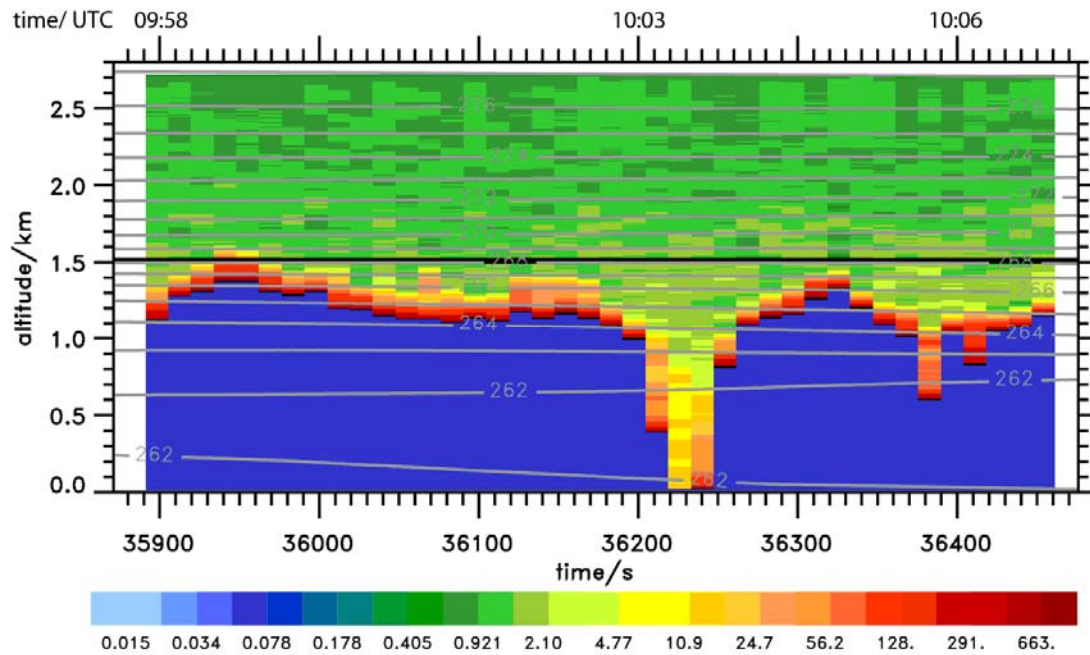


Figure 7.4: Nadir measurements of lidar backscattering ratio (color shaded) along the flight track on 8 April 2007. Areas of dark blue cannot be evaluated as the lidar signal does not penetrate the clouds. The potential temperature (K, grey lines) is interpolated in time and space on the flight track. The straight black line indicates the boundary layer height (see text). Meteorological data are taken from operational ECMWF analyses provided by Andreas Dörnbrack.

7.2.1 Synoptic situation and cloud structure

On the back of a slowly north-eastward propagating trough, cold air was ejected from higher latitudes towards Svalbard on 8 April 2007 (Fig. 7.2, left). This cold-air outbreak was associated with convective cloud streets forming south of the ice edge and extending far south (Fig. 7.3, left). The synoptic situation favored the formation of boundary layer mixed-phase clouds. On 9 April 2007, a ridge built up west of Svalbard and disrupted the cold air outflow. After the passage of the ridge axis, warmer and moister tropospheric air from the South replaced the cold air masses from the North (Fig. 7.2, right). The meteorological situation along the flight track consequently revealed the existence of two different air masses: convective cloud streets and northerly flow with low temperatures were observed in the southern part, and warmer air with scattered clouds in the northern part of the flight track (Fig. 7.3, right).

On 8 April 2007, the time series of lidar backscatter profiles (Fig. 7.4) depicts the cloud top of boundary layer clouds extending up to an altitude of 1600 m. The upper edge of this low-level cloud layer shows wavelike undulations. As the clouds were forming in a cold-air outbreak over the warmer water, it is most likely that these undulations are the signature of convective roll clouds (Houze, 1993). This argument is supported by the low static stability (small buoyancy frequency) in the near adiabatic boundary layer underneath a sharp inversion. The static stability N^2 is defined from the hydrostatic equilibrium of pressure gradient force and gravitational force,

$$N^2 = g_0/\Theta_0 \partial\Theta/\partial z, \quad (7.1)$$

with g_0 the gravitational constant, Θ_0 the potential temperature at ground level, and Θ being the potential temperature.

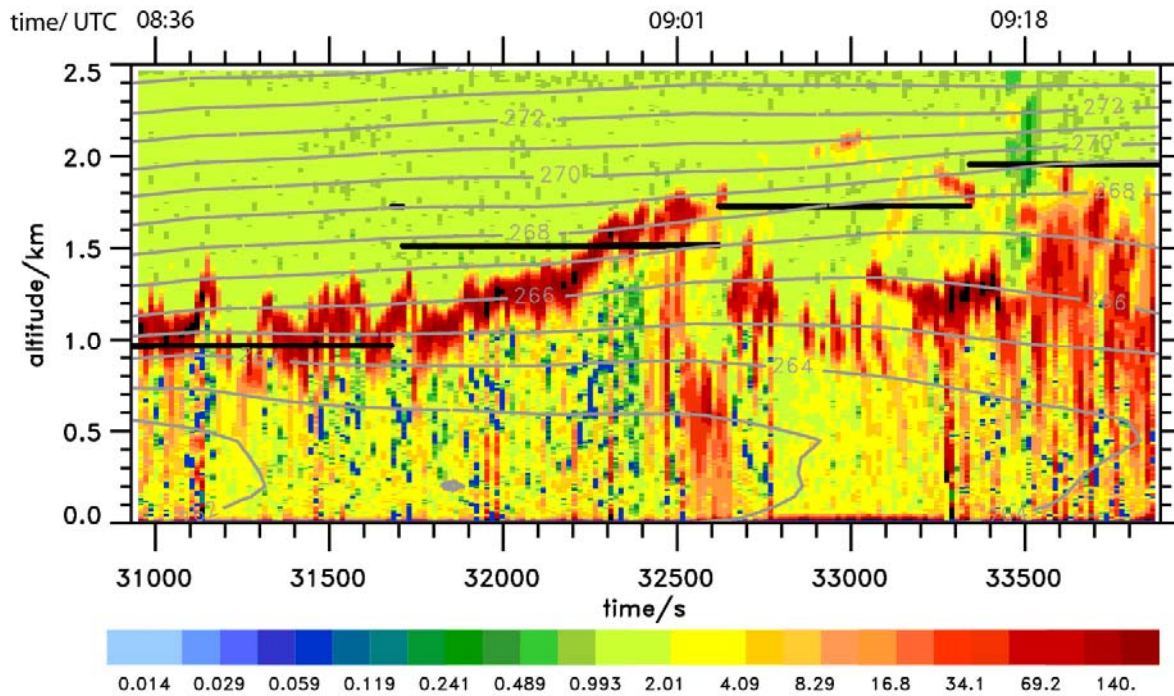


Figure 7.5: Nadir measurements of lidar backscattering ratio (color shaded) along the flight track toward NW on 9 April 2007. Potential temperature (K, grey lines) interpolated in time and space on the flight track. The straight black lines indicate the boundary layer height (see text). Meteorological data are taken from operational ECMWF analyses provided by Andreas Dörnbrack.

The low static stability can be seen by the broadly spaced isentropic surfaces from the operational ECMWF analyses, superimposed to the lidar backscattering ratio (Fig. 7.4). However, the ECMWF analyses cannot resolve the mesoscale features of the convective clouds and give a uniform boundary layer height of about 1500 m. This height was determined as the height of maximum N^2 (inversion) which here coincides with a local maximum of the potential vorticity attaining a nearly stratospheric value of 1.9 PVU (PVU being the potential vorticity unit $10^{-6} \text{ m}^2 \text{ s}^{-1} \text{ K kg}^{-1}$).

The clouds were optically thick and homogeneous, and attenuated the laser pulses. The ground return was not visible, so no information about the cloud geometrical thickness can be given in this case. The cloud optical thickness was estimated from albedometer measurements (see Sect. 5.3) to be in the range of 15 to 20.

On 9 April 2007, the particle backscattering ratio as shown in Fig. 7.5 reveals a gradual increase of the cloud top height along the flight track. This observation agrees with the superimposed isentropic surfaces from ECMWF analyses which indicate an increase of the boundary layer depth along the flight track. Here, the boundary layer height was calculated as the location of maximum buoyancy frequency N^2 or as the minimum altitude where $N > 0.015 \text{ s}^{-1}$. In the time series of lidar backscatter profiles, the two different air masses can clearly be distinguished: During the first part of the lidar flight (08:36–09:01 UTC), a relatively homogeneous boundary layer cloud with high values of the backscattering ratio (exceeding 50) was observed. The optical depth was estimated by albedometer measurements (see Sect. 5.3) as around 13 to 17. Despite the large values of the optical depth, the ground return of the open ocean was visible for most time steps. This may be due to cloud gaps with a size smaller than the horizontal resolution of around 900 m, corresponding to the lidar integration time of 15 s. The laser pulses thus penetrated the clouds, and between the upper cloud boundary and the surface, structures with high backscattering ratio (water layers) were also observed in the lidar signal. However, the detection of the weaker backscatter signal of ice or precipitation

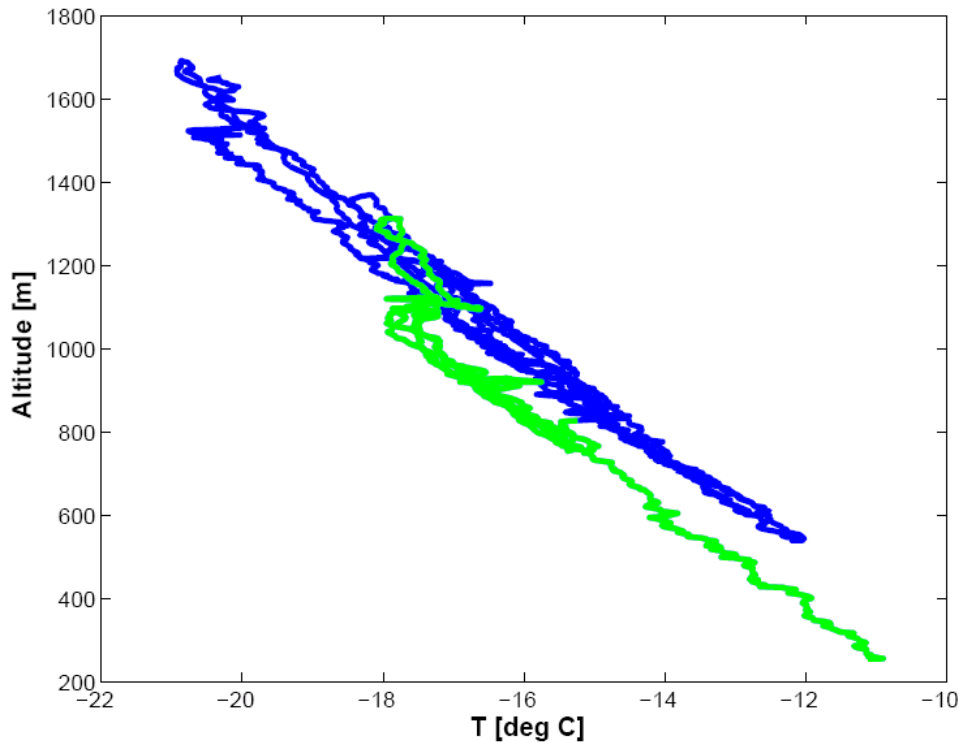


Figure 7.6: Temperature profiles measured on 9 April 2007. Blue are the profiles measured in the North-West, before 10:18 UTC, and green are the profiles measured in the South-East, after 10:18 UTC. Below the altitude of 1100 m, the air temperature is about 1.5 degrees colder in the South-East of the flight leg.

below the water layer is not reliable. In the second part of the lidar flight, after 09:02 UTC (32500 s in Fig. 7.5), the continuous cloud layer broke up and scattered clouds at different altitudes were detected. In contrast to the continuous cloud deck, the lidar signal could penetrate these clouds almost completely throughout their depth for each time step. Precipitation was observed on several occasions.

The observations point to different processes of cloud evolution. In fact, the meteorological analyses reveal that the lidar sampled air masses of different origin: During the first part of the research flight, remnants of the northerly cold-air outbreak were observed, which were gradually replaced by warmer air originating from the South.

The temperature profiles obtained during the in situ measurements are shown in Fig. 7.6. During the first part of the in situ leg in South-East direction (blue color), the temperature amounted to around $-12\text{ }^{\circ}\text{C}$ at the altitude of 550 m, and $-21\text{ }^{\circ}\text{C}$ at 1500 m. After 10:18 UTC, corresponding to the coordinates $78.12\text{ }^{\circ}\text{N}$ and $11.52\text{ }^{\circ}\text{E}$ (green color), the temperature below 1100 m was about $1.5\text{ }^{\circ}\text{C}$ colder.

As the uppermost layer of a cloud has the highest influence on radiative transfer (Ehrlich et al., 2009), it is crucial to determine the geometrical depth of this layer. The information on the geometrical thickness of the uppermost liquid layer could be retrieved from the lidar measurements for 9 April 2007. Even if the ground return was only visible due to local inhomogeneities, i.e. cloud gaps smaller than the horizontal resolution of the lidar profiles, the information is of interest for radiative transfer modeling. The upper liquid cloud layer was defined here as the height interval with (arbitrarily chosen) high backscattering ratio above 30. The mean geometrical thickness of the water layer was $280 (\pm 80)$ m for the relatively homogeneous clouds observed from 08:40 to 09:02. Liquid water was found by lidar observations at altitudes between 900 and 1600 m.

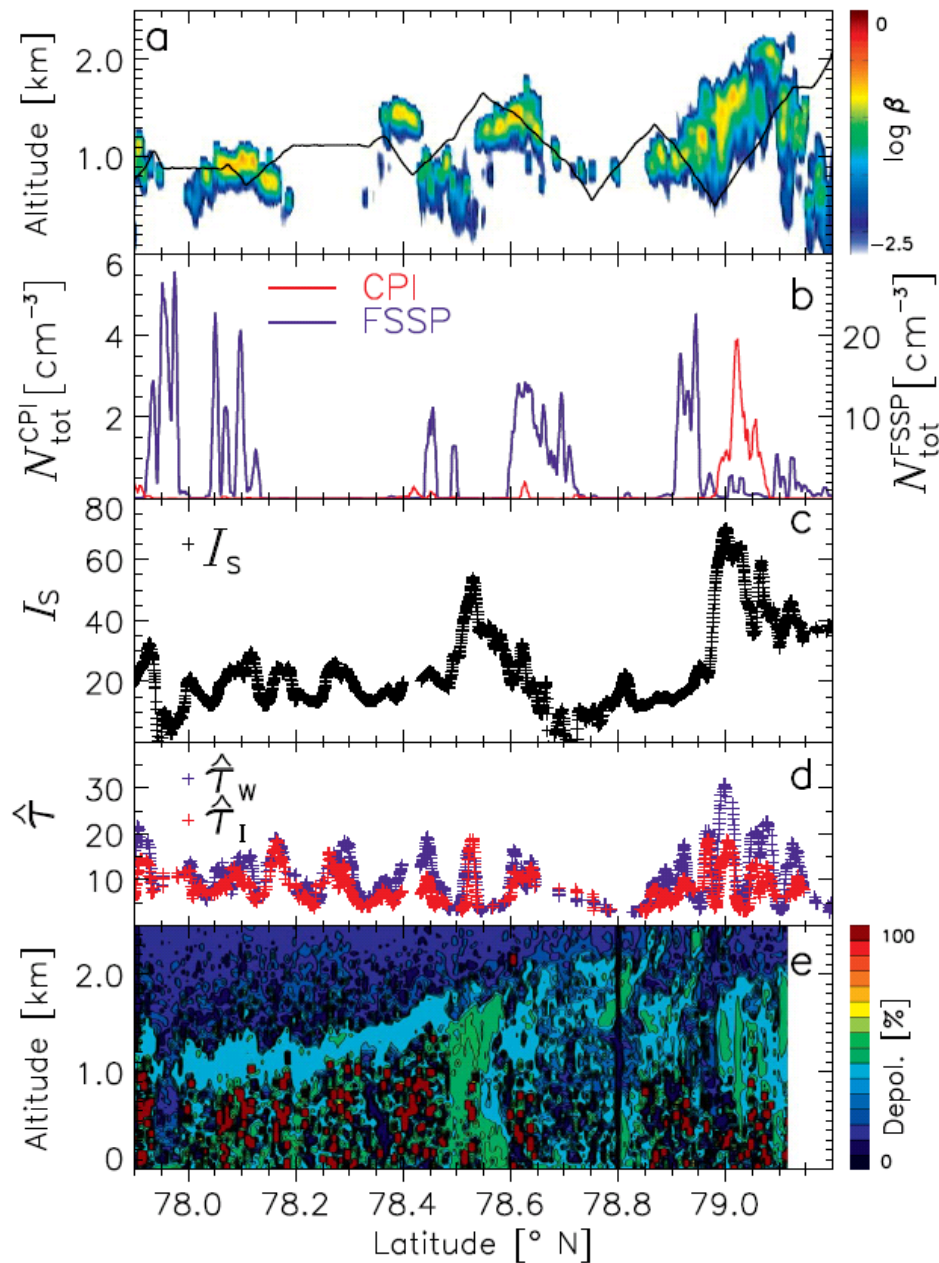


Figure 7.7: Overview of the measurements on 9 April 2007. The panels show the CALIOP attenuated backscatter coefficient and superimposed the flight altitude of the in situ measurements (a), in situ particle number concentrations (CPI representing ice particles, FSSP liquid droplets, b), as well as the synchronously recorded ice index (c) and cloud optical depth (d, albedometer, see Sect. 5.3) and depolarization (e, AMALi). Plot provided by André Ehrlich.

Figure 7.7 provides an overview of the different measurements along the flight track coordinates. The upper panel (a) shows the time series of CALIOP attenuated backscatter of clouds measured around 10:06 UTC. The superimposed black line indicates the flight altitude during the in situ probing. In situ measurements (Gayet et al., 2009) were performed during successive descent / ascent slant profiles at a flight altitude between 500 m and 1700 m. Panel b provides the in situ particle number concentrations of ice particles (red, represented by CPI measurements) and liquid water droplets (blue, FSSP measurements). Panel c shows the ice index I_s (Ehrlich et al., 2008), and panel d the optical thickness $\hat{\tau}$ estimated from cloud top radiation measurements under the assumption of pure ice (red) and pure liquid water (blue) phase (Sect. 5.3). For pure water clouds, the cloud optical thickness had values around 13-17

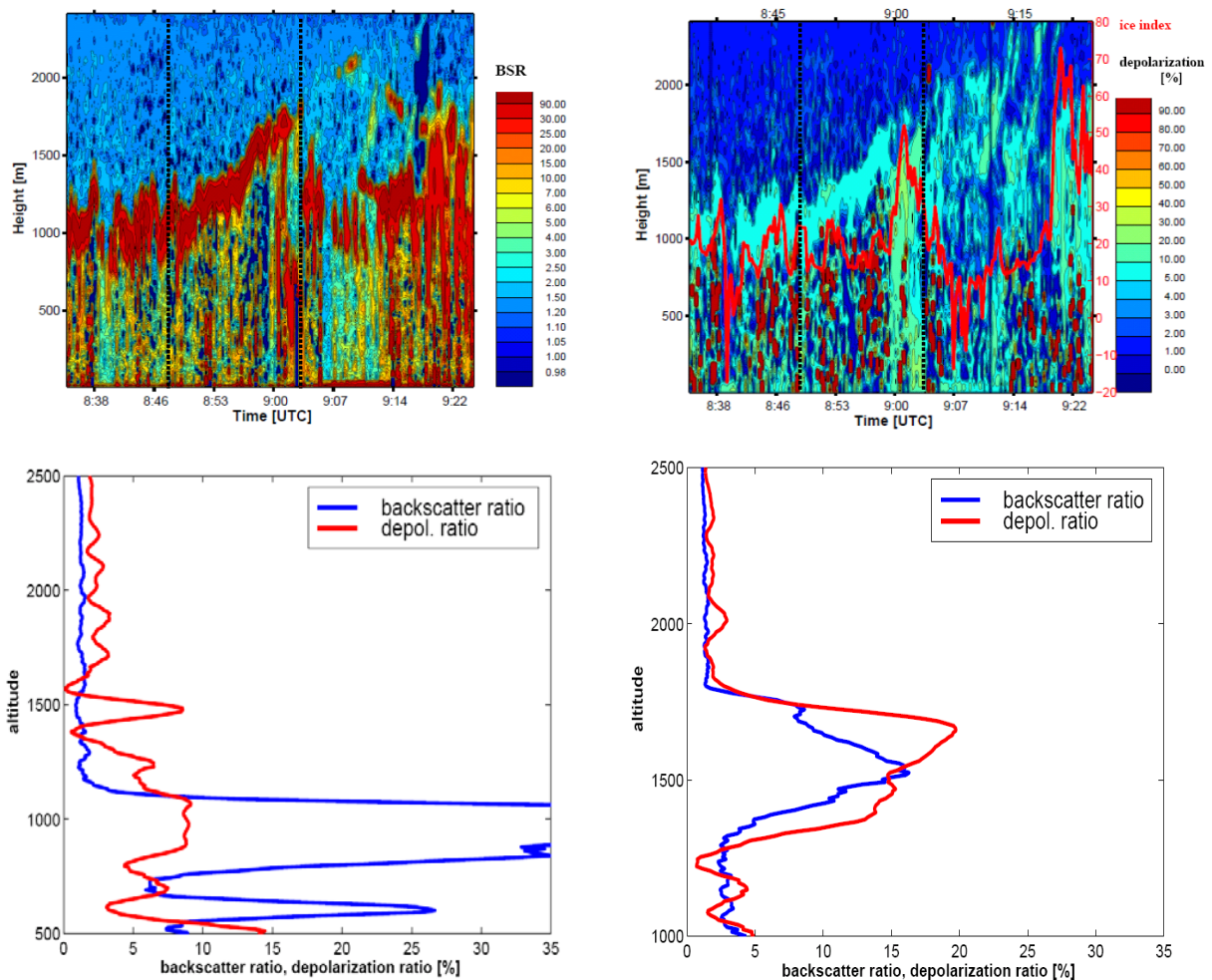


Figure 7.8, top: Time series of backscattering ratio (left) and depolarization ratio with superimposed ice index (right). The dotted vertical bars indicate the time steps of the profiles shown in the bottom panels.

Bottom: Profiles of backscattering and depolarization ratios for a liquid-topped cloud at 08:48 UTC (left) and an ice cloud at 09:03 UTC (right) on 9 April 2007.

for the continuous cloud deck in the South. In the mixing zone at 09:02, the mean optical thickness was lower (11-13 assuming pure ice). Finally, the last panel (e) shows the lidar depolarization measured synchronously with the ice index and optical depth. The cloud structures observed by space borne and airborne lidar are further discussed in Sect. 7.2.3.

In the clouds, a generally high number concentration of liquid water droplets (droplet concentration exceeding 20 cm^{-3} , Gayet et al., 2009) was detected. During one ascent, a thick water layer in the altitude of 900 to 1500 m was probed (profiles not shown). For one descent, a thin water layer was detected on cloud top at an altitude of about 900 to 1000 m. Below 900 m, ice crystals were found. Precipitation of ice crystals below cloud base was also captured by CloudSat radar observations (Gayet et al., 2009). The large number concentrations of liquid cloud droplets with an extinction coefficient of up to 35 km^{-1} explain the high backscattering ratio observed by lidar.

7.2.2 Cloud thermodynamic phase

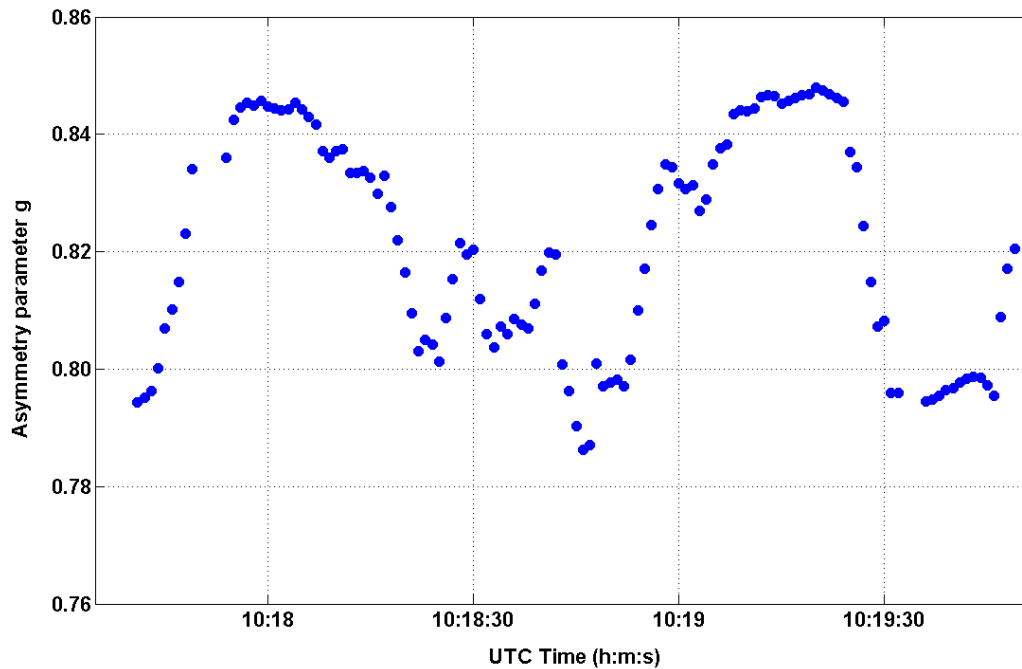


Figure 7.9: Time series of the asymmetry parameter in the mixing zone. During 15 seconds (around 900 m horizontal extent), only ice ($g < 0.82$) was found at an altitude of 900 m. Provided by Guillaume Mioche.

From lidar backscatter and depolarization profiles, the prevailing cloud thermodynamic phase was determined. The results were compared with the ice indices obtained from cloud top radiation and the asymmetry parameter derived from PN measurements.

The lidar observations on 8 April 2007 exhibited a strong backscattering ratio together with low volume depolarization at the cloud top (1500 m), increasing gradually with range (not shown). This indicates a liquid water layer on cloud top and multiple scattering effects (Hu et al., 2007). The clouds were optically too thick and attenuated the laser beam significantly, thus they did not allow lidar measurements down to the sea surface. Only once in a cloud gap at around 10:04 UTC (~ 36250 s in Fig. 7.4), the lidar was able to penetrate to the surface and detected ice precipitation, high depolarization and low backscatter, in the lowest 700 m.

Generally, the simultaneously performed cloud top reflection measurements showed the existence of mixed-phase clouds which were clearly dominated by water. The spectral pattern of the cloud reflectivity in the range 1550 – 1700 nm affected by ice and water absorption resulted in an average spectral slope ice index $I_S = 23$ for the mixed-phase clouds observed on 8 April ($I_S = 10$ corresponds to pure water, $I_S = 50-60$ to pure ice clouds, Ehrlich et al., 2008). The vertical profiles of the in situ measurements confirmed that the cloud system on 8 April 2007 was capped with a geometrically and optically thick layer dominated by water droplets. They demonstrated a 500 m thick layer of pure liquid water droplets and below ice particles (not shown). The in situ measurements were not performed near the ground, so no ice crystal precipitation could be observed.

The profiles of backscattering and depolarization ratio for 9 April 2007 (Fig. 7.8, bottom, left panel) generally exhibited the same cloud features as observed on 8 April (not shown). The depolarization values within the clouds were slightly enhanced (Fig. 7.8). The values around 10 % are typical for multiple scattering of a cloud consisting of mainly liquid water droplets.

This is consistent with the observations of glory from the aircraft (see Rauber and Tokay, 1991, Ehrlich et al., 2009). On two occasions, however, the depolarization signal was clearly enhanced (above 20 %) while the backscatter signal was comparatively low, which gives evidence of ice particles. Exemplary individual profiles of backscattering ratio and depolarization ratio for two time steps (08:48 and 09:03 UTC) are shown in Fig. 7.8 (lower panels). They exhibit different characteristics concerning the values and slopes of the profiles. A high backscattering ratio (above 30) and gradual increase of the depolarization with cloud penetration depth was found for the time step representative of the continuous cloud deck at 08:48 UTC. The analysis leads to the conclusion that multiple scattering was responsible for the enhanced depolarization ratios. A much lower backscattering ratio of 15 and a higher value of the depolarization ratio of 20 %, enhanced immediately at the cloud top, were observed in the air mass mixing zone.

The ice index I_S calculated from measured spectral cloud top reflectivity (Sect. 5.3) is shown in Fig. 7.7c. The mean value of the spectral slope ice index for the continuous cloud deck was $I_S = 18.5$, which is typical for mixed-phase clouds with predominantly liquid contribution. Two exceptions with an ice index up to 60 were recorded, indicating pure ice clouds below the aircraft at the same time when the lidar detected ice (around 09:02 and 09:20 UTC, compare Fig. 7.7d and e). This confirms the lidar observations of enhanced depolarization values, characterizing a glaciated cloud.

The in situ measurements (profiles not shown) found mostly liquid water droplets in the altitude between 900 and 1500 m (asymmetry parameter higher than 0.82) and ice particles below (asymmetry parameter smaller than 0.82). For single profiles, the water layer geometrical depth amounted to 1000 m (Gayet et al., 2009). However, a pure ice cloud with considerable ice content (extinction coefficient up to 20 km^{-1}) was recorded at 10:18 UTC. As can be seen in Fig. 7.9, the asymmetry parameter was below 0.82 for 15 seconds (horizontal extent of around 900 m). The measurements cannot be compared directly to the radiation observations due to the time delay and advection. However, the spatial characteristics of liquid water clouds observed by in situ measurements are in agreement with the vertical extent of the liquid cloud layer from the airborne lidar measurements.

The clouds on 9 April revealed their special feature along the mixing zone of the two different air masses (cold air from the North, warmer air mass advected from the South-West): both the enhanced lidar depolarization and the high ice indices showed the existence of a pure ice cloud. The in situ measurements were performed around 1 h later. Due to advection, the cloud could not be probed at the same intersection again. But pure ice, identified by the low asymmetry parameter of PN data and the CPI detection of ice crystals, was equally found at the mixing zone (Fig. 7.9), indicated by the transition of the temperature profiles as described above.

Further, near the turning point in the North-West, another completely glaciated part of the cloud was observed by lidar and albedometer (Fig. 7.7, at 79° N).

Qualitatively, the identification of cloud phase of all three instruments agreed, even with the time delay between the in situ and remote measurements. Advection of the sampled air masses was taken into account for comparison. The instruments probed mixed-phase clouds dominated by a liquid topped layer, and they twice observed the existence of a completely glaciated area.

The ice phase in the air mass mixing zone underlines the importance of vertical motion. The general updraft with moist air from the warmer ocean is disrupted by the turbulences of mixing air masses. As shown by Korolev and Isaac (2003), Shupe et al. (2007), and Korolev and Field (2008), the updraft and the supply with moist air are responsible for the formation of new liquid droplets. They are in equilibrium with the formation and subsequent growth

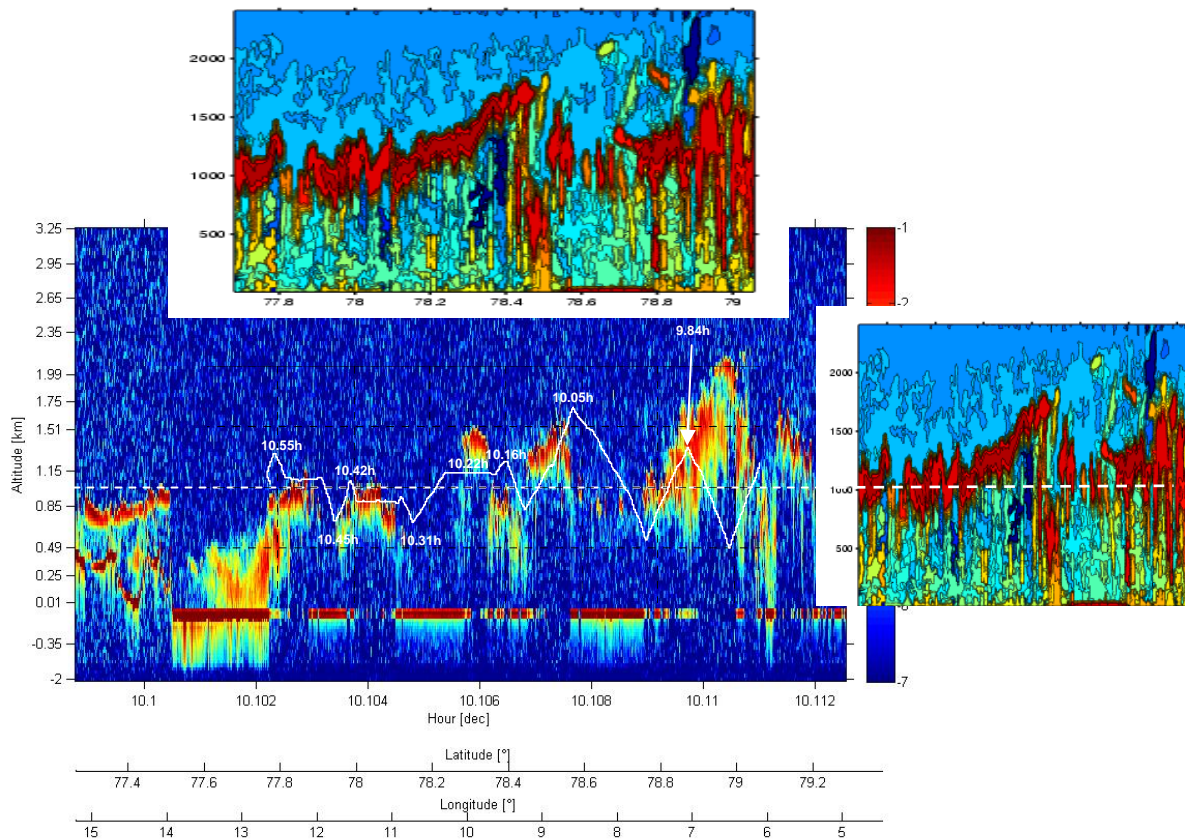


Figure 7.10: Time series of attenuated backscatter of the space borne CALIOP lidar and the airborne AMALi along the same flight track. The time delay between the measurements is approximately 1 h. Provided by Guillaume Mioche. CALIPSO data were obtained from the NASA Langley Research Center.

(WBF process) and removal of ice crystals from near cloud top. If the moisture supply is disturbed, no more liquid cloud droplets form, and the cloud quickly glaciates completely. Hereby, the area of glaciation is limited, and does not contact other parts of the cloud. After around 1 h, the same phenomenon of a small glaciated area within the cloud system was still observed with the in situ sensors. This suggests the existence of stable cloud cells with little horizontal exchange of air masses and slowly proceeding entrainment / detrainment processes.

7.2.3 Cloud comparison with CALIPSO

With the purpose of validating the CALIOP lidar data, the Polar-2 route on 9 April 2007 was chosen along the satellite track. The coincidence was planned for in situ cloud observations on the way back along the same path. Therefore, the time delay of around 1 h between the two lidar measurements led to differing cloud structures observed by space borne CALIOP lidar and the AMALi data. This can be attributed to advection and dynamical cloud processes during the time delay. Figure 7.10 shows the profiles of CALIOP attenuated backscatter (background panel) and AMALi backscattering ratio (small upper panel) along the same geographical coordinates. Further, a direct comparison of cloud altitude is given by the same vertical scale and the horizontal white line at 1000 m altitude linking the CALIOP and the AMALi time series (small right panel). The two lidar systems probed boundary layer clouds. Both observations have in common that the cloud top height increases towards the North. However, in the CALIOP data, the continuous cloud deck evidenced by airborne lidar is missing, all clouds occur as scattered patches. Cloud gaps were pronounced. Further, the

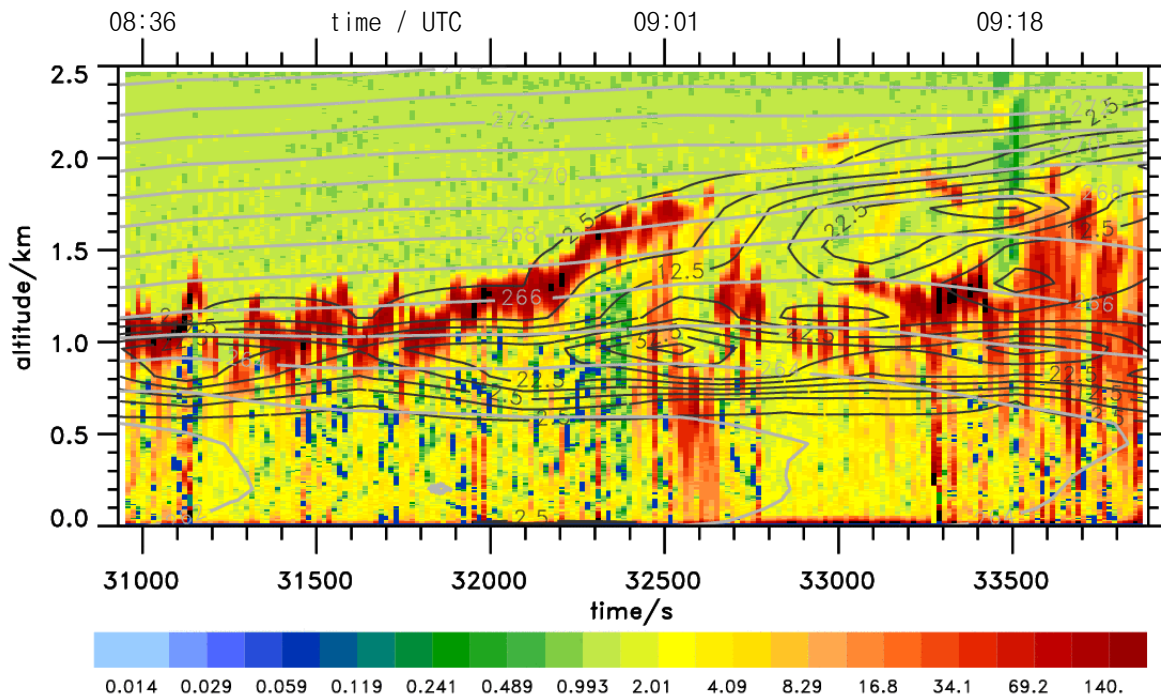


Figure 7.11: Time series of nadir lidar backscattering ratio (color coded). Superimposed are the potential temperature (K, gray) and the total cloud water content (sum of cloud liquid water content and cloud ice water content, mg kg^{-1} , black) determined by ECMWF analyses. Provided by Andreas Dörnbrack.

cloud top altitude measured by CALIOP was lower than the height detected one hour earlier by AMALi. In the case of cloudy profiles, the CALIOP laser pulses were completely attenuated and did not penetrate to the surface. Therefore, no information about cloud bottom and the geometrical thickness of the clouds can be obtained from the space borne lidar observations. The lower penetration depth into the clouds is caused by the high satellite velocity above ground and the integration over few laser pulses only. A horizontal resolution of 1 km in flight direction, similar to the standard AMALi resolution for an integration time of 15 s, is achieved by averaging over 3 single CALIOP lidar profiles.

For a detailed comparison of airborne AMALi and satellite borne CALIOP lidar data of boundary layer clouds, more parallel observations including direct overpasses, and a smaller time delay would be necessary.

7.2.4 Cloud comparison with ECMWF analyses

The cloud structures observed by the airborne backscatter lidar were compared to ECMWF cloud analyses interpolated in space and time along the flight track. Figure 7.11 shows the profiles of the backscattering ratio as color coded picture. The superimposed contour lines represent the potential temperature (gray) and the condensed water content (black), i.e. the sum of cloud liquid water and ice water content. With the cloud threshold value of 2.5 mg kg^{-1} , the modeled cloud boundaries agree with the cloud top and bottom height determined by airborne lidar backscatter. The feature of increasing cloud top following the growing boundary layer depth towards the North is well captured. However, with the coarse model resolution of 25 km, small scale cloud structures cannot be resolved.

While the ECMWF model was able to represent the vertical and horizontal cloud extent of not too small cloud structures, the partitioning of the cloud condensate into liquid and ice fraction

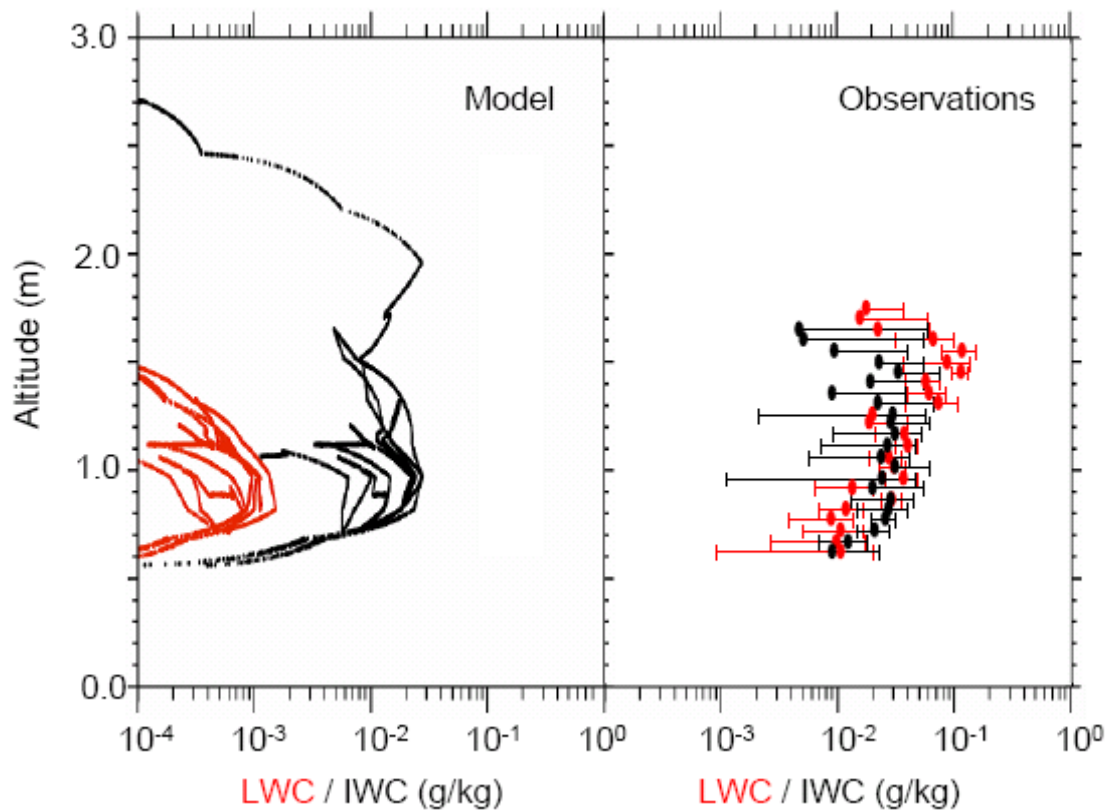


Figure 7.12: Comparison of liquid water content and ice water content calculated from ECMWF analyses (left) and in situ observations (right) for the cloud observed on 9 April 2007. The horizontal bars indicate the standard deviation of the measured values. Figure 10 from Gayet et al. (2009).

could not reproduce the measured distribution of the cloud phase. The partitioning is implemented as a function of temperature in the ECMWF model, with the result that generally more liquid water was modeled for the warmer cloud areas at cloud bottom, while the cloud top consisted of predominantly ice. Gayet et al. (2009) compared directly the in situ measurements of liquid water content and ice water content for the particular clouds on 9 April 2007, horizontally averaged over 1500 m, with the ECMWF analyses interpolated to the corresponding coordinates, altitude and time. The modeled liquid fraction was 0-0.1, while the measured liquid fraction amounted to 0.43-0.8 (Gayet et al., 2009). The vertical profiles of modeled and observed liquid water (red) and ice water content (black) are shown in Fig. 7.12. It is obvious from the profiles that liquid water is underestimated in the model by at least an order of magnitude and peaks near cloud bottom, while the in situ observations evidence a maximum liquid water concentration near cloud top. This is in agreement with lidar and albedometer observations (Sect. 7.2.2) and commonly observed in Arctic mixed-phase clouds (Sect. 2.1). As cloud phase essentially influences both solar and terrestrial radiation, the modeled surface radiation will be biased by the erroneous cloud representation.

7.3 Midlevel clouds

In contrast to multiple cloud layers in the Arctic boundary layer observed regularly in summer (e.g. Intrieri et al., 2002a, Luo et al., 2008, see Sect. 2.1), multiple layer clouds in the free troposphere are less frequently reported. A complex multiple layer cloud system with layers up to 5.5 km altitude was analyzed by Hobbs et al. (2001). They found ice crystals falling

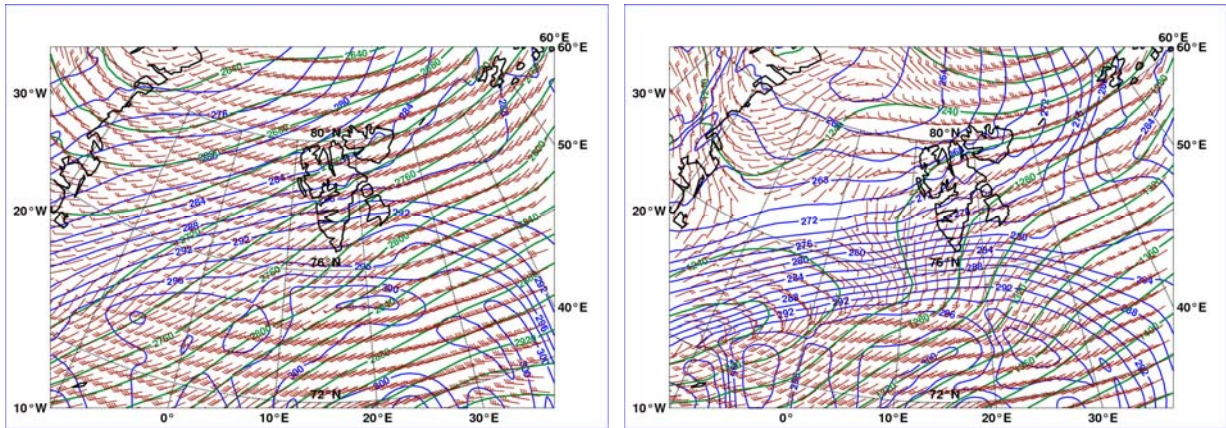


Figure 7.13: ECMWF analyses of geopotential height (green), potential temperature (blue) and wind speed (barbs) at a pressure level of 700 hPa (left) and 850 hPa (right) for 14 April 2007, 18:00 UTC. The flight track along the West coast of Svalbard is indicated as a red line. Provided by Andreas Dörnbrack.

from the individual cloud layers into lower layers, and at times evaporating above ground. The flight on 14 April 2007 was dedicated to the investigation of midlevel clouds, which were predicted by ECMWF forecast. The Polar-2 aircraft went towards the South along the West coast of Svalbard, in the direction of an approaching high pressure system. For a horizontal extent of around 30 km (8 flight minutes) from 16:18 to 16:26 UTC, a two-layer cloud structure was observed by the zenith pointing AMALi. As the aircraft was cruising at constant altitude (1330 m) only until 16:24 UTC, the evaluation of the data focuses on this first part of the lidar cloud observations. The short flight track is indicated as red line in the synoptic analyses (Fig. 7.13) and the charts of relative humidity (Fig. 7.15).

The lidar signal was smoothed with a running mean over 10 data points vertically, and the time resolution was 15 s, corresponding to a horizontal resolution of about 930 m. The signal to noise ratio at 4 km altitude then amounted to 15.

7.3.1 Synoptic situation and cloud structure

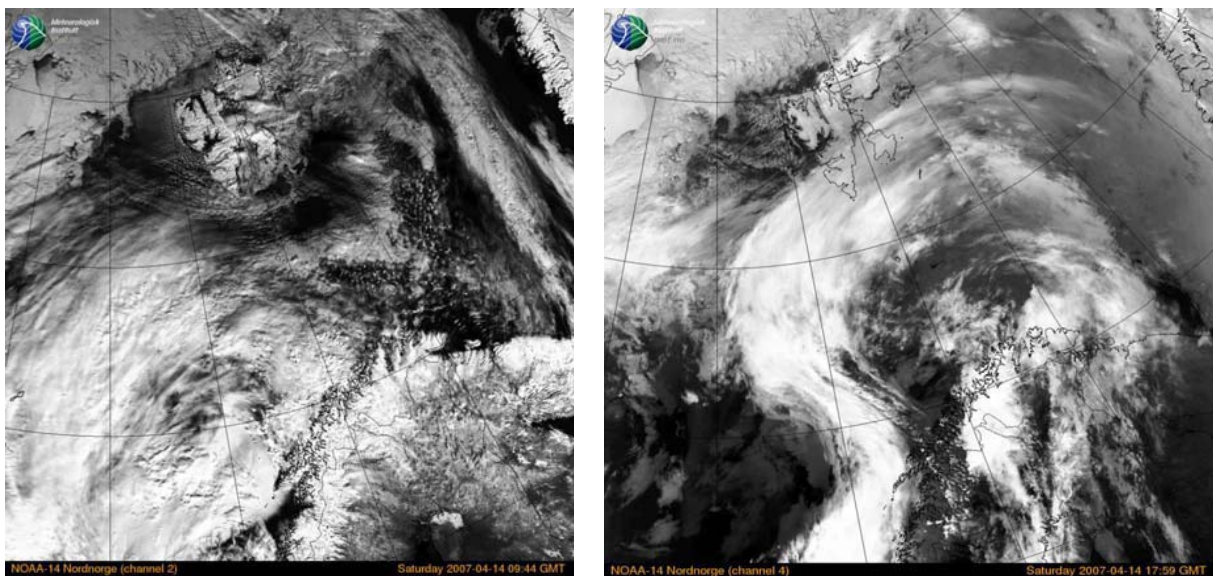


Figure 7.14: NOAA satellite images of 14 April 2007. Left: Channel 2 (VIS) at 09:44 UTC, right: Channel 4 (IR) 17:59 UTC. The approaching cirrus shield covers the southern part of Svalbard. Courtesy of the Norwegian Meteorological Institute, Tromsø, Norway.

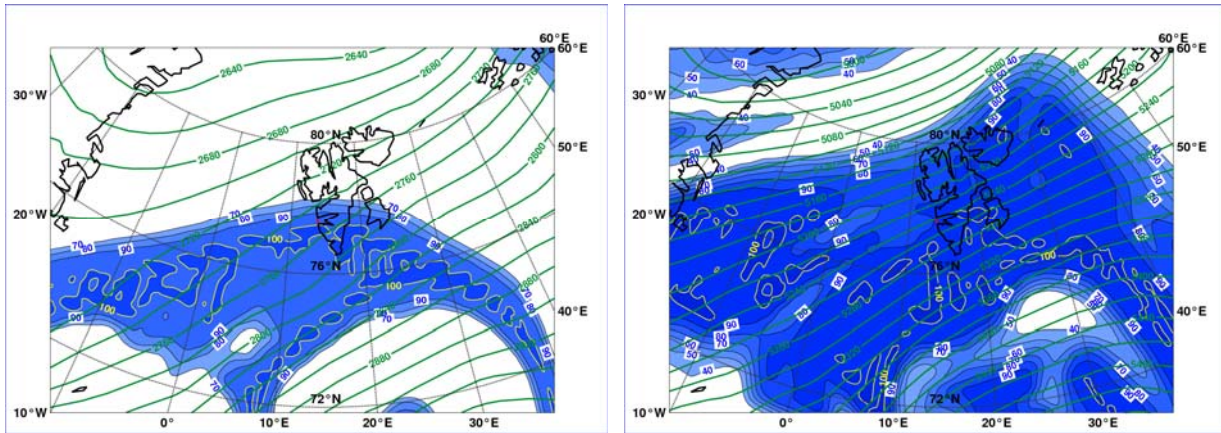


Figure 7.15. Geopotential height and relative humidity on 14 April 2007, 18:00 UTC, at a pressure level of 700 hPa (left) and 500 hPa (right). The flight track along the West coast is indicated as red line. Provided by Andreas Dörnbrack.

Meteorological ECMWF analyses performed for 14 April 2007 revealed that on the rear side of a through propagating eastward, the low level wind turned from north-westerlies to easterlies in the period from 12:00 UTC till 18:00 UTC. However, the wind speed was rather low with values around 2 m s^{-1} at 10 m altitude. The prevailing easterly winds near ground level turned to westerlies at higher pressure levels above Spitsbergen (Fig. 7.13).

Associated with the approaching ridge, warm and moist air was transported to the Svalbard area at the altitude of the cloud observation. A cirrus shield is clearly visible in the NOAA satellite images (7.14). As the wind at the aircraft's cruising altitude during the cloud observation came from the West, the lidar observations were performed along a cross section perpendicular to the wind direction prevailing at cloud level.

ECMWF analyses reveal the existence of an area of humid air masses (relative humidity around saturation) at 700 hPa and enhanced relative humidity up to 90 % at 500 hPa (Fig. 7.15). Midlevel clouds were therefore calculated in the observation area. However, the small scale structures of the observed cloud could not be resolved by the ECMWF analyses.

Two separated geometrically thin liquid clouds (150 m thickness) with high backscattering ratio and low depolarization were observed (Fig. 7.16 and 7.17). The upper cloud was centered at 4.2 km altitude, the lower cloud at 3.9 km. In between, the enhanced depolarization and low backscatter signal revealed the existence of precipitating ice particles. The temperature at 4 km altitude was estimated to be around $-25 \text{ }^{\circ}\text{C}$ (radio sonde measurement in Ny-Ålesund at 11:00 UTC). A cirrus cloud was located above the two-layer cloud system with a slanted cloud base at around 5.5 km (not shown in Fig. 7.16), which made it impossible to compare the lidar data of the cloud properties with albedometer measurements of downwelling radiation. The detection of the cirrus cloud proved that the laser pulses penetrated the two-layer cloud, and was not attenuated completely. The cloud boundaries are therefore reliable despite the occurrence of multiple scattering. As this effect leads to an enhanced apparent optical depth (Nicolas et al., 1997), only a maximum value for the optical depth can be estimated as follows: The maximum backscatter coefficient of the upper liquid layer was around $10^{-4} \text{ m}^{-1} \text{ sr}^{-1}$. By multiplication of this value with a typical cloud LR of 20 sr, and integration over the cloud altitude (150 m), the optical thickness of one liquid cloud layer is estimated to be in the order of 0.3, thus quite thin.

In the case of 14 April 2007, different mechanisms might be responsible for the lifting of the air masses and cloud formation: A possible scenario is that the humid air masses were lifted orographically. Until about 12:00 UTC, westerlies dominated in the lower troposphere and the flow perpendicular to the coast line passed the mountains of the Svalbard archipelago.

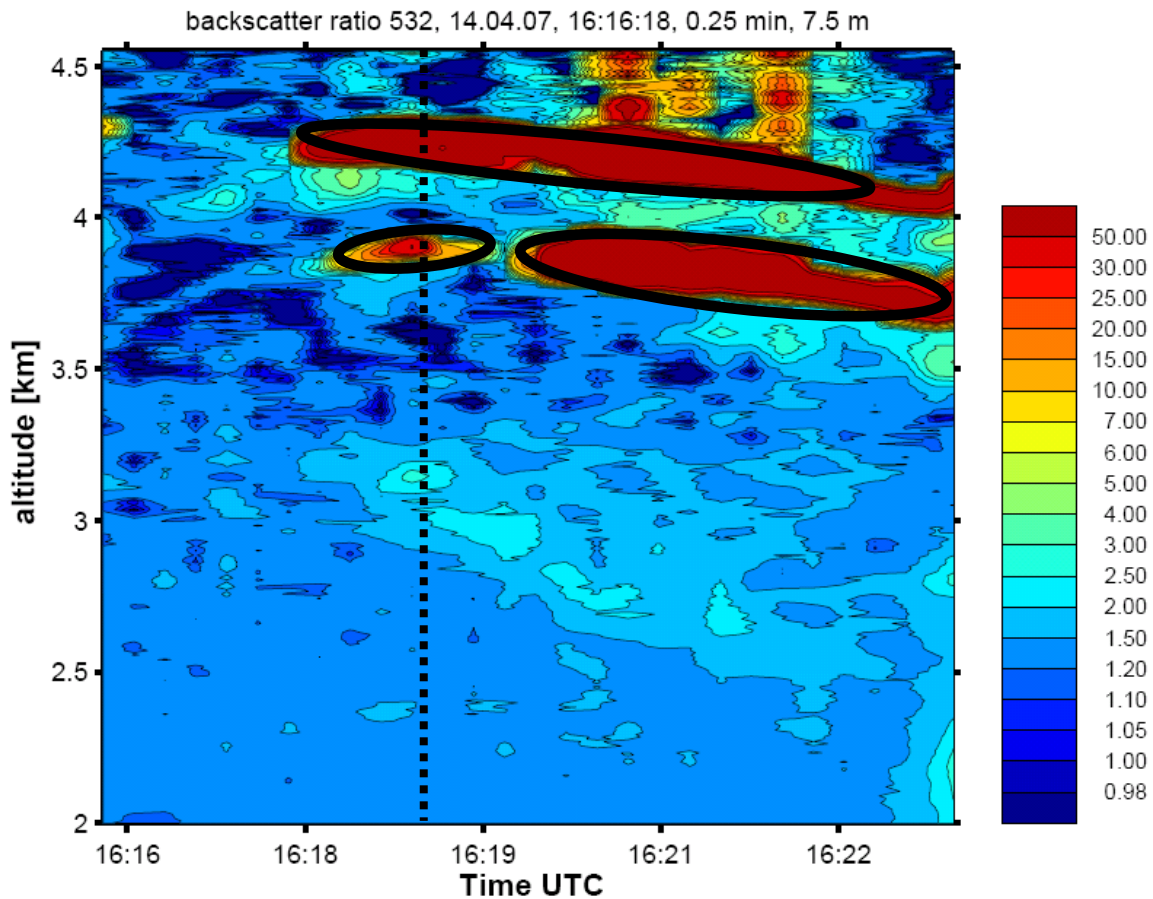


Figure 7.16: Zenith measurements of lidar backscattering ratio on 14 April 2007. Encircled in black are the cloud areas of high backscatter values. The dotted vertical bar indicates the time step of the lidar profile shown in Fig. 7.18.

However, the cloud was observed on the windward side and in the direct vicinity of Svalbard (less than 5 km off land). Therefore, the observed clouds cannot be typical lee wave clouds. Another possible explanation is that the flow above the Svalbard archipelago was interrupted by the change of the wind direction in the lower troposphere. As the forcing of gravity waves diminishes, an upstream shift of the waves might occur under these transient conditions (Chen et al., 2007).

A third possibility is that cloud filaments formed due to the enhanced vertical and horizontal wind shears in the strongly divergent flow. Lifting by one of the mentioned mechanisms and subsequent cooling of the moist air is probably the cause of the formation of at least the upper liquid cloud layer. As precipitation between the individual cloud layers was observed, and the lower liquid cloud layer exhibited a smaller optical thickness, the double-layer structure might be the result of ice crystal precipitation which evaporated below the upper cloud (as proposed by Harrington et al., 1999). Radiative cooling by the upper cloud layer or further orographic lifting led to cooling of the humid layer, resulting in the second cloud layer.

7.3.2 Cloud thermodynamic phase

The cloud phase of the double layer cloud observed on 14 April 2007 was determined from the profiles of backscatter and depolarization ratio. In the time series of the backscattering ratio (Fig. 7.16), the areas of enhanced values above 30 are encircled in black. The

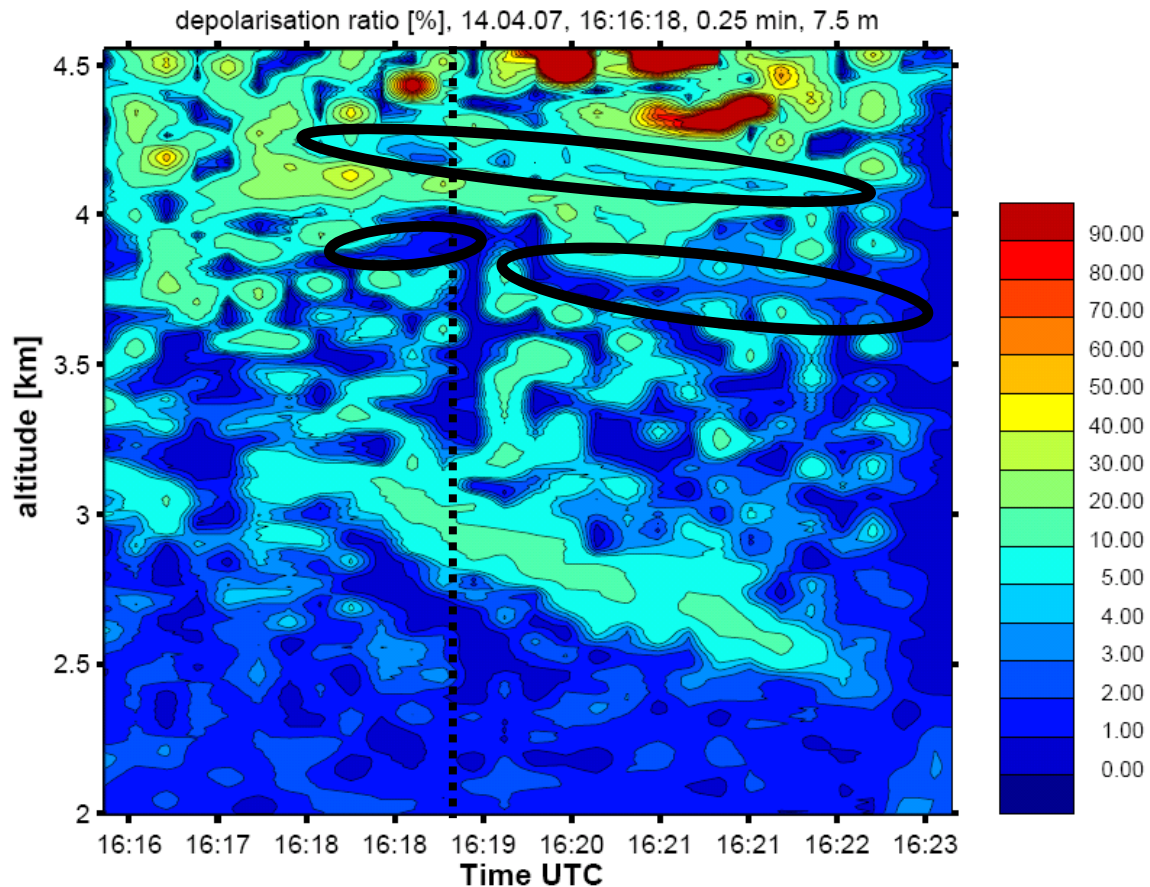


Figure 7.17: Zenith measurements of depolarization ratio on 14 April 2007. Encircled in black are the same cloud areas as in Fig. 7.16. The dotted vertical bar indicates the time step of the lidar profile shown in Fig. 7.18.

depolarization values at the same altitudes are depleted (Fig. 7.17). The analysis of single profiles of backscatter and depolarization ratio, as shown in Fig. 7.18, provides further evidence of two geometrically thin liquid water clouds with ice below each liquid layer: The gradual increase of the depolarization signal in the highly backscattering height intervals is caused by multiple scattering, whereas the prompt increase of the depolarization signal below the liquid cloud layers is interpreted as the existence of depolarizing ice crystals.

7.4 Discussion: Airborne lidar retrieval of cloud properties

Elastic lidar systems provide valuable information on the vertical cloud structure in high spatial and temporal resolution. Thereby lidar observations cover the range from optically subvisible, thin to moderately thick clouds at all altitudes. However, lidar measurements alone are not sufficient to describe cloud properties. Additional instruments for radiation and in situ data are necessary.

Optically thin to subvisible clouds can easily be observed with lidar systems (Chapt. 6). With the assumption of single scattering being valid, the optically thin clouds can be characterized by a quantitative backscatter coefficient and depolarization ratio. This allows reliable determination of the cloud structure and cloud phase. Subvisible clouds occur more than just occasionally in the Arctic (Wyser et al., 2008). They cannot be neglected for radiative transfer calculations under all circumstances.

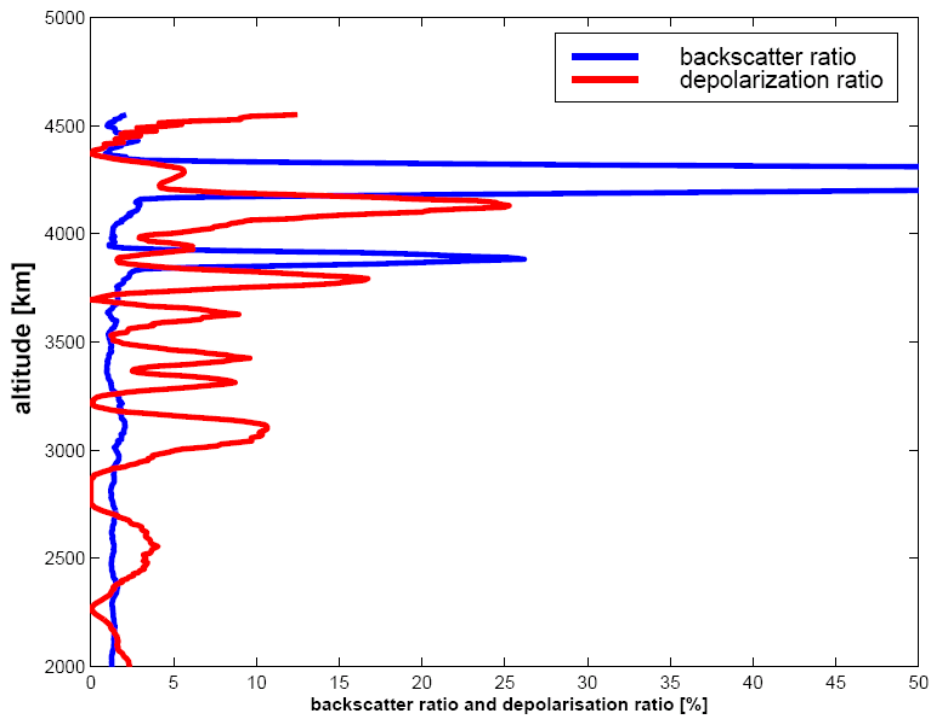


Figure 7.18: Profiles of zenith lidar backscatter and depolarization ratio on 14 April 2007 (16:18:45 UTC).

On the other hand, optically thick clouds attenuate the lidar signal and lead to multiple scattering, which influences the detection of backscattered light in both polarization directions. The photons scattered more than once are detected at a later time, provoking an afterglow effect behind the cloud. This can be seen in the CALIOP lidar data below thick clouds and also below the ground return (Fig. 7.10). Therefore, the lidar signal cannot be evaluated quantitatively within and behind the clouds.

At least cloud top or cloud base of a cloud system can be determined straightforward from lidar observations depending on the viewing direction of the lidar. In the case of airborne nadir measurements, the cloud top of boundary layer clouds additionally provides an indication of the height of the planetary boundary layer. If the lidar signal is not attenuated completely, the cloud base can be observed. This is practiceable for optically thick clouds with an optical depth up to 3 (You et al., 2006) in the case of homogeneous cloud systems, and up to an optical depth around 15 for clouds with small local inhomogeneities (as shown for 9 April 2007). The usually very high backscattering of liquid water clouds enables to receive an enhanced signal from the whole cloud range to the other cloud boundary. However, in this case, no quantitative analysis of the lidar profile and therefore calculation of the optical thickness can be performed. As criterion if the second boundary was reliable, the observation of further cloud structures or the ground return through an optically thick cloud was used. In the CALIOP profiles (Fig. 7.10), the ground return is not visible below the clouds on 9 April 2007, and the cloud geometrical thickness cannot be determined reliably. In contrast, the ground return is visible for most time steps of the AMALi measurements of 9 April 2007 (Fig. 7.5). On 14 April 2007, a cirrus cloud above the double-layer cloud was detected (not shown).

With depolarization lidar, the thermodynamic phase of the cloud layer closest to the lidar system can be retrieved, which plays a crucial role for the surface energy budget (McFarquhar and Cober, 2004). The relation of parallel and cross-polarized signals reveals whether the scattering particles are mainly liquid droplets or ice crystals. For liquid water clouds, the backscatter and the depolarization are positively correlated, while for ice clouds, the depolarization decreases with penetration into the cloud. The relation was investigated in

detail for CALIOP data (Hu et al., 2006, 2007). The analysis of the airborne lidar profiles of 9 and 14 April (Figs. 7.8 and 7.18) showed a similar behaviour: For layers dominated by liquid water droplets, the depolarization increases gradually with penetration into the cloud, while the backscatter ratio is enhanced immediately at the cloud boundary. For ice clouds, the depolarization is enhanced immediately and exhibits higher values than for the typical multiple scattering effect.

The combination of simultaneous lidar and albedometer measurements provided complementary information, which upgraded the data evaluation of both instruments: the lidar provides information on the cloud altitude and structure, while the albedometer obtains values of the cloud optical thickness for optically thick clouds. The thermodynamic cloud phase can be intercompared.

In order to reduce uncertainties caused by advection and the temporal development of clouds on a short time scale, the parallel in situ investigation of cloud microphysical and optical properties would be desirable. The accuracy of direct validation and closure calculations between the different remote sensing and in situ observations could be improved drastically by the use of two coordinated aircraft, one flying above or below the cloud layer with the remote sensing instrumentation, one probing the cloud with the in situ technique. The setup using two aircraft, one with the in situ instruments Polar Nephelometer, PMS-FSSP, PMS-2D-C, and CPI, the other with a backscatter lidar and radar, was successfully applied during the CERCLE-2 campaign for the CALIPSO satellite validation of cirrus clouds (Mioche et al., 2009).

8 Outlook

This final chapter provides a review of the cloud studies presented in the thesis and an outlook on further research activities.

8.1 Summary of results

With the combination of airborne lidar, spectral solar radiation and in situ sensors, cloud formations typical of the Arctic troposphere were investigated. The cloud studies include the observation of an optically subvisible midlevel ice cloud (Chapt. 6), boundary-layer mixed-phase clouds (Sect. 7.2) and a multi-layer midlevel cloud (Sect. 7.3). The lidar measurements served to indicate the vertical and horizontal cloud structures, especially the cloud height and small- and mesoscale features, as well as to identify the prevailing cloud phase. For the thin cloud, a quantitative analysis of the optical properties (backscatter and extinction coefficient, cloud optical depth, lidar ratio) and a rough estimate of microphysical properties (existence of small particles) were provided by lidar observations.

The subvisible ice cloud occurring at 3 km altitude and $-24\text{ }^{\circ}\text{C}$ (10 April 2007) was detected by lidar despite the very low particle concentration (0.2 cm^{-3}). The high depolarization values evidenced non-spherical ice crystals. Further, the lidar color ratio suggested the existence of small ice particles (effective diameter smaller than $5\text{ }\mu\text{m}$). Following the guidance of the lidar, the aircraft flew into the cloud, and it was probed by the in situ instrumentation. The subvisible cloud appeared also in the data of spectral downwelling solar radiance and broadband downwelling IR radiation. Radiative transfer calculations simulating the subvisible ice cloud were performed combining the data of the airborne sensors mentioned above. The total cloud forcing was determined as -0.4 W m^{-2} . This slight cloud surface cooling is negligible on the local scale. However, similar clouds might be of importance in winter, when the positive longwave forcing of 2.8 W m^{-2} is not balanced by the negative shortwave forcing. Depending on the geographical extent, the amount of cloud forcing is considerable. The comparison of regional climate models with observations of cloud cover in winter time during the SHEBA experiment suggests that optically thin clouds are a common phenomenon in Arctic winter (Wyser et al., 2008). A detailed analysis of the frequency of occurrence of this cloud type, e.g. using the CALIOP data set, is beyond the scope of the case study presented here. For the possible application in climate modeling, the open question about the presence and extent of such cloud formations is worth further investigations in a future study.

Two observations of boundary layer mixed-phase clouds revealed the typical structure observed regularly in the Arctic, an optically thick layer dominated by liquid water on top and ice crystals below (Pinto, 1998, Shupe et al., 2008). For homogeneous clouds (8 April 2007), the upper layer could not be penetrated by the laser pulses. However, in the presence of small-scale inhomogeneities (9 April 2007), the lidar was able to probe the atmosphere down to the surface and determine the geometrical thickness of the upper layer. This is of interest for radiative transfer calculations, as the properties of the uppermost cloud layer dominate the scattering of solar radiation (Ehrlich et al., 2008). The lidar cloud measurements were validated with spectral solar radiation and in situ observations. One open topic is the sensitivity of lidar depolarization to a mixture of very few ice crystals and a high concentration of liquid cloud droplets. The increase of the depolarization signal caused by multiple scattering and possibly few ice crystals could not be distinguished and should be examined by theoretical calculations. Radiative transfer calculations reproducing the spectral radiation measurements evidenced the existence of few ice crystals in mixed-phase clouds near cloud top (Ehrlich et al., 2009), which could not be resolved with lidar.

The flight track on 9 April 2007 was chosen along the CALIPSO satellite footprint. For a detailed intercomparison with space borne CALIOP lidar data, more parallel airborne and space borne measurements are necessary. In the comparison of the boundary layer mixed-phase clouds on 9 April 2007, the lidar systems showed agreement about the increase of the cloud top height towards the North despite the time delay of 1 h between the observations. In contrast to the airborne lidar, CALIOP measurements could not penetrate the inhomogeneous clouds down to the surface.

The evaluation of meteorological analyses confirmed lidar as an appropriate tool to link cloud properties and the synoptic situation. Composites of lidar backscatter data and meteorological parameters obtained by ECMWF operational analyses showed good agreement of the boundary layer height, location and vertical extent of clouds and mesoscale heterogeneity. This finding might be of interest for improving the cloud parameterization in climate models (Sect. 8.3). However, a cloud parameterization with only one prognostic equation for cloud condensate is utilized in the ECMWF model. The comparison of lidar and especially in situ cloud observations of 9 April 2007 with operational ECMWF analyses revealed serious shortcomings: the partitioning of liquid water and ice water, the absolute amount of liquid water and ice, precipitation and the vertical distribution of liquid on top and ice below could not be reproduced by the model (Gayet et al., 2009). This confirms previous results obtained by Beesley et al. (2000).

A double layer structure of two geometrically thin liquid cloud layers with ice below each liquid layer was further observed in the free troposphere (14 April 2007). Compared to the common phenomenon of multiple cloud layers in the Arctic boundary layer in summer (Intrieri et al., 2002a, Luo et al., 2008), this cloud type is less frequently reported at midlevel altitudes. Possible formation mechanisms were analyzed in the meteorological context. The lifting of humid air masses was influenced by local orography, as the flight took place in the direct vicinity of Svalbard. Evaporation of the observed precipitating ice crystals, and consecutive lifting of the humid air masses leading to condensation, may have caused the second layer.

The airborne instrumentation allowed the evaluation of the lidar cloud observations. The spectral radiation measurements provided the cloud thermodynamic phase and estimates of the cloud optical thickness. The in situ instruments delivered the cloud particle number concentration, particle size and shape, and extinction for liquid and ice phase, identified by the asymmetry parameter. The agreement of the instruments was generally good.

In conclusion, the unique combination of airborne lidar, spectral radiation and in situ measurements was used to characterize different cloud types of the Arctic troposphere above the remote Arctic Ocean. Four case studies were reported, which were analyzed in the meteorological context. The main scientific results are

- particular airborne cloud observations above the inaccessible Arctic Ocean
- the determination of the cloud forcing for an optically thin ice cloud
- the quantification of ECMWF shortcomings concerning the partitioning of cloud condensate into liquid water and ice and the vertical distribution
- the proposition of using two coordinated aircraft, one carrying the in situ, the other the remote sensing instrumentation for future cloud studies.

8.2 Conclusions: Airborne lidar for cloud research

In Chaps. 6 and 7, the results of different cloud studies performed with airborne lidar were presented. The following information on cloud properties was derived:

- Airborne elastic lidar measurements provided reliable information on the **vertical and horizontal cloud structures** in high spatial and temporal resolution. The basic information about cloud location and altitude is essential for understanding cloud formation and evolution processes as well as for radiative transfer studies (Shupe and Intrieri, 2004) and the validation of climate model output (Inoue et al., 2006).
- With depolarization measurements, the **thermodynamic phase** of the cloud layer closest to the lidar system was retrieved even under conditions of multiple scattering. The thermodynamic phase of Arctic clouds, especially in mixed-phase clouds, is subject to current investigations (Ehrlich et al., 2009) as it plays a crucial role for the surface energy budget (McFarquhar and Cober, 2004).
- In certain limits, the calculation of **optical and microphysical properties** from airborne lidar data was possible. For optically thin clouds, the backscatter coefficient can be retrieved, and with further assumptions also the extinction coefficient and optical depth. For optically thick clouds, only an estimation of these properties can be given. In Chapt. 6, the lidar ratio of an Arctic ice clouds was determined from in situ and remote sensing information, yielding a result of 21 sr. The retrieval of the *LR* provides valuable information about the existence of small cloud particles as well as internal processes in clouds (e.g. the growth / shrinking of small-size cloud particles).
- The **existence of subvisible clouds**, which occur at least occasionally in the Arctic, can be evidenced with airborne lidar. Their radiative impact was found to be small, but not negligible for the Arctic winter, and they should be considered in radiative transfer calculations. Little is known about the frequency of occurrence of these subvisible clouds. However, the study of Wyser et al. (2008) suggests the existence of many optically thin clouds in winter. As shown in Chapt. 6, lidar measurements constitute a suitable tool for further investigating this cloud type.

The results of the thesis confirm that airborne elastic lidar observations deliver information about cloud structure, cloud phase, optical properties, and even rough estimates of cloud microphysical properties in high temporal and spatial resolution.

However, the necessary information for radiative transfer calculations of Arctic clouds, the single scattering albedo, particle number concentration, particle size distribution, liquid water content, and ice water content, need other measurement techniques. They were available during the ASTAR 2007 campaign.

For remote sensing of clouds, the coupling of lidar with radar and IR radiometer provides complementary additional information: lidar observations are highly sensitive to the relatively small liquid cloud droplets, and radar to the larger ice crystals (Delanoë and Hogan, 2009, Gayet et al., 2009). IR radiometer measurements allow the retrieval of brightness temperature and cloud emissivity (Platt, 1973).

In conclusion, airborne lidar data provide an indispensable complement to other instruments for cloud studies. Closure experiments with a combination of sensors and numerical simulations are needed to improve the understanding of Arctic clouds.

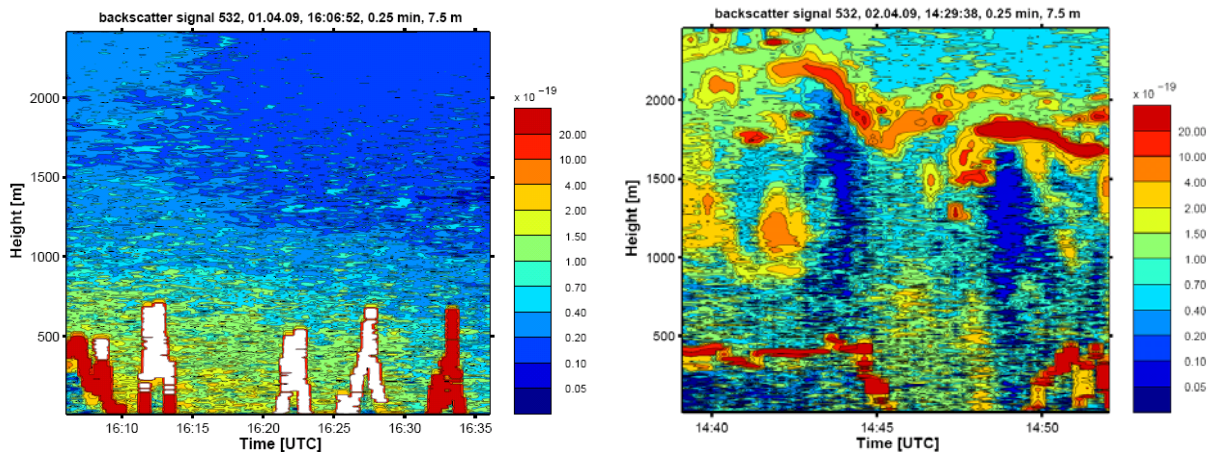


Figure 8.1: Nadir lidar backscatter measurements recorded in the surroundings of Svalbard during PAM-ARCMIP. The range-corrected signals exhibit enhanced values of backscattering in the boundary layer on 1 April 2009 (left) and complex multi-layer cloud structures on 2 April 2009 (right).

8.3 Future studies involving the AMALi

Extended airborne observations of Arctic mixed-phase clouds at low and midlevel, and of optically thin clouds are necessary for better understanding cloud processes and quantifying their radiative impact on climate. The combination of airborne lidar, spectral radiation and in situ sensors proved to be successful for cloud investigations during ASTAR 2007 (Richter et al., 2008, Ehrlich et al., 2008, 2009, Lampert et al., 2009a, 2009b, Gayet et al., 2009). As summarized in Sect. 8.1, lidar measurements served as a pathfinder to detect cloud structures of interest, and provided a direct link between the analysis of the meteorological situation and cloud observations.

The pilot study Pan-Arctic Measurements and Arctic Regional Climate Model Intercomparisons (PAM-ARCMIP) in April 2009 was a follow-up campaign of ASTAR. Spring time was chosen as during the transition time, the atmosphere is subject to large changes, including the increase in cloud cover (Key et al., 2004), influencing the melting of snow and sea ice (Zhang et al., 1996), a sudden change in aerosol properties (Ström et al., 2003) or even the formation of Arctic haze (Herber et al., 2002). These processes are difficult to represent in models due to multiple interactions and feedback mechanisms. One of the primary objectives of the campaign was to provide a data set of the Arctic on a large scale for improving regional climate modeling. Special emphasis was on northerly measurements above the Arctic Ocean, as not many atmospheric data of this remote region have been obtained. The measurement area therefore covered the western half of the Arctic from Svalbard via Greenland and Canada to Alaska with flight legs towards the North Pole above the Arctic Ocean, including also a research flight to the North Pole Drifting Station "NP36". The instrumentation on board of the Polar-5 aircraft (Basler BT-67) was designed to collect data on sea ice thickness, aerosol, trace gases and meteorological parameters. However, the observation of clouds was restricted to AMALi in nadir configuration and meteorological in situ observations, as well as vertical profiles of drop sondes. A first preliminary analysis of AMALi data revealed enhanced aerosol concentrations in the lowest 400 to 1200 m above the surface, depending on the location, and observations of optically thick boundary-layer clouds as well as complex multi-layer clouds below 3 km altitude. Examples of preliminary analyses are shown in Fig. 8.1. The raw lidar profiles were density and range corrected for a first impression of the atmospheric state, as described in Sect. 4.3. Further PAM-ARCMIP campaigns are in the planning phase.

The Solar Radiation and Phase Discrimination of Arctic Clouds (SORPIC) project, an airborne campaign from Svalbard, is scheduled for April 2010. The approved configuration of AMALi, in situ and solar radiation sensors, together with radiative transfer modeling, will be used for studying the spatial distribution of ice and liquid water in Arctic boundary layer clouds and its effects on the solar energy budget and remote sensing. Cloud formation and evolution processes will be studied above different surfaces, land, sea ice, and open water. Intersections at the edge of sea ice / open ocean are of special interest, as different dynamic features also influence cloud properties. Measurements like the observation of cloud glaciation in an air mass mixing zone on 9 April 2007 are a starting point for deeper investigations.

Further, a joint cloud observation strategy during airborne campaigns is proposed, which includes the ground-based lidar KARL in Ny-Ålesund, and the airborne AMALi and in situ sensors. The lidar KARL with three elastic wavelengths and Raman channels of water vapor and molecular nitrogen provides various parameters of interest for cloud research, namely the independent extinction coefficient and lidar ratio, further an estimation of size distribution and index of refraction by an inversion for spherical particles smaller than the lidar wavelength 1064 nm (Böckmann, 2001, Kirsche and Böckmann, 2006). In the case of observations of optically thin pre-condensation and cloud layers by the KARL lidar (Lampert et al., 2009b), airborne in situ measurements could provide valuable additional information on particle size and shape. Like that, an evaluation of the lidar retrieval of microphysical parameters is achieved, which constitutes a mathematically ill-posed problem. So far, overpasses of the aircraft above the ground-based KARL were especially performed with the aim of applying the two-stream method (Kunz, 1987, Cuesta and Flamant, 2004) using the nadir aiming AMALi and the zenith aiming KARL (Stachlewska et al., 2009). With this method, independent profiles of the extinction and backscatter coefficient were obtained with the knowledge of just two non-calibrated backscatter lidar signals in opposite directions and one backscatter value at an arbitrary altitude. No further assumptions about the lidar ratio are necessary. With this method, the lidar instrumental constant of the airborne lidar can be determined for calibrating the airborne lidar system. The two-stream method was successfully applied and reported for the first time by Stachlewska et al. (2005) for the airborne AMALi and the ground-based KARL system. In the future, the possibility of investigating also optically thin clouds by the two-stream method should be explored. However, as the success of the method critically depends on both lidar systems probing the same air (Stachlewska, 2006), small-scale cloud inhomogeneities might be challenging for the data evaluation.

In the future, the development of a new airborne lidar system at the AWI Potsdam is planned. For cloud observations, the use of the original lidar wavelength 1064 nm or even 1.57 μm would be an advantage, as more information about the large cloud particles can be retrieved from longer wavelengths. A small overlap distance is necessary for airborne applications. To reduce multiple scattering effects, a small telescope field of view is desirable. However, the use of a smaller laser divergence has to be considered carefully in the light of eye safety constraints.

8.4 Potential application in models

As mentioned in Chapt. 1, and underlined by the comparison of the airborne measurements with ECMWF data (Sect. 7.2.4), the representation of clouds in climate models needs urgent improvement. Especially properties of mixed-phase clouds cannot be reproduced adequately by one prognostic equation for the cloud condensate (e.g. Sandvik et al., 2007).

With the increasing computing capacities, it is possible to include more and complex physical cloud processes in climate models. Currently there are efforts to improve the cloud

parameterization of HIRHAM by enabling the interaction of water and ice phase particles in mixed-phase clouds (as already performed in ECHAM5, Roeckner et al., 2003). Pfeifer (2006) implemented an additional prognostic equation for cloud ice to the similar regional model REMO. This allowed the representation of microphysical processes, interactions between the cloud components liquid and ice water in the form of melting and freezing, integration of the Wegener-Bergeron-Findeisen process and different methods of precipitation formation. Further, the parameterization of convective clouds was modified to include also the typical properties of convection in cold air outbreaks. This resulted in more realistic simulations of the ice phase fraction in a climate simulation for the European climate, and improved modeling of precipitation in the case study of a North Atlantic cyclone (Pfeifer, 2006). Such an advanced cloud microphysics module is proposed to be integrated into a regional weather forecasting model like the ECMWF.

The comparison of own lidar measurements and in situ observations with ECMWF analyses (Sect. 7.2.4) demonstrated the relevance of validating model output with airborne data. The potential could be further explored in case studies after applying the implementation of a more complex cloud parameterization. Generally, data assimilation and the feeding of models with observational data obtained by satellite, airborne and ground-based measurements, as well as the intercomparison of different models with observations, are important to estimate the capabilities of models to reproduce observed atmospheric features (Inoue et al., 2006). For HIRHAM, the use of the observational data set obtained during the PAM-ARCMIP campaign is planned.

A further suggestion for improving the cloud simulations of a regional weather prediction model with advanced cloud parameterization is the implementation of CALIPSO and CloudSat data of cloud height and thermodynamic phase. CALIPSO level 2 data products provide information on cloud layer top and base altitude, midlayer temperature, integrated attenuated backscatter, integrated volume depolarization ratio, optical depth and ice water path at a horizontal resolution of 5 km along the trajectory (Anselmo et al., 2006). For the high latitudes in the Arctic, the dense data network formed by consecutive satellite overpasses can be adapted to the spatial resolution of regional climate models.

However, to accurately reproduce Arctic cloud properties for modeling activities, the knowledge gaps in the understanding of cloud processes and interactions have to be filled. Closure can only be achieved by the combination of different observational methods, radiative transfer simulations and climate modeling. Therefore, successor measurement campaigns with diverse observation and data evaluation techniques are crucial for improved results of modeling activities.

List of acronyms

AMALi	<u>A</u> irborne <u>M</u> obile <u>A</u> erosol <u>L</u> idar
ASC	<u>a</u> ngular <u>s</u> cattering <u>c</u> oefficient
ASTAR	<u>A</u> rctic <u>S</u> tudy of <u>T</u> ropospheric <u>A</u> erosol, <u>C</u> louds and <u>R</u> adiation
AVHRR	<u>A</u> dvanced <u>V</u> ery <u>H</u> igh <u>R</u> esolution <u>R</u> adiometer
AWI	<u>A</u> lfred <u>W</u> egener <u>I</u> nstitute for Polar and Marine Research
AWIPEV	<u>A</u> lfred <u>W</u> egener <u>I</u> nstitut / <u>I</u> nstitut <u>P</u> aul <u>E</u> mile <u>V</u> ictor
BASE	<u>B</u> eaufort and <u>A</u> rctic <u>S</u> torms <u>E</u> xperiment
BSR	<u>b</u> ack <u>s</u> cattering <u>r</u> atio
CALIOP	<u>C</u> loud- <u>A</u> erosol <u>L</u> idar with <u>O</u> rthogonal <u>P</u> olarization
CALIPSO	<u>C</u> loud- <u>A</u> erosol <u>L</u> idar and <u>I</u> nfrared <u>P</u> athfinder <u>S</u> atellite <u>O</u> bservations
CCN	<u>C</u> loud <u>C</u> ondensation <u>N</u> uclei
CF	<u>c</u> loud <u>f</u> orcing
CMET	<u>c</u> ontrolled <u>m</u> eteorological <u>b</u> alloon
CPI	<u>C</u> loud <u>P</u> article <u>I</u> mager
DISORT	<u>D</u> iscrete <u>O</u> rdenate
DLR	<u>D</u> eutsches Zentrum für <u>L</u> uft- und <u>R</u> aumfahrt
DOAS	<u>D</u> ifferential <u>O</u> ptical <u>A</u> bsorption <u>S</u> pectrometry
ECHAM	<u>E</u> CMWF, <u>H</u> amburg
ECMWF	<u>E</u> uropean <u>C</u> entre for <u>M</u> edium- <u>R</u> ange <u>W</u> eather <u>F</u> orecast
FIRE ACE	<u>F</u> irst <u>I</u> nternational <u>S</u> atellite <u>C</u> loud <u>C</u> limatology <u>P</u> roject <u>R</u> egional <u>E</u> xperiment <u>A</u> rctic <u>C</u> loud <u>E</u> xperiment
FOV	<u>f</u> ield of <u>v</u> iew
FSSP	<u>F</u> orward <u>S</u> cattering <u>S</u> pectrometer <u>P</u> robe
FWHM	<u>f</u> ull <u>w</u> idth at <u>h</u> alf <u>m</u> aximum
HIRHAM	<u>H</u> IRLAM + <u>E</u> CHAM
HIRLAM	<u>H</u> igh <u>R</u> esolution <u>L</u> imited <u>A</u> rea <u>M</u> odel
HYSPLIT	<u>H</u> ybrid <u>S</u> ingle- <u>P</u> article <u>L</u> agrangian <u>I</u> ntegrated <u>T</u> rajectory
ICE	<u>I</u> ntegrated <u>C</u> ooler and <u>E</u> lectronics
IFN	<u>I</u> ce <u>F</u> orming <u>N</u> uclei
IGOM	<u>I</u> mproved <u>G</u> eometric <u>O</u> ptics <u>M</u> odel
IR	<u>i</u> nfrared
ISAC	<u>I</u> stituto di <u>S</u> ienze dell' <u>A</u> tmosfera e del <u>C</u> lima
ISCCP	<u>I</u> nternational <u>S</u> atellite <u>C</u> loud <u>C</u> limatology <u>P</u> roject
ITM	<u>I</u> nstitutionen för <u>t</u> illämpad <u>m</u> iljövetenskap
IUP	<u>I</u> nstitut für <u>U</u> mwelt <u>p</u> hysik
IWC	<u>i</u> ce <u>w</u> ater <u>c</u> ontent
KARL	<u>K</u> oldewey <u>A</u> erosol <u>R</u> aman <u>L</u> idar
LAGRANTO	<u>L</u> agrangian <u>A</u> nalysis <u>T</u> ool
LaMP	<u>L</u> aboratoire de <u>M</u> étéorologie <u>P</u> hysique
libRadtran	<u>l</u> ibrary of <u>r</u> adiative <u>t</u> ransfer
lidar	<u>l</u> ight <u>d</u> etection <u>a</u> nd <u>r</u> anging
LR	<u>l</u> idar <u>r</u> atio
LW	<u>l</u> ong <u>w</u> ave
LWC	<u>l</u> iquid <u>w</u> ater <u>c</u> ontent
MISU	<u>M</u> eteorologiska <u>i</u> nstitutionen <u>S</u> tockholms <u>u</u> niversitet
MODIS	<u>M</u> oderate <u>R</u> esolution <u>I</u> maging <u>S</u> pectroradiometer
M-PACE	<u>M</u> ixed- <u>P</u> hase <u>A</u> rctic <u>C</u> loud <u>E</u> xperiment
MPL	<u>M</u> icro <u>P</u> ulse <u>L</u> idar

MSL	<u>m</u> ean <u>s</u> ea <u>l</u> evel
NAAPS	<u>N</u> avy <u>A</u> erosol <u>A</u> nalysis and <u>P</u> rediction <u>S</u> ystem
NILU	<u>N</u> orsk <u>i</u> nstitut for <u>l</u> uftforskning
NOAA	<u>N</u> ational <u>O</u> ceanic and <u>A</u> tmospheric <u>A</u> dmistration
NIPR	<u>N</u> ational <u>I</u> nstitute for <u>P</u> olar <u>R</u> esearch (Japan)
PAM-ARCMIP	<u>p</u> an- <u>A</u> rctic <u>m</u> easurements and <u>A</u> rctic <u>r</u> egional <u>c</u> limate <u>m</u> odel intercomparison
PN	<u>P</u> olar <u>N</u> ephelometer
POLARCAT	<u>P</u> olar Study using <u>A</u> ircraft, <u>R</u> emote Sensing, <u>S</u> urface Measurements and <u>M</u> odels, of <u>C</u> limate, <u>C</u> hemistry, <u>A</u> erosols, and <u>T</u> ransport
PSD	<u>p</u> article <u>s</u> ize <u>d</u> istribution
PVU	<u>p</u> otential <u>v</u> orticity <u>u</u> nit
REFLEX	<u>R</u> adiation and <u>E</u> ddy <u>F</u> lux <u>E</u> xperiment
RHI	<u>r</u> elative <u>h</u> umidity above <u>i</u> ce
SHEBA	<u>S</u> urface <u>H</u> eat <u>B</u> udget of the <u>A</u> rctic Ocean
SMART	<u>S</u> pectral <u>M</u> odular <u>A</u> irborne <u>R</u> adiation Measurement System
SNR	<u>s</u> ignal to <u>n</u> oise <u>r</u> atio
SORPIC	<u>S</u> olar <u>R</u> adiation and <u>P</u> hase <u>D</u> iscrimination of Arctic <u>C</u> louds
SW	<u>s</u> hortwave
TCP/IP	<u>T</u> ransmission <u>C</u> ontrol <u>P</u> rotocol / <u>I</u> nternet <u>P</u> rotocol
TWC	<u>t</u> otal <u>w</u> ater <u>c</u> ontent
UV	<u>u</u> ltra <u>v</u> iolet

List of symbols

α	(total) extinction coefficient		km^{-1}
α^{part}	particle extinction coefficient		km^{-1}
α^{Ray}	Rayleigh extinction coefficient		km^{-1}
β	(total) backscatter coefficient		$\text{km}^{-1} \text{sr}^{-1}$
β_{ref}	(total) backscatter coefficient at reference altitude		$\text{km}^{-1} \text{sr}^{-1}$
β_{par}	parallelly polarized backscatter coefficient		$\text{km}^{-1} \text{sr}^{-1}$
β^{part}	particle backscatter coefficient		$\text{km}^{-1} \text{sr}^{-1}$
β^{Ray}	Rayleigh backscatter coefficient		$\text{km}^{-1} \text{sr}^{-1}$
β_{perp}	perpendicularly polarized backscatter coefficient		$\text{km}^{-1} \text{sr}^{-1}$
γ	size parameter		
δ	depolarization		
Θ	potential temperature		K
Θ_0	potential temperature at ground level		K
η	shape parameter (kurtosis)		
θ	scattering angle		°
λ	wavelength		nm
μ	Ångstrom exponent		
ν	read-out frequency of lidar signal		MHz
π	circular constant	3.14	
ρ	air density		kg m^{-3}
σ	scattering cross section		m^2
σ_s	scale parameter		
τ	optical thickness		
A	area of lidar telescope		m^2
ASC	angular scattering coefficient		$\mu\text{m}^{-1} \text{sr}^{-1}$
BSR	backscattering ratio		
c	speed of light	3×10^6	m s^{-1}
C	lidar constant		
C^{part}	color ratio		
CF	cloud forcing		W m^{-2}
d	diameter		μm
F_{λ}^{\downarrow}	downwelling spectral irradiance		$\text{W m}^{-2} \text{nm}^{-1}$
F_{λ}^{\downarrow}	downwelling spectral irradiance		$\text{W m}^{-2} \text{nm}^{-1}$
$F_{\text{IR}}^{\downarrow}$	downwelling thermal infrared irradiance		W m^{-2}
F_{IR}^{\uparrow}	upwelling thermal infrared irradiance		W m^{-2}
$F_{\text{IR}}^{\text{net}}$	net (downwelling minus upwelling) thermal infrared irradiance		W m^{-2}
$F_{\text{S}}^{\downarrow}$	downwelling solar irradiance		W m^{-2}
F_{S}^{\uparrow}	upwelling solar irradiance		W m^{-2}
$F_{\text{S}}^{\text{net}}$	net (downwelling minus upwelling) solar irradiance		W m^{-2}
g_0	gravitational constant	9.81	m s^{-2}
g	asymmetry parameter		
h	Planck constant	6.63×10^{-34}	J s
I_{S}	spectral slope ice index		
I_{λ}	spectral radiance		
I_{λ}^{\downarrow}	downwelling spectral nadir radiance		$\text{W sr}^{-1} \text{m}^{-2} \text{nm}^{-1}$
I_{λ}^{\uparrow}	upwelling spectral nadir radiance		
k	Boltzmann constant	1.38×10^{-23}	J K^{-1}

LR	lidar ratio	sr
LWP	liquid water path	g m^{-2}
n	index of refraction	
N	buoyancy frequency	s^{-1}
P	backscattered laser power (lidar signal)	
P_{par}	parallelly polarized lidar signal	
P_{perp}	perpendicularly polarized lidar signal	
$P(\theta)$	phase function	
r	range	m
r_b	range at cloud bottom	m
r_t	range at cloud top	m
R	ratio of gas concentration SO_2 and NO_y	
R_{eff}	effective radius	μm
R_λ	spectral cloud top reflectivity	
s	sampling interval of lidar signal	m
S	logarithmic range-corrected lidar signal	
S_{ref}	logarithmic range-corrected lidar signal at reference altitude	
T	temperature	K
T	transmission	
z	altitude	m

References

- Allison, I., Beland, M., Alverson, K., Bell, R., Carlson, D., Danell, K., Ellis-Evans, C., Fahrbach, E., Fanta, E., Fujii, Y., Glaser, G., Goldfarb, L., Hovelsrud, G., Huber, J., Kotlyakov, V., Krupnik, I., Lopez-Martinez, J., Mohr, T., Qin, D., Rachold, V., Rapley, C., Rogne, O., Sarukhajian, E., Summerhayes, C., and Xiao, C.: The scope of science for the International Polar Year 2007/2008 . WMO/TD-No. 1364, 79 pp., 2007.
- Anderson, G., Clough, S., Kneizys, F., Chetwynd, J., and Shettle, E.: AFGL Atmospheric Constituent Profiles (0-120 km), Tech. Rep. AFGL-TR-86-0110, Air Force Geophysics Laboratory (OPI), Hanscom AFB, MA 01736, 1986.
- Anselmo, T., Clifton, R., Hunt, W., Lee, K.-P., Murray, T., Powell, T., Rodier, S.D., Vaughan, M., Chomette, O., Viollier, M., Hagolle, O., Lifermann, A., Garnier, A., Pelon, J., Currey, C., Pitts, M., and Winker, D.: Cloud – Aerosol LIDAR Infrared Pathfinder Satellite Observations, Data Management System, Data Products Catalog, Release 2.3, Document No: PC-SCI-503, 2006.
- Ansmann, A., Wandinger, U., Riebesell, M., Weitkamp, C., and Michaelis, W.: Independent measurement of extinction and backscatter profiles in cirrus clouds by using a combined Raman elastic-backscatter lidar, *Appl. Opt.*, 31, 33, 7113-7131, 1992.
- Baran, A.J., and Francis, P.N.: On the radiative properties of cirrus cloud at solar and thermal wavelengths: A test of model consistency using high-resolution airborne radiance measurements, *Q.J.R. Meteorol. Soc.*, 130, 763-778, 2004.
- Baran, A.J., and Labonnote L.-C.: On the reflection and polarisation properties of ice cloud, *J. Quant. Spectrosc. Radiat. Transfer*, 100, 41-54, 2006.
- Baran, A.J., and Labonnote L.-C.: A self-consistent scattering model for cirrus. I: The solar region, *Q.J.R. Meteorol. Soc.*, 133, 1899-1912, 2008.
- Beesley, J. A., Bretherton, C.S., Jakob, C., Andreas, E.L., Intrieri J.M., and Uttal, T.A.: A comparison of cloud and boundary layer variables in the ECMWF forecast model with observations at Surface Heat Budget of the Arctic Ocean (SHEBA) ice camp, *J. Geophys. Res.*, 105, 12337-12349, 2000.
- Bergeron, T.: On the physics of cloud and precipitation, *Proceedings 5th Assembly U.G.G.I., Lisbon, Portugal*, 156-178, 1935.
- Beyerle, G., Gross, M.R., Haner, D.A., Kjome, N.D., McDermid, I.S., McGee, T.J., Rosen, J.M., Schäfer, H.-J., and Schrems, O.: A Lidar and Backscatter Sonde Measurement Campaign at Table Mountain during February-March 1997: Observations of Cirrus Clouds, *Journal of the Atmospheric Sciences*, 58, 1275-1287, 2001.
- Bierwirth, E., Wendisch, M., Ehrlich, A., Heese, B., Tesche, M., Althausen, D., Schladitz, A., Müller, D., Otto, S., Trautmann, T., Dinter, T., von Hoyningen-Huene, W., and Kahn, R.: Spectral surface albedo over Morocco and its impact on the radiative forcing of Saharan dust, *Tellus*, 61B, 252-269, 2009.
- Bissonnette, L.R., Roy, G., and Roy, N.: Multiple-scattering-based lidar retrieval: method and results of cloud probings, *Appl. Opt.*, 44, 26, 5565-5581, 2005.
- Blanchet, J.-P., and List, R.: Estimation of optical properties of Arctic haze using a numerical model, *Atmos. Ocean* 21, 444-464, 1983.

- Böckmann, C.: Hybrid regularization method for the ill-posed inversion of multiwavelength lidar data to determine aerosol size distribution, *Appl. Opt.*, 40, 1329-1342, 2001.
- Boudala, F. S., Isaac, G. A., Cober, S. G., and Fu, Q.: Liquid fraction in stratiform mixed-phase clouds from in situ observations, *Quart. J. Roy. Meteor. Soc.*, 130, 2919–2931, 2004.
- Cadet B., Goldfarb, L., Faduilhe, D., Baldy, S., Giraud, V., Keckhut, P., and Réchou, A.: A sub-tropical cirrus clouds climatology from Reunion Island (21°S, 55°E) lidar data set, *GRL* 30, 3, 1130, doi:10.1029/2002GL016342, 2003.
- Cadet, B., Giraud, V., Haeffelin, M., Keckhut, P., Réchou, A., and Baldy, S.: Improved retrievals of the optical properties of cirrus clouds by a combination of lidar methods, *Appl. Opt.*, 44, 9, 1726-1734, 2005.
- Campbell, J.R., and Shiobara, M.: Glaciation of a mixed-phase boundary layer cloud at a coastal arctic site as depicted in continuous lidar measurements, *Polar Science* 2, 121-127, 2008.
- Chen, W.N., Chiang, C.W., and Nee, J.B.: Lidar ratio and depolarisation ratio for cirrus clouds, *Appl. Opt.*, 31, 6470-6476, 2002.
- Chen, C.C., Hakim, G.J., and Durran, D.R.: Transient mountain waves and their interaction with large scales, *J. Atmos. Scie.*, 64, 7, 2378-2400, 2007.
- Christensen, J.H., Christensen, O.B., Lopez, P., van Mijgaard, E., and Botzet, M.: The HIRHAM4 regional atmospheric climate model, *DMI Science Rep.* 96-4, 1-51, 1996.
- Corell, R.: *Arctic Climate Impact Assessment*, Cambridge University Press, Cambridge, UK, 139 pp., 2004.
- Cuesta J., and Flamant, P.H.: Two-stream lidar inversion algorithm for airborne and satellite validations, in *Proceedings of 22nd International Laser Radar Conference (ILRC 2004)*, G. Pappalardo and A. Amodeo, eds., ESA SP-561 1, 471-474, 2004.
- Curry, J.A., and Ebert, E.E.: Annual Cycle of Radiation Fluxes over the Arctic Ocean: Sensitivity to Cloud Optical Properties, *Journal of Climate*, 5, 1267-1280, 1992.
- Curry, J.A., Schramm, J.L., Ebert, E.E., Impact of Clouds on the Surface Radiation Balance of the Arctic Ocean, *Meteorol. Atmos. Phys.* 51, 197-217, 1993.
- Curry, J.A., Rossow, W.B., Randall, D., and Schramm, J.L.: Overview of Arctic Cloud and Radiation Characteristics, *Journal of Climate*, 9, 1731-1764, 1996.
- Curry, J.A., Pinto, J.O., Benner, T., Tschudi, M., Evolution of the cloudy boundary layer during the autumnal freezing of the Beaufort Sea, *J. Geophys. Res.*, 102, D12, 13851-13860, 1997.
- Curry, J.A., Hobbs, P.V., King, M.D., Randall, D.A., Minnis, P., Isaac, G.A., Pinto, J.O., Uttal, T., Bucholtz, A., Cripe, D.G., Gerber, H., Fairall, C.W., Garrett, T.J., Hudson, J., Intrieri, J.M., Jakob, C., Jensen, T., Lawson, P., Marcotte, D., Nguyen, L., Pilewskie, P., Rangno, A., Rogers, D.C., Strawbridge, K.B., Valero, F.P.J., Williams, A.G., and Wylie, D.: FIRE Arctic Clouds Experiment, *Bulletin Am. Meteorolog. Soc.*, 81, 1, 5-29, 2000.
- Davis, K.J., Gamage, N., Hagelberg, C.R., Kiemle, C., Lenschow, D.H., and Sullivan, P.P.: An Objective Method for Deriving Atmospheric Structure from Airborne Lidar Observations, *J. Atmos. Ocean. Technol.*, 17, 1455-1468, 2000.
- Delanoë, J., and Hogan, R.J.: Combined CloudSat-CALIPSO-MODIS retrievals of the properties of ice clouds, submitted to *J. Geophys. Res.*, 2009.

- Dye, J. E., and Baumgardner, D.: Evaluation of the Forward Scattering Spectrometer Probe. Part I: Electronic and optical studies, *J. Atmos. Oceanic Technol.*, 1, 329–344, 1984.
- Engvall, A.-C., Krejci, R., Ström, J., Minikin, A., Treffeisen, R., Stohl, A., and Herber, A.: In-situ airborne observations of the microphysical properties of the Arctic tropospheric aerosol during late spring and summer, accepted to *Tellus B*, 2008.
- Ehrlich, A., Bierwirth, E., Wendisch, M., Gayet, J.-F., Mioche, G., Lampert, A., and Heintzenberg, J.: Cloud phase identification of Arctic boundary-layer clouds from airborne spectral reflection measurements: test of three approaches, *Atmos. Chem. Phys.*, 8, 7493-7505, 2008.
- Ehrlich, A., Wendisch, M., Bierwirth, E., Gayet, J.-F., Mioche, G., Lampert, A., and Mayer, B.: Evidence of ice crystals at cloud top of Arctic boundary-layer mixed-phase clouds derived from remote sensing, *Atmos. Chem. Phys. Discuss.*, 9, 13801–13842, 2009.
- Findeisen, W.: Kolloidmeteorologische Vorgänge bei Niederschlagsbildung, *Meteor.Z.*, 55, 121-133, 1938.
- Flamant, C., Pelon, J., Flamant, P.H., Durand, P.: Lidar determination of the entrainment zone thickness at the top of the unstable marine atmospheric boundary layer, *Boundary-Layer Meteorology*, 83, 247–284, 1997.
- Fleishauer, R.P., Larson, V.E., and Vonder Haar, T.H.: Observed Microphysical Structure of Midlevel, Mixed-Phase Clouds, *J. American Meteorological Society*, 1779-1804, 2001.
- Francis, P.N., Foot, J.S., and Baran A.J.: Aircraft measurements of the solar and infrared radiative properties of cirrus and their dependence on ice crystal shape, *J. Geophys. Res.*, 104, 31685-31696, 1999.
- Frey, R.A., Baum, B.A., Menzel, W.P., Ackermann, S.A., Moeller, C.C., and Spinhirne, J.D.: A comparison of cloud top heights computed from airborne lidar and MAS radiance data using CO₂ slicing, *J. Geophys. Res.*, 104, D20, 24,547–24,555, 1999.
- Fridlind, A.M., Ackermann, A.S., McFarquhar, G., Zhang, G., Poellot, M.R., DeMott, P.J., Prenni, A.J., and Heymsfield, A.J.: Ice properties of single-layer stratocumulus during the Mixed-Phase Arctic Cloud Experiment: 2. Model results, *J. Geophys. Res.*, 112, D2402, doi:10.1029/2007JD008646, 2007.
- Gayet, J.-F., Crépel, O., Fournol, J.F., and Oshchepkov, S.: A new airborne polar Nephelometer for the measurements of optical and microphysical cloud properties. Part I: Theoretical design, *Ann. Geophys.*, 15, 451-459, 1997.
- Gayet, J.-F., Shcherbakov, V. N., Mannstein, H., Minikin, A., Schumann, U., Ström, J., Petzold, A., Ovarlez, J., and Immler, F.: Microphysical and optical properties of midlatitude cirrus clouds observed in the southern hemisphere during INCA, *Quart. J. Roy. Meteor. Soc.*, 132, 621, 2719-2748, 2006.
- Gayet J.-F., Stachlewska, I.S., Jourdan, O., Shcherbakov, V., Schwarzenboeck, A., and Neuber, R.: Microphysical and optical properties of precipitating drizzle and ice particles obtained from alternated Lidar and in situ measurements, *Annales Geophys.*, 25, 1487-1497, 2007.
- Gayet, J.-F., Mioche, G., Dörnbrack, A., Ehrlich, A., Lampert, A., and Wendisch, M.: Microphysical and optical properties of Arctic mixed-phase clouds – the 9 April 2007 case study, *Atmos. Chem. Phys. Discuss.*, 9, 11333-11366, 2009.
- Garrett, T.J., Hobbs, P.V., and Gerber, H.: Shortwave, single-scattering properties of arctic ice clouds, *J. Geophys. Res.*, 106, D14, 15155-15172, 2001.

- Garrett, T.J., Zhao, C., Dong, X., Mace, G.C., and Hobbs, P.V.: Effects of varying aerosol regimes on low-level Arctic stratus, *Geophys. Res. Lett.*, 31, L17105, doi:10.1029/2004GL019928, 2004.
- Garrett, T.J., and Zhao, C.: Increased Arctic cloud longwave emissivity associated with pollution from mid-latitudes, *Nature*, 440, doi:10.1038/nature04636, 787-789, 2006.
- Giannakaki, E., Balis, D.S., Amiridis, V., and Kazadzis, S.: Optical and geometrical characteristics of cirrus clouds over a mid-latitude lidar station, *Atmos. Chem. Phys.*, 7, 5519-5530, 2007.
- Gore, A.: *An Inconvenient Truth: the planetary emergency of global warming and what we can do about it*, Melcher Media, ISBN 1594865671, 9781594865671, 325 pp., 2006.
- Gultepe, I., Isaac, G., Hudak, D., Nissen, R., and Strapp, J.W.: Dynamical and Microphysical Characteristics of Arctic Clouds during BASE, *J. of Climate*, 13, 1225-1254, 2000.
- Hallar, A.G., Avallone, L.M., Herman, R.L., Anderson, B.E., and Heymsfield, A.J.: Measurements of ice water content in tropopause region Arctic cirrus during the SAGE III Ozone Loss and Validation Experiment (SOLVE), *J. Geophys. Res.*, 109, D17203, doi:10.1029/2003JD004348, 2004.
- Hara, K., Yamagata, S., Yamanouchi, T., Sato, K., Herber, A., Iwasaka, Y., Nagatani, M., and Nakata, H.: Mixing states of individual aerosol particles in spring Arctic troposphere during ASTAR 2000 campaign, *J. Geophys. Res.*, 108, D7, 4209, doi:10.1029/2002JD002513, 2003.
- Harrington, J.Y., Reisin, T., Cotton, W.R., and Kreidenweis, S.M.: Cloud resolving simulations of Arctic stratus, Part II: Transition-season clouds, *Atmospheric Research*, 51, 45-75, 1999.
- Hartmann, J., Bochert, A., Freese, D., Kottmeier, C., Nagel, D., and Reuter, A.: Radiation and Eddy Flux Experiment 1995 (Reflex III), *Reports Pol. Res.*, 218, ISSN 0176-5027, 74 pp., 1997.
- Herber, A., Thomason, L.W., Gernandt, H., Leiterer, U., Nagel, D., Schulz, K.-H., Kaptur, J., Albrecht, T., and Notholt, J.: Continuous day and night aerosol optical depths observations in the Arctic between 1991 and 1999, *J. Geophys. Res.* 107, D10, 4097, doi 10.1029/2001JD000536, 2002.
- Herman G.F., and Goody, R.: Formation and persistence of summertime Arctic stratus clouds, *J. Atmos. Sci.*, 33, 1537-1553, 1976.
- Heymsfield, A. J.: On measurements of small ice particles in clouds, *Geophys. Res. Lett.*, 34, doi:10.1029/2007GL030951, 2007.
- Hobbs, P.V., and Rangno, A.L.: Microstructures of low and middle-level clouds over the Beaufort Sea, *Q.J.R.Meteorol.Soc.*, 124, 2035-2071, 1998.
- Hobbs, P.V., Rangno, A.L., Shupe, M., and Uttal, T.: Airborne studies of cloud structures over the Arctic Ocean and comparison with retrievals from ship-based remote sensing measurements, *J. Geophys. Res.*, 106, D14, 15029-15044, 2001.
- Hoffmann, A., Ritter, C., Stock, M., Shiobara, M., Lampert, A., Maturilli, M., Orgis, T., Neuber, R., and Herber, A.: Ground-based lidar measurements from Ny-Ålesund during ASTAR 2007: A statistical overview, *Atmos. Chem. Phys. Discuss.*, 9, 15453–15510, 2009.
- Houze, R.A.: *Cloud dynamics*, Academic Press, San Diego, London, ISBN 0-12-356881-1, 1993.

Hu, Y., Winker, D., Yang, P., Baum, B., Poole, L., and Vann, L.: Identification of cloud phase from PICASSO-CENA lidar depolarization: a multiple scattering sensitivity study, *J. Quantitative Spectroscopy & Radiative Transfer*, 70, 569-579, 2001.

Hu, Y., Liu, Z., Winker, D., Vaughan, M., and Noel, V.: Simple relation between lidar multiple scattering and depolarization for water clouds, *Optics Letters*, 31, 12, 1809-1811, 2006.

Hu, Y., Vaughan, M., Liu, Z., Lin, B., Yang, P., Flittner, D., Hunt, B., Kuehn, R., Huang, J., Wu, D., Rodier, S., Powell, K., Trepte, C., and Winker, D.: The depolarization - attenuated backscatter relation: CALIPSO lidar measurements vs. theory, *Optics Express*, 15, 9, 5327-5332, 2007.

Immler, F., and Schrems, O.: Lidar observations of extremely thin clouds at the tropical tropopause, Reviewed and revised papers presented at the 23rd International Laser Radar conference 24-28 July 2006, Nara, Japan, Editors: Chikao Nagasawa, Nobuo Sugimoto, 547-550, 2006.

Immler, F., Krüger, K., Fujiwara, M., Verver, G., Rex, M., and Schrems, O.: Correlation between equatorial Kelvin waves and the occurrence of extremely thin ice clouds at the tropical tropopause, *Atmospheric Chemistry and Physics*, 8, 4019-4026, 2008.

Inoue, J., Liu, J., Pinto, J.O., and Curry, J.A.: Intercomparison of Arctic Regional Climate Models: Modeling Clouds and Radiation for SHEBA in May 1998, *Journal of Climate*, 19, 4167-4178, 2006.

Intrieri, J.M., Shupe, M.D., Uttal, T., and McCarty, B.J.: An annual cycle of Arctic cloud characteristics observed by radar and lidar at SHEBA, *J. Geophys. Res.*, 107, C10, 8030, doi:10.1029/2000JC000423, 2002a.

Intrieri, J.M., Fairall, C.W., Shupe, M.D., Persson, P.O.G., Andreas, E.L., Guest, P.S., and Moritz, R.E.: An annual cycle of Arctic surface cloud forcing at SHEBA, *J. Geophys. Res.*, 107, C10, 8039, doi:10.1029/2000JC000439, 2002b.

Intrieri, J.M., and Shupe, M.D.: Characteristics and radiative effects of diamond dust over the western Arctic Ocean region, *J. Climate*, 17 (15), 2953-2960, 2004.

IPCC, Intergovernmental Panel on Climate Change: Climate Change 2007: The Physical Science Basis. Contribution of Working Group I to the Fourth Assessment Report of the Intergovernmental Panel on Climate Change, Solomon, S., Qin, D., Manning, M., Chen, Z., Marquis, Z.M., Averyt, K.B., Tignor M., and Miller, H.L. (eds.), Cambridge University Press, 996 pp., 2007.

Jiang, H., Cotton, W.R., Pinto, J.O., Curry, J.A., and Weissbluth, M.J.: Cloud Resolving Simulations of Mixed-Phase Arctic Stratus Observed during BASE: Sensitivity to Concentration of Ice Crystals and Large-Scale Heat and Moisture Advection, *J. of the Atmospheric Sciences*, 57, 2105-2117, 2000.

Jourdan, O., Oshchepkov, S., Gayet, J.-F., Shcherbakov, V. N., and Isaka, H.: Statistical analysis of cloud light scattering and microphysical properties obtained from airborne measurements, *J. Geophys. Res.*, 108, D5, 4155, doi:10.1029/2002JD002723 (AGU), 2003a.

Jourdan, O., Oshchepkov, S., Shcherbakov, V., Gayet, J.-F., and Isaka, H.: Assessment of cloud optical parameters in the solar region: Retrievals from airborne measurements of scattering phase functions, *J. Geophys. Res.*, 108, D18, 4572, doi:10.1029/2003JD003493, 2003b.

- Kay, J.E., L'Ecuyer, T., Gettelman, A., Stephens, G., and O'Dell, C.: The contribution of cloud and radiation anomalies to the 2007 Arctic sea ice extent, *Geophys. Res. Lett.*, 35, L08503, doi:10.1029/2008GL033451, 2008.
- Key, J. R., Yang, P., Baum, B. A., and Nasiri, S. L.: Parameterization of shortwave ice cloud optical properties for various particle habits, *J. Geophys. Res-Atmos.* 107 (D13), Art. No. 4181., doi:10.1029/2001JD000742, 2002.
- Key, E.L., Minnett, P.J., and Jones, R.A.: Cloud distributions over the coastal Arctic Ocean: surface-based and satellite observations, *Atmospheric Research*, 72, 57-88, 2004.
- Kiehl, J.T., and Trenberth, K.E.: Earth's Annual Global Mean Energy Budget, *Bull. Amer. Meteor. Soc.*, 78, 197-208, 1997.
- King, M.D., Platnick, S., Yang, P., Arnold, G.T., Gray, M.A., Riedi, J.C., Ackerman, S.A., and Liou, K.-N.: Remote Sensing of Liquid Water and Ice Cloud Optical Thickness and Effective Radius in the Arctic: Application of Airborne Multispectral MAS Data, *J. Atmos. Ocean. Technol.*, 21, 857-875, 2004.
- Kirsche, A., and Böckmann, C.: Pade iteration method for regularization, *Appl. Math. Comput.*, 180, 648-663, 2006.
- Klett, J.D.: Stable analytical inversion solution for processing lidar returns, *Appl. Opt.* 20, 211-220, 1981.
- Klett, J.D.: Lidar inversions with variable backscatter/extinction values, *Appl. Opt.*, 24, 1638-1648, 1985.
- Korolev, A., and Field, P. R.: The effect of dynamics on mixed-phase clouds: Theoretical considerations, *J. Atmos. Sci.*, 65, 66-86, 2008.
- Korolev, A., and Isaac, G.: Phase transformation of mixed-phase clouds, *Q.J.R. Meteorol. Soc.* 129, 19-38, 2003.
- Korolev, A., and G. A. Isaac: Shattering during sampling by OAPs and HVPS. Part I: Snow particles, *J. Atmos. Oceanic Technol.*, 22, 528-543, 2005.
- Korolev, A. V., Isaac, G. A., Cober, S. G., Strapp, J.W., and Hallett, J.: Microphysical characterization of mixed-phase clouds, *Quart. J. Roy. Meteor. Soc.*, 129, 39–65, 2003.
- Korolev, A.V., and Mazin, I.P.: Supersaturation of Water Vapor in Clouds, *J. Atmos. Scie.*, 60, 2957-2974, 2003.
- Kunz, G.J.: Biphase method as a way to measure the spatial backscatter and extinction coefficients with lidar, *Appl. Opt.* 26, 794-795, 1987.
- Kunz, G., and de Leeuw, G.: Inversion of lidar signals with the slope method, *Appl. Opt.*, 32, 18, 3249-3256, 1993.
- Kupfer, H., Herber, A., and König-Langlo, G.: Radiation Measurements and Synoptic Observations at Ny-Ålesund, *Reports on Polar Research*, 538, 75, <http://epic.awi.de/Publications/Kup2006a.pdf>, 2006.
- Labonnote, L.-C., Brogniez, G., Buriez, J-C., Doutriaux-Boucher M., Gayet, J-F., and Macke, A: Polarized light scattering by inhomogeneous hexagonal monocrystals : Validation with ADEOS-POLDER measurements, *J. Geophys. Res.*, 106, 12139-12154, 2001.
- Lampert, A., Ehrlich, A., Dörnbrack, A., Jourdan, O., Gayet, J.-F., Mioche, G., Shcherbakov, V., Ritter, C., and Wendisch, M.: Microphysical and Radiative Characterization of a

- Subvisible Midlevel Arctic Ice Cloud by Airborne Observations - A Case Study, *Atmos. Chem. Phys.*, 9, 2647-2661, 2009a.
- Lampert, A., Ritter, C., Hoffmann, A., Gayet, J.-F., Mioche, G., Ehrlich, A., Dörnbrack, A., Wendisch, M., and Shiobara, M.: Observations of Boundary Layer, Mixed-Phase and Multi-Layer Arctic Clouds with different lidar systems during ASTAR 2007, *Atmos. Chem. Phys. Discuss.*, 9, 15125–15179, 2009b.
- Law, K.S., Ancellet, G., Pelon, J., Turquety, S., Clerbaux, C., Pommier, M., de Villiers, R., Gayet, J.-F., Schwarzeboeck, A., Nedelec, P., Schneider, J., and Borrmann, S.: POLARCAT-France Airborne Experiment: first results. /Intern. Global Atmospheric Chemistry conference (IGAC)/, 7-12 September 2008, Annecy, France, 2008.
- Lawson, P., Heymsfield, A.J., Aulenbach, S.M., and Jensen, T.L.: Shapes, sizes and light scattering properties of ice crystals in cirrus and a persistent contrail during SUCCES, *Geophys. Res. Lett.*, 25, 1331-1334, 1998.
- Lawson, R.P., Baker, B.A., Schmitt, C.G., and Jensen, T.L.: An overview of microphysical properties of Arctic clouds observed in May and July 1998 during FIRE ACE, *J. Geophys. Res.*, 106, D14, 14989-15014, 2001.
- Liu, L., and Mishchenko, M.I.: Constraints on PSC particle microphysics derived from lidar observations, *J. Quantitative Spectroscopy & Radiative Transfer*, 70, 817-831, 2001.
- Lohmann U., and Feichter, J.: Global indirect aerosol effects: a review, *Atmos. Chem. Phys.*, 5, 715-737, 2005.
- Luo, Y., Xu, K.-M., Morrison, H., and McFarquhar, G.: Arctic Mixed-Phase Clouds Simulated by a Cloud-Resolving Model: Comparison with ARM Observations and Sensitivity to Microphysics Parameterizations, *J. Atmos. Sciences*, 65, 1285-1303, 2008.
- Masuda, K., Kobayashi, T., Raschke, E., Albers, F., Koch, W., and Maixner, U.: Short-wave radiation flux divergence in Arctic cirrus: a case study, *Atmos. Res.*, 53, 251-267, 2000.
- Mayer, B., and Kylling, A.: Technical note: The libRadtran software package for radiative transfer calculations – description and examples of use, *Atmos. Chem. Phys.*, 5, 1855–1877, 2005.
- McFarquhar, G.M., and Cober, S.G.: Single Scattering Properties of Mixed Phase Arctic Clouds at Solar Wavelengths: Impact on radiative transfer, *Jour. of Climate*, 17, 19, 3799-3813, 2004.
- McFarquhar, G.M., Zhang, G., Poellot, M.R., Kok, G.L., McCoy, R., Tooman, T., Fridlind, A.M., Heymsfield, A.J.: Ice properties of single-layer stratocumulus during the Mixed-Phase Arctic Cloud Experiment: 1. Observations, *J. Geophys. Res.*, 112, D24201, doi:10.1029/2007JD008633, 2007.
- McGill, M.J., Hlavka, D.L., Hart, W.D., Welton, E.J., and Campbell, J.R.: Airborne lidar measurements of aerosol optical properties during SAFARI-2000, *J. Geophys. Res.*, 108, D13, 8493, doi:10.1029/2002JD002370, 2003.
- McGill, M. J., Vaughan, M.A., Trepte, C.R., Hart, W.D., Hlavka, D.L., Winker, D.M, and Kuehn, R.: Airborne validation of spatial properties measured by the CALIPSO lidar, *J. Geophys. Res.*, 112, D20201, doi:10.1029/2007JD008768, 2007.
- McInnes, K.L., and Curry, J.A.: Modeling the mean and turbulent structure of the summertime Arctic cloudy boundary layer, *Bound.-Layer Meteor.*, 73, 125-143, 1995.
- Melles Griot, Interference Filters (<http://www.mellesgriot.com/pdf/0013.25-13.29.pdf>), 2004.

- Mioche, G., Josset, D., Gayet, J.-F., Pelon, J., Garnier, A., Minikin, A., and Schwarzenboeck, A.: Validation of the CALIPSO/CALIOP extinction coefficients from in situ observations in mid-latitude cirrus clouds during CIRCLE-2 experiment, submitted to *J. Geophys. Res.*, 2009.
- Mishchenko, M.I., Wieland, D.J., and Carlson, B.E.: T-matrix computations of zenith-enhanced lidar backscatter from horizontally oriented ice plates, *Geophys. Res. Lett.*, 24, 7, 771-774, 1997.
- Morrison, H., Pinto, J. O., Curry, J. A., and McFarquhar, G. M.: Sensitivity of modeled Arctic mixed-phase stratocumulus to cloud condensation and ice nuclei over regionally varying surface conditions, *J. Geophys. Res.*, 113, D05203, doi:10.1029/2007JD008729, 2008.
- Nakajima, T. and King, M.: Determination of the optical thickness and effective particle radius of clouds from reflected solar radiation measurements. Part I: Theory, *J. Atmos. Sci.*, 47, 1878-1893, 1990.
- Nghiem, S., Rigor, I., Perovich, D., Clemente-Colon, P., Weatherly, J., and Neumann, G.: Rapid reduction of Arctic perennial sea ice, *Geophys. Res. Lett.*, 34, L19504, doi:10.1029/2007GL031138, 2007.
- Nicolas, F., Bissonnette, L.R., and Flamant, P.H.: Lidar effective multiple-scattering coefficients in cirrus clouds, *Appl. Opt.*, 36, 15, 3458-3468, 1997.
- Oshchepkov, S.L., Isaka, H., Gayet, J.F., Sinyuk, A., Auriol, F., and Havemann, S.: Microphysical properties of mixed-phase & ice clouds retrieved from in situ airborne "Polar Nephelometer" measurements, *Geophys. Res. Lett.*, 27, 209-213, 2000.
- Pal, S.R., and Carswell, A.I.: Polarization Properties of Lidar Backscattering from Clouds, *Appl. Opt.*, 12, 7, 1530-1535, 1973.
- Peter, T., Luo, B.P., Wirth, M., Kiemle, C., Flentje, H., Yushkov, V.A., Khattatov, V., Rudakov, V., Thomas, A., Borrmann, S., Toci, G., Mazzinghi, P., Beuermann, J., Schiller, C., Cairo, F., Di Donfrancesco, G., Adriani, A., Volk, C.M., Strom, J., Noone, K., Mitev, V., MacKenzie, R.A., Carslaw, K.S., Trautmann, T., Santacesaria, V. and Stefanutti, L.: Ultrathin Tropical Tropopause Clouds (UTTCS): I. Cloud morphology and occurrence, *Atmos. Chem. Phys.*, 3, 1083-1091, 2003.
- Pfeifer, S.: Modeling cold cloud processes with the regional climate model REMO, PhD thesis, Reports on Earth System Science, 23, 2006.
- Pinto, J.O.: Autumnal Mixed-Phase Cloudy Boundary Layers in the Arctic, *J. Atmos. Sci.*, 55, 2016-2037, 1998.
- Pinto, J.O., Curry, J.A., and Intrieri, J.M.: Cloud-aerosol interactions during autumn over Beaufort Sea, *J. Geophys. Res.*, 106, D14, 15077-15097, 2001.
- Platt, C.M.R.: Lidar and Radiometric Observations of Cirrus Clouds, *J. Atmos. Sci.*, 30, 1191-1204, 1973.
- Platt, C.M.R.: Lidar Observation of a Mixed-Phase Altostratus Cloud, *J. Appl. Meteorol.*, 16, 339-345, 1977.
- Prahl, S.: Mie Scattering Calculator, http://omlc.ogi.edu/calc/mie_calc.html, 2007.
- Quante, M., Lemke, H., Flentje, H., Francis, P., and Pelon, J.: Boundaries and Internal Structure of Mixed Phase Clouds as Deduced from Ground-Based 95GHz Radar and Airborne Lidar Measurements, *Phys. Chem. Earth (E)*, 25, 10-12, 889-895, 2000

- Quinn, P.K., Shaw, G., Andrews, E., Dutton, E.G., Ruoho-Airola, T., and Gong, S.L.: Arctic haze: Current trends and knowledge gaps, *Tellus*, 59B, 99-114, 2007.
- Ramanathan, V., Cess, R.D., Harrison, E.F., Minnis, P., Barkstrom, B.R., Ahmad, E., and Hartmann, D.: Cloud-Radiative Forcing and Climate: Results from the Earth Radiation Budget Experiment, *Science*, 243, 57-63, 1989.
- Rangno, A.L., and Hobbs, P.V.: Ice particles in stratiform clouds in the Arctic and possible mechanisms for the production of high ice concentrations,” *J. Geophys. Res.*, 106, D14, 15065-15075, 2001.
- Rauber, R.M., and Tokay, A.: An Explanation for the Existence of Supercooled Water at the Top of Cold Clouds, *J. Atmos. Sciences*, 48, 8, 1005-1023, 1991.
- Ricchiazzi, P., Yang, S., Gautier, C. and Sowle, D.: SBDART: a research and teaching software tool for plane-parallel radiative transfer in the Earth’s atmosphere, *Bull. Am. Meteorol. Soc.*, 79, 2101–2114, 1998.
- Richter A., Gayet, J.-F., Mioche, G., Ehrlich, A., and Dörnbrack, A.: Mixed-Phase Clouds in the Arctic: A Synopsis of Airborne Lidar, In-Situ, and Albedometer Observations, complemented by Meteorological Analyses, 24th International Laser Radar Conference (ILRC), 23 – 27 June 2008, Boulder, USA, 881-884, 2008.
- Rinke, A., Dethloff, K., and Fortmann, M.: Regional climate effects of Arctic Haze, *Geophys. Res. Lett.*, 31, L16202, doi:10.1029/2004GL020318, 2004.
- Ritter, C., Kirsche, A., and Neuber, R.: Tropospheric Aerosol characterized by a Raman Lidar over Spitsbergen, Reviewed and revised papers presented at the 22nd International Laser Radar Conference (ILRC 2004) : 12 - 16 July 2004, Matera, Italy / European Space Agency. Gelsomina Pappalardo, ed. Noordwijk : ESA Publications Div., 459-462, 2004.
- Roeckner, E., Bäuml, G., Bonaventura, L., Brokopf, R., Esch, M., Giorgetta, M., Hagemann, S., Kirchner, I., Kornblueh, L., Manzini, E., Rhodin, A., Schlese, U., Schulzweida, U., and Tompkins, A.: The atmospheric general circulation model ECHAM 5. PART I: Model description, Max-Planck-Institut für Meteorologie, Report No. 349, 2003.
- Rogers, D.C., DeMott, P.J., and Kreidenweis, S.M.: Airborne measurements of tropospheric ice-nucleating aerosol particles in the Arctic spring, *J. Geophys. Res.*, 106, D14, 15053-15063, 2001.
- Rossow, W. B., Walker, A., Beuschel, D., and Roiter, M.: International Satellite Cloud Climatology Project (ISCCP) Documentation of Cloud Data. World Climate Research Programme, NASA, Goddard Institute of Space Studies, 115 pp, 1996.
- Rother, T., Schmidt, K., Wauer, J., Shcherbakov, V., and Gayet, J.-F.: Light scattering on Chebyshev particles of higher order, *Appl. Opt.* 45, 6030-6037, 2006.
- Sandvik, A., Biryulina, M., Kvamstø, N.G., Stamnes J.J., and Stamnes, K.: Observed and simulated composition of Arctic clouds: Data properties and model validation, *J. Geophys. Res.*, 112, doi:10.1029/2006JD007351, 2007.
- Sasano, Y., Browell, E.V., and Ismail, S.: Error caused by using a constant extinction/backscattering ratio in the lidar solution, *Appl. Opt.* 24, 3929-3932, 1985.
- Sassen, K., Griffin, M.K., and Dodd, G.C.: Optical Scattering and Microphysical Properties of Subvisual Cirrus Clouds, and Climatic Implications, *J. Appl. Meteorol.*, 28, 91-98, 1989.
- Sassen, K.: The Polarization Lidar Technique for Cloud Research: A Review and Current Assessment, *Bulletin American Meteorological Society*, 72, 12, 1848-1866, 1991.

- Sassen, K., and Comstock, J.M.: A midlatitude cirrus cloud climatology from the facility for atmospheric remote sensing. Part III: Radiative properties, *J. Atmos. Sci.*, 58, 2113-2127, 2001.
- Scheuer, E., Talbot, R.W., Dibb, J.E., Seid, G.K., and DeBell, L.: Seasonal distributions of fine aerosol sulfate in the North American Arctic basin during TOPSE, *J. Geophys. Res.* 108, D4, 8370 doi 10.1029/2001JD001364, 2003.
- Schweiger, A.J., Lindsay, R.W., Key, J.R., and Francis, J.A.: Arctic Clouds in Multiyear Satellite Data Sets, *J. Geophys. Res.*, 26, 13, 1845-1848, 1999.
- Shaw, G.E.: Evidence for a Central Eurasian source area of Arctic haze in Alaska, *Nature*, 299, 815-818, 1982.
- Shcherbakov, V. N., Gayet, J.-F., Jourdan, O., Minikin, A., Ström, J., and Petzold, A.: Assessment of Cirrus Cloud Optical and Microphysical Data Reliability by Applying Statistical Procedures, *J. Atmos. Ocean. Technol.*, 22, 4, 409-420, 2005.
- Shcherbakov, V.N, Gayet, J.-F, Baker, B., and Lawson, P.: Light Scattering by Single Natural Ice crystals, *Journal of the Atmospheric Sciences*, 63, 1513-1525, 2006.
- Shettle, E.: Comments on the use of LOWTRAN in transmission calculations for sites with the ground elevated relative to sea level, *Appl. Opt.*, 28, 1451-1452, 1989.
- Shiobara, M., Yabuki, M., Kobayashi, H.: A polar cloud analysis based on Micro-pulse Lidar measurements at Ny-Alesund, Svalbard and Syowa, Antarctica, *Phys. and Chem. of the Earth*, 28, 1205-1212, 2003.
- Shiobara, M., Yabuki, M., Neuber, R., Spinhirne, J.D., Welton, E.J., Campbell, J.R., Hart, W.D., Berkoff, T.A.: Arctic experiment for ICESat/GLAS ground validation with a Micro-Pulse Lidar at Ny-Ålesund, Svalbard, *Polar Meteorol. Glaciol.*, 20, 28-39, 2006.
- Shupe, M.D., and Intrieri, J.M.: Cloud radiative forcing of the Arctic surface: The influence of cloud properties, surface albedo and solar zenith angle, *J. Climate*, 17, 616-628, 2004.
- Shupe, M., Uttal, T., and Matrosov, S.Y.: Arctic Cloud Microphysics Retrievals from Surface-Based Remote Sensors at SHEBA, *J. Appl. Meteorol.*, 44, 1544-1562, 2005.
- Shupe, M.D., Kollias, P., Persson, P.O.G., McFarquhar, G.M., Vertical Motions in Arctic Mixed-Phase Stratiform Clouds, *J.A.S.*, 65, pp. 1304-1322, 2008.
- Sirois, A., and Barrie, L.A.: Arctic lower tropospheric aerosol trends and composition at Alert, Canada: 1980-1995, *J. Geophys. Res.*, 104, D9, 11599-11618, 1999.
- Spichtinger, P., Gierens, K. and Dörnbrack, A.: Formation of ice supersaturation by mesoscale gravity waves, *Atmos. Chem. Phys.*, 5, 1243-1255, 2005.
- Spinhirne, J.D.: Micro pulse lidar, *IEEE Trans. Geosci. Remote Sens.*, 31, 48-55, 1993.
- Spreen, G., Kaleschke, L. and Heygster, G.: Sea ice remote sensing using AMSR-E 89 GHz channels, *J. Geophys. Res.*, doi:10.1029/2005JC003384, 2008.
- Stachlewska, I.S., Wehrle, G., Stein, B., and Neuber, R.: Airborne Mobile Aerosol Lidar for measurements of Arctic aerosols, *Proceedings of 22nd International Laser Radar Conference (ILRC2004)*, ESA SP-561, 1, 87-89, 2004.
- Stachlewska, I. S., Ritter, C., and Neuber, R.: Application of the two-stream inversion algorithm for retrieval of extinction, backscatter, and lidar ratio for clean and polluted Arctic air, *Proceedings of SPIE*, 5984, 15-22, 2005.

- Stachlewska I.S., Investigation of tropospheric arctic aerosol and mixed-phase clouds using airborne lidar technique, PhD Thesis, University of Potsdam, 100 pp., (<http://opus.kobv.de/ubp/volltexte/2006/698/>), 2006.
- Stachlewska, I.S., Neuber, R., Lampert, A., Ritter, C., and Wehrle, G.: AMALi - the Airborne Mobile Aerosol Lidar for Arctic research, submitted to *Atmos. Chem. Phys. Discuss.*, 2009.
- Stachlewska, I.S., Ritter, C., and Neuber, R.: The two-stream method applied to airborne and ground based lidar data, submitted to *Atmos. Chem. Phys. Discuss.*, 2009.
- Stamnes, K., Tsay, S., Wiscombe, W., and Jayaweera, K.: A numerically stable algorithm for discrete-ordinate-method radiative transfer in multiple scattering and emitting layered media, *Appl. Opt.*, 27, 2502–2509, 1988.
- Stephens, G.L., D.G. Vane, R.J. Boain, G.G. Mace, K. Sassen, Z.E. Wand, A.J. Illingworth, E.J. O'Connor, W.B. Rossow, S.L. Durden, S. Miller, R.T. Austin, A. Benedetti, and C. Mitrescu: The CloudSat mission and the A-train. A new dimension of space-based observations of clouds and precipitation, *B. Am. Meteor. Soc.*, 83, 1771-1790, 2002.
- Stohl, A., C. Forster, A. Frank, P. Seibert, and G. Wotawa: Technical Note: The Lagrangian particle dispersion model FLEXPART version 6.2. *Atmos. Chem. Phys.* 5, 2461-2474, 2005.
- Stohl, A.: Characteristics of atmospheric transport into the Arctic troposphere, *J. Geophys. Res.*, 111, D11306, doi:10.1029/2005JD006888, 2006.
- Stohl, A., Berg, T., Burkhardt, J.F., Fjærraa, A.M., Forster, C., Herber, A., Hov, Ø., Lunder, C., McMillan, W.W., Oltmans, S., Shiobara, M., Simpson, D., Solberg, S., Stebel, K., Ström, J., Tørseth, K., Treffeisen, R., Virkkunen, K., and Yttri, K.E.: Arctic smoke – record high air pollution levels in the European Arctic due to agricultural fires in Eastern Europe. *Atmos. Chem. Phys.* 7, 511-534, 2007.
- Ström, J., Umegård, J., Tørseth, K., Tunved, P., Hansson, H.-C., Holmén, K., Wismann, V., Herber, A., and König-Langlo, G.: One year of particle size distribution and aerosol chemical composition measurements at the Zeppelin Station, Svalbard, March 2000-March 2001, *Physics and Chemistry of the Earth*, 28, 1181-1190, 2003.
- Thomas, A., Borrmann, S., Kiemle, C., Cairo, F., Volk, M., Beuermann, J., Lepuchov, B., Santacesaria, V., Matthey, R., Rudakov, V., Yushkov, V., MacKenzie, A.R., and Stefanutti, L.: In situ measurements of background aerosol and subvisible cirrus in the tropical tropopause region, *J. Geophys. Res.*, 107(D24), 4763, doi:10.1029/2001JD001385, 2002.
- Treffeisen, R., Rinke, A., Fortmann, M., Dethloff, K., Herber, A., and Yamanouchi, T.: An estimation on the radiative effects of Arctic aerosols using two different aerosol data sets: A case study for March 2000, *Atmos. Environ.*, 39, 887-899, 2005.
- Treffeisen, R., P. Turnved, J. Ström, A. Herber, J. Bareiss, A. Helbig, R. S. Stone, W. Hoyningen-Hüne, R. Krejci, A. Stohl, and R. Neuber: Arctic smoke – aerosol characteristics during a record smoke event in the European Arctic and its radiative impact, *Atmos. Chem. Phys.*, 7, 3035-3053, 2007.
- Tsay, S., and Jayaweera, K.: Physical Characteristics of Arctic Stratus Clouds, *J. Climate and Appl. Met.*, 23, 584-596, 1984.
- Tsias, A., Wirth, M., Carslaw, K.S., Biele, J., Mehrtens, H., Reichardt, J., Wedekind, C., Weiß, V., Renger, W., Neuber, R., von Zahn, U., Stein, B., Santacesaria, V., Stefanutti, L., Fierli, F., Bacmeister, J., and Peter, T.: Aircraft lidar observations of an enhanced type Ia polar stratospheric clouds during APE-POLECAT, *J. Geophys. Res.*, 104, D19, 23,961-23,969, 1999.

- Turner, D.D.: Arctic Mixed-Phase Cloud Properties from AERI Lidar Observations: Algorithm and Results from SHEBA, *J. Appl. Meteorology*, 44, 427-444, 2005.
- Twomey, S.: The Influence of Pollution on the Shortwave Albedo of Clouds, *J. Atmos. Scie.*, 34, 7, 1149-1152, 1977.
- Uthe, E.E., Nielsen, N.B., and Osberg, T.E.: Airborne scanning lidar observations of aircraft contrails and cirrus clouds during SUCCESS, *Geophys. Res. Lett.*, 25, 9, 1339-1342, 1998.
- Vaughan, M., Young, S., Winker, D., Powell, K., Omar, A., Liu, Z., Hu, Y., and Hostetler, C.: Fully automated analysis of space-based lidar data: An overview of the CALIPSO retrieval algorithms and data products, *Proc. SPIE Int. Soc. Opt. Eng.*, 5575, 16–30, 2004.
- Vavrus, S.: The Impact of Cloud Feedbacks on Arctic Climate under Greenhouse Forcing, *J. Climate*, 17, 603-615, 2004.
- Verlinde, J., Harrington, J.Y., McFarquhar, G.M., Yannuzzi, V.T., Avramov, A., Greenberg, S., Johnson, N., Zhang, G., Poellot, M.R., Mather, J.H., Turner, D.D., Eloranta, E.W., Zak, B.D., Prenni, A.J., Daniel, J.S., Kok, G.L., Tobin, D.C., Holz, R., Sassen, K., Spangenberg, D., Minnis, P., Tooman, T.P., Ivey, M.D., Richardson, S.J., Bahrman, C.P., Shupe, M., DeMott, P.J., Heymsfield, A.J., and Schofield, R.: The Mixed-Phase Arctic Cloud Experiment, *BAMS*, doi:10.1175/BAMS-88-2-205, pp. 205-221, 2007.
- Visconti, G.: *Fundamentals of Physics and Chemistry of the Atmosphere*, Springer Verlag, Berlin, Heidelberg, ISBN 3-540-67420-9, 593 pp., 2001.
- Wandinger, U.: Multiple-scattering influence on extinction- and backscatter-coefficient measurements with Raman and high-spectral-resolution lidars, *Appl. Opt.*, 37, 3, 417-427, 1998.
- Warren, S. G., and Brandt, R. E.: Optical constants of ice from the ultraviolet to the microwave: A revised compilation. *J. Geophys. Res.*, 113, D14220, 2008.
- Wegener, A.: *Thermodynamik der Atmosphäre*, J. A. Barth Verlag, 311 pp., 1911.
- Welton, E.J., Campbell, J.R., Spinhirne, J.D., and Scott, V.S.: Global monitoring of clouds and aerosols using a network of micro-pulse lidar systems, *Proc. Int. Soc. Opt. Eng.*, 4153, 151-158, 2001.
- Wendisch, M., Müller, D., Schell, D., and Heintzenberg, J.: An airborne spectral albedometer with active horizontal stabilization, *J. Atmos. Oceanic Technol.*, 18, 1856–1866, 2001.
- Wernli, H. and Davies, H. C.: A Lagrangian-based analysis of extratropical cyclones, I: The method and some applications, *Q. J. Roy. Meteorol. Soc.*, 123, 467–489, 1997.
- Wieliczka, D. M., Weng, S. S., and Querry, M. R.: Wedge shaped cell for highly absorbent liquids - Infrared optical-constants of water, *Appl. Opt.*, 28, 1714-1719, 1989.
- Winker, D. M., Hunt, B.H., and McGill, M.J.: Initial performance assessment of CALIOP, *Geophys. Res. Lett.*, 34, L19803, doi:10.1029/2007GL030135, 2007.
- Winker, D., and Trepte, C.: Distribution and Characteristics of Polar Clouds from CALIOP, A-Train-Lille 07 symposium, 22-25 October 2007.
- Wyser, K., Jones, C.G., Du, P., Girard, E., Willén, U., Cassano, J., Christensen, J.H., Curry, J.A., Dethloff, K., Haugen, J.-E., Jacob, D., Körtzow, M., Laprise, R., Lynch, A., Pfeifer, S., Rinke, A., Serreze, M., Shaw, M.J., Tjernström, M., and Zagar, M.: An evaluation of Arctic cloud and radiation processes during the SHEBA year: simulation results from eight Arctic regional climate models, *Clim. Dyn.*, 30, doi:10.1007/s00382-007-0286-1, 203-223, 2008.

Yamanouchi, T., Treffeisen, R., Herber, A., Shiobara, M., Yamagata, S, Hara, K., Sato, K., Yabuki, M., Tomikawa, Y., Rinke, A., Neuber, R., Schumacher, R., Kriews, M., Ström, J, Schrems, O., and Gernandt, H.: Arctic Study of Tropospheric Aerosol and Radiation (ASTAR) 2000: Arctic haze case study, *Tellus*, 57B, 141-152, 2005.

Yang, P., and Liou, K.N., Geometric-optics-integral-equation method for light scattering by nonspherical ice crystals, *Appl. Opt.*, 35, 6568-6584, 1996.

You, Y., Kattawar, G.W., Yang, P., Hu, Y.X., and Baum, B.A.: Sensitivity of depolarized lidar signals to cloud and aerosol particle properties, *J. Quantitative Spectroscopy & Radiative Transfer*, 100, 470-482, 2006.

Zhang, T., Stamnes, K., and Bowling, S.A.: Impact of Clouds on Surface Radiative Fluxes and Snowmelt in the Arctic and Subarctic, *J. Climate*, 9, 2110-2123, 1996.

Zuidema, P., Baker, B., Han, Y., Intrieri, J., Key, J., Lawson, P., Matrosov, S., Shupe, M., Stone, R., and Uttal, T.: An Arctic Springtime Mixed-Phase Cloudy Boundary Layer Observed during SHEBA, *J. Atmos. Sci.*, 62, 160-176, 2005.

Acknowledgements

Many persons supported me during the PhD thesis.

First of all, I would like to thank Klaus Dethloff for the great opportunity of working in his research group and for the flexibility concerning the topic of my thesis. A cordial thanks to my supervisor Roland Neuber, who always had an open door and was within reach by telephone under any circumstances. A thanks to Christoph Ritter for sharing his vast lidar experience with me. To Franz Immler for the practical assistance in questions of lidar handling and during the process of modifying the lidar setup. Joann Schmid is acknowledged for the mechanical construction work, Bernhard Stein and Bernd Mielke for the software adaptation of the modified AMALi version. A deep thanks to Anne Hoffmann for the spontaneous decision to help out during the ASTAR campaign.

Thank you to Jean - François Gayet, Manfred Wendisch and Christine Böckmann for the willingness to review the thesis.

Heiko Gericke and Tobias Schmidt are gratefully acknowledged for their support with any issues concerning the connection to Potsdam.

I further would like to acknowledge Iwona Stachlewska for all the work performed with the AMALi system, providing the evaluation programs and giving me a good start in Potsdam.

A deep thanks to the ASTAR 2007 members, especially Andreas Herber, Andreas Minikin and Manfred Wendisch for the organization, Andreas Hahn, Jens Heider and Jens Hammer for the successful and unforgettable flights, Thomas Garbrecht and Jürgen Höltig for their help with technical problems, and all the other persons involved.

Thanks to Andreas Dörnbrack for the interest in the measurements and the support with meteorological analyses and great plots.

Thanks to the LaMP group, especially Jean - François Gayet, Guillaume Mioche and Olivier Jourdan for the fruitful collaboration and motivation during the data analysis, as well as to André Ehrlich (Uni Mainz / Leipzig) for sharing ideas and realizing the radiative transfer calculations of "Astrid's cloud".

A thanks to the whole group at AWI Potsdam for the numerous inspiring discussions, the great atmosphere, and the cake. :-)

Thanks to all the people who contributed to the success of the first publications.

I also would like to thank Rolf Weller for waking my interest in performing the PhD thesis at the lidar group of AWI Potsdam.

I would like to give a cordial thanks to everybody who helped to improve the thesis by valuable contributions and corrections of the manuscript: To Annette Rinke for checking the HIRHAM description, to Andreas Minikin and Andreas Stohl for adding their expertise to the ASTAR chapter, to Klaus Dethloff, Manfred Wendisch, Jean - François Gayet, Roland Neuber, Anne Hoffmann, Christoph Ritter, Marion Maturilli, André Ehrlich, Andreas Dörnbrack, Rolf Weller, and Rudolf Richter for going through the manuscript.

This work would not have been possible without the constant support of my family. Thank you so much, Philipp, for providing me the necessary time, for helping with formatting issues, for borrowing me "Alouette" spontaneously, and for your motivation to finish the project. Thank you, Dominik, for the welcome distractions and for accepting that Mom also needs to work.

Die "**Berichte zur Polar- und Meeresforschung**" (ISSN 1866-3192) werden beginnend mit dem Heft Nr. 569 (2008) ausschließlich elektronisch als Open-Access-Publikation herausgegeben. Ein Verzeichnis aller Hefte einschließlich der Druckausgaben (Heft 377-568) sowie der früheren "**Berichte zur Polarforschung**" (Heft 1-376, von 1982 bis 2000) befindet sich im Internet in der Ablage des electronic Information Center des AWI (**ePIC**) unter der URL <http://epic.awi.de>. Durch Auswahl "Reports on Polar- and Marine Research" auf der rechten Seite des Fensters wird eine Liste der Publikationen in alphabetischer Reihenfolge (nach Autoren) innerhalb der absteigenden chronologischen Reihenfolge der Jahrgänge erzeugt.

To generate a list of all Reports past issues, use the following URL: <http://epic.awi.de> and select the right frame to browse "Reports on Polar and Marine Research". A chronological list in declining order, author names alphabetical, will be produced, and pdf-icons shown for open access download.

Verzeichnis der zuletzt erschienenen Hefte:

Heft-Nr. 595/2009 — "The Expedition of the Research Vessel 'Polarstern' to the Antarctic in 2008/2009 (ANT-XXV/2)", edited by Olaf Boebel

Heft-Nr. 596/2009 — "Crustal evolution of the submarine plateaux of New Zealand and their tectonic reconstruction based on crustal balancing", by Jan Werner Gerhard Grobys

Heft-Nr. 597/2009 — "The Expedition of the Research Vessel 'Polarstern' to the Arctic in 2008 (ARK-XXIII/3)", edited by Wilfried Jokat

Heft-Nr. 598/2009 — "The Expedition of the Research Vessel 'Pelagia' to the Natal Basin and the Mozambique Ridge in 2009 (Project AISTEK III)", edited by Wilfried Jokat

Heft-Nr. 599/2009 — "The Expedition of the Research Vessel 'Maria S. Merian' to the Labrador Sea in 2009 (MSM12/2)", edited by Gabriele Uenzelmann-Neben

Heft-Nr. 600/2009 — "Russian-German Cooperation SYSTEM LAPTEV SEA: The Expedition Lena 2009, edited by Julia Boike, Katya Abramova, Dmitry Yu. Bolshiyarov, Mikhail N. Grigoriev, Ulrike Herzschuh, Gerhard Kattner, Christian Knoblauch, Lars Kutzbach, Gesine Mollenhauer, Waldemar Schneider

Heft-Nr. 601/2009 — "Analyse von Bathymetrie und akustischer Rückstreuung verschiedener Fächersonar- und Sedimentecholot-Systeme zur Charakterisierung und Klassifizierung des Meeresbodens am Gakkel-Rücken, Arktischer Ozean", by Jörn Hatzky

Heft-Nr. 602/2009 — "Cumacea (Crustacea; Peracarida) of the Antarctic shelf – diversity, biogeography, and phylogeny", by Peter Rehm

Heft-Nr. 603/2010 — "The Expedition of the Research Vessel 'Polarstern' to the Antarctic in 2009 (ANT-XXV/5)", edited by Walter Zenk and Saad El Naggat

Heft-Nr. 604/2010 — "The Expedition of the Research Vessel 'Polarstern' to the Antarctic in 2007/2008 (ANT-XXIV/2)", edited by Ulrich Bathmann

Heft-Nr. 605/2010 — "The Expedition of the Research Vessel 'Polarstern' to the Antarctic in 2003 (ANT-XXI/1)", edited by Otto Schrems

Heft-Nr. 606/2010 — "The Expedition of the Research Vessel 'Polarstern' to the Antarctic in 2008 (ANT-XXIV/3)", edited by Eberhard Fahrbach and Hein de Baar

Heft-Nr. 607/2010 — "The Expedition of the Research Vessel 'Polarstern' to the Arctic in 2009 (ARK-XXIV/2)", edited by Michael Klages

Heft-Nr. 608/2010 — "Airborne lidar observations of tropospheric Arctic clouds", by Astrid Lampert